COULOMB ATTRACTION EFFECTS IN SEMICONDUCTOR QUANTUM WELL LASERS

By

CHIA-FU HSU

DISSERTATION PRESENTED TO THE GRADUATE SCHOOL
OF THE UNIVERSITY OF FLORIDA IN PARTIAL FULFILLMENT
OF THE REQUIREMENTS FOR THE DEGREE OF
DOCTOR OF PHILOSOPHY

UNIVERSITY OF FLORIDA

1997

Copyright 1997

By

CHIA-FU HSU

DEDICATED TO MY PARENTS,
CHUNG-MEI TSAI AND HUNG-YI HSU

AND IN MEMORY OF MY DEAREST BROTHER,
CHIA-HENG HSU

ACKNOWLEDGMENTS

Being able to have the strength to finish my dissertation, I am very grateful to my parents, Chung-Mei Tsai and Hung-Yi Hsu, my sister, Sung-Ya Hsu, and my grandmother for their unconditional love and support. I feel particularly indebted to my parents for not being able to spend time with them during these years of studying abroad. I hope at least my academic accomplishment can make them proud.

I would like to express my sincere thanks to my advisor, Dr. Peter S. Zory. He has always been very inspiring to me during my studies these years in the Department of Electrical and Computer Engineering at University of Florida. He has the ability to explain complicated subjects in a way that people can understand and that attracts me to the research field of semiconductor diode lasers. I also thank him for offering me the financial support as a research assistant and I have truly enjoyed working for him.

I would like to thank all the professors on my Ph.D. committee: Dr. Gijs Bosman, Dr. Fredrik A. Lindholm, Dr. Ramakant Srivastava, and Dr. Kevin S. Jones. I have appreciated the guidance they have provided for this dissertation and their contributions to my understanding of semiconductor physics and my experimental skills.

I particularly wish to thank Dr. Paul Rees at University of Wales, Bangor, UK, for the very valuable discussions on Coulomb attraction effects in semiconductor lasers. I would also like to thank Dr. M. A. Haase at the 3M Company and Dr. M. A. Emanuel at the Lawrence Livermore National Laboratory for providing me with state-of-the-art CdZnSe and InGaAs QW laser materials, respectively.

I would like to gratefully recognize all the students with whom I have worked during the last four years of pursuing my Ph.D. Particular thanks go to Dr. Chi-Lin "Kenny"

Young, Dr. Chih-Hung "David" Wu, Dr. Craig Largent, Bob Widenhofer, Jeong-Seok "Jason" O, Carl Miester, John Yoon, Christian Keyser and Jee-Hoon "Steve" Han for their professional opinions and friendships.

I also would like to gratefully acknowledge my friends at the Emmanuel Mennonite Church in Gainesville, especially Mary and Paul Lehman for being my host family. It was their kindness and caring that made me, as an international student and for the first time being 13,000 miles away from home five and half years ago, feel comfortable in this country very quickly.

I would like to gratefully recognize a late friend, Hsi-Hung Kuo, for his generosity in helping me and numerous new students from Taiwan during his two years of Ph.D. study in Department of Electrical and Computer Engineering at University of Florida. I am also grateful to my friend, Dr. Yu-Fu Hsieh, and his wife, Hsueh-Chu Chen, for helping me settle down in Gainesville and treating me like their brother since then. I would like to thank my dear friends, Margaret and Kathy Cheng, and their parents for inviting me to their house during many holidays. I am also grateful to my best friend, Ming-Cheng "Benjamin" Liu, his wife, Chun-Yi "Jean" Chen, for that they always reserved an extra pair of chop sticks on their dining table for me.

Last, but certainly not least, I want to thank my girlfriend, Huei-Feng "Vicky" Lee, for the companionship, love and encouragement that she gave me.

TABLE OF CONTENTS

page

ACKNOWLEDGMENTS iv

ABSTRACT........ ix

CHAPTERS

1 INTRODUCTION 1

2 SINGLE-PARTICLE MODEL 6

2.1 Introduction 6
2.2 Laser Structures 7
2.2.1 InGaAs QW Laser 7
2.2.2 CdZnSe QW Laser 7
2.3 Strained Quantum Wells 8
2.3.1 Strained Bandgaps 8
2.3.2 Bandgap Lineup 15
2.3.3 Numerical Results 16
2.4 Active Region Model 21
2.4.1 Potential Wells and Quantized States 21
2.4.2 Parabolic In-plane Subband Structures 24
2.4.3 Numerical Results 25
2.5 Single-Particle Gain and Spontaneous Emission Functions 26
2.5.1 Transition Energy 26
2.5.2 Gain and Spontaneous Emission 27
2.6 Simulation Results 30
2.6.1 InGaAs QW 30
2.6.2 CdZnSe QW 31
2.6.3 Comparison 31
2.7 Summary 36

3 MANY-BODY EFFECTS 39

3.1 Introduction 39
3.2 Carrier Scattering (CS) 39

3.2.1 Gain and Spontaneous Emission Functions 39
3.2.2 Simulation Results 42
3.3 Bandgap Renormalization (BGR) 45
3.3.1 Plasma Screening 45
3.3.2 Bandgap Renormalization 49
3.3.3 Simulation Results 52
3.4 Coulomb Enhancement (CE) 53
3.4.1 Coulomb Enhancement Factor 53
3.4.2 Gain and Spontaneous Emission Functions 60
3.4.3 Simulation Results 63
3.5 Summary 66

4 LASER THRESHOLD CHARACTERISTICS 67

4.1 Introduction 67
4.2 Laser Devices 68
4.2.1 InGaAs QW 68
4.2.2 CdZnSe QW 68
4.3 Cavity Length Dependence of Lasing Energy 68
4.3.1 Experiment 71
4.3.2 Prediction 72
4.4 Cavity Length Dependence of Threshold Current 89
4.4.1 Experiment 89
4.4.2 Prediction 90
4.4.2.1 Gain-current relation 96
4.4.2.2 Predicting threshold current 97
4.5 Temperature Dependence of Lasing Energy 106
4.5.1 Experiment 106
4.5.2 Prediction 107
4.6 Summary 110

5 ABSORPTION RESONANCES DUE TO COULOMB ATTRACTION 114

5.1 Introduction 114
5.2 Claims of Evidence for Excitonic Gain 114
5.3 Calculation of Gain/Absorption Spectra 115
5.4 Comparison between Calculations and Experiments 121
5.4.1 Spectral Correlation between Peaks of Absorption and Spontaneous Emission 121
5.4.2 Energy Arrangement of Some Key Spectral Features 121
5.4.3 Coexistence of Gain with Absorption 125
5.4.4 Evolution of Gain/Absorption Spectra with Injection Level 126
5.5 Summary 126

6 CARRIER-INDUCED EFFECTS IN II-VI QW LASERS 130

6.1 Introduction 130
6.2 Effect of Injected Carriers on the Refractive Index 131
6.2.1 Complex Optical Dielectric Function 131
6.2.2 Complex Refractive Index 132
6.2.3 Simulation results 133
6.3 Beam Quality 134
6.3.1 Antiguiding Factor 134
6.3.2 A Qualitative Description 141
6.4 Near-Field Measurement 146
6.5 Summary 149

7 CONCLUSIONS AND FUTURE WORKS 152

7.1 Conclusions 152
7.2 Future Works 154

APPENDICES

A MATERIAL PARAMETERS II-VI TERNARIES 157

A.1 Interpolation Method 157
A.2 Binary Parameters 158
A.3 Ternary Parameters 158

B TRANSITION MATRIX ELEMENT 162

B.1 Polarization-Dependent Effects 162
B.2 Angle-Dependent Effects 165

REFERENCES 168

BIOGRAPHICAL SKETCH 174

Abstract of Dissertation Presented to the Graduate School
of the University of Florida in Partial Fulfillment of the
Requirements for Degree of Doctor of Philosophy

COULOMB ATTRACTION EFFECTS IN SEMICONDUCTOR QUANTUM WELL LASERS

By

CHIA-FU HSU

December, 1997

Chairman: Peter S. Zory
Major Department: Electrical and Computer Engineering

Theoretical and experimental studies of many-body effects in semiconductor quantum well (QW) lasers are presented. These many-body effects arise from the Coulomb force interactions among the charged particles trapped in the quantum well and their interaction with phonons. Expressions are derived for the dependence of optical gain and spontaneous emission on photon energy using an electron-hole plasma (EHP) theory with many-body effects taken into account. Optical gain and spontaneous emission spectra are calculated for the well-developed, infrared emitting, InGaAs/GaAs strained QW structure and the relatively-new blue-green CdZnSe/ZnSSe strained QW structure. The results show that Coulomb attraction effects (CE) have a significantly stronger effect on the spectral characteristics of the wide-bandgap CdZnSe QW structure than on the narrow-bandgap InGaAs QW structure. The room-temperature dependences of lasing energy and threshold current on cavity length for InGaAs and CdZnSe QW diode lasers are numerically simulated and compared to experiment. In all cases, the comparisons are found to be in better agreement when CE is included in the calculations. The importance of CE is also found when comparing the experimental and calculated lasing energies for a CdZnSe QW laser over the temperature range from 160 K to 300 K. For photon energies somewhat higher than the lasing energy, the calculated optical gain spectra with CE included show resonance-like absorption features usually attributed to excitons in the QW. A comparison of these absorption spectra with published experimental spectra shows good agreement. Since excitons do not exist in the CE model used, this success refutes published work which says that free excitons play an important role in determining the magnitude of optical gain in room temperature CdZnSe QW lasers.

CHAPTER 1
INTRODUCTION

Semiconductor diode lasers have become the key components in many commercial products such as compact disk players, laser printers and optical fiber telecommunication systems. High-power diode lasers are also used in applications such as medical surgery, free-space communication and diode laser pumped solid-state lasers. Diode laser design with a double heterojunction (DH) active layer of thickness about 100 to 200 nm was perfected in the late 1970s and early 1980s. When reducing the thickness of the active layer down to the 10 nm regime, electrons and holes are confined in the active layer and the associated states become quantized in the potential wells along the direction normal to the active layer. Quantum well (QW) diode lasers, devices with this very thin active layer design, were realized in the 1980s and shown to have higher performance than their DH counterparts. By introducing built-in strain in the QW, these strained QW lasers were found to be substantially superior to unstrained QW lasers. Although these improvements in diode lasers rely heavily on advances in high-quality crystal-growth techniques such as molecular beam epitaxy (MBE), the ideas behind them came from thoroughly understanding the basic mechanism of optical gain and spontaneous emission in diode lasers. Stimulated electron-hole recombination in the active layer was believed to be responsible for the laser action in diode lasers and an electron-hole plasma (EHP) theory was used to model the laser devices such as the well-developed infrared (IR) GaAs-based QW lasers [Asa93, Col95, Cor93]. Soon after the demonstration of the world's first blue-green diode lasers fabricated using a CdZnSe QW structure by 3M Company personnel in June 1991 [Haa91], confusion about the gain mechanism in these new CdZnSe QW lasers began. J. Ding *et al.* reported the first observation of so-called excitonic gain and laser emission in ZnSe-based QWs and proposed a phenomenological model of optical gain based on partial phase-space filling (PSF) of an inhomogeneously broadened exciton resonance [Din92]. This phenomenological gain model, which includes the effects of exciton-phonon interaction, was used to explain their pump-probe experiment at cryogenic temperature up to 220 K [Din93]. In 1994, J. Ding *et al.* reported the measured gain/absorption spectra of CdZnSe QW diode lasers at T = 300 K in which two resonance-like absorption peaks appearing at low excitation level were attributed to absorption resonances from $n = 1$ HH and LH excitons [Din94]. The conclusion drawn was that the origin of optical gain in blue-green CdZnSe QW lasers is excitonic in nature even at room temperature. Since the conventional EHP theory did not include exciton effects, these claims attracted considerable attention in the diode laser community.

Setting aside the truth about the lasing mechanism in CdZnSe QW lasers for a moment, physicists, working for many years in the research field of fundamental semiconductor physics, have been studying the mutual interactions among charged particles (i.e. electrons and holes) in semiconductors. These interactions in an EHP system include carrier scattering (CS), bandgap renormalization (BGR) and Coulomb enhancement (CE) and are usually referred to as many-body effects in the literatures. Haug *et al.* showed that gain spectra of a semiconductor changed when many-body effects were taken into account [Hau90]. Although CS and BGR were usually included in the conventional EHP theory [Asa93, Col95, Cor93], there seemed to be a tendency to ignore CE in the diode laser community since CE calculations are more complicated than those for CS and BGR. A theory with such an ignorance of CE was shown to lead to predictions that were in worse agreement with experiment than predictions of a theory with only CS included [Che93, Chi88]. The errors result from the fact that it is inconsistent to account for the Coulomb repulsion, which gives rise to BGR, and at the same time ignore the Coulomb attraction, which gives rise to CE. Since Coulomb interactions are stronger in materials with smaller dielectric constants, CE is expected to be more important in the wide-bandgap CdZnSe QW lasers [Cho95b, Ree95a] than in the narrow-bandgap GaAs-based QW lasers [Cho94, Hau90].

Now going back to the discussion about the nature of the gain mechanism in CdZnSe QW lasers, two questions were thus raised: "Can the operation of CdZnSe QW lasers be simulated using EHP theory with inclusion of CE?" and "Is optical gain in CdZnSe QW lasers of excitonic nature?" The approach to answering these questions is twofold: theoretical and experimental. In the theoretical part, theories of many-body effects available in the literatures were studied extensively and understood thoroughly. These existing theoretical works were all done under the assumption of a perfect two-dimensional (2D) QW with zero QW thickness and infinite barrier height. In addition, the formula derived for many-body effects are limited to the case that only the lowest conduction (CB) and valence band (VB) subbands exist. The simple perfect 2D QW model has no physical meaning except for easy demonstration of many-body effects in semiconductors.

In order to use these many-body formulas and implement them in the device simulation for actual QW diode lasers, several modifications to the formulas had to be made. First, the finite QW thickness and barrier height in real QW lasers were taken into account. In such a quasi-2D QW, a number of subbands in both CB and VB become available from solving the one-dimensional (1D) Schrödinger's equation. Second, effective mass anisotropy in the VB due to the large built-in strain the QW was considered, where the heavy hole (HH) and light hole (LH) effective masses in the in-plane direction become different from those in the growth direction. Third, a model with CE included for the spontaneous emission function was developed in order to estimate the threshold current required for lasing, since most of the existing literatures on many-body effects really dealt only with the gain function [Cho94, Hau90]. Four, the modified many-body formulas were integrated with the state-of-the-art EHP theory where CE has not been taken into account [Asa93, Col95, Cor93]. Efforts were also placed on converting formulas from wavevector space to energy space, from summations to integrals and from the C.G.S. units used by many-body physicists to the M.K.S. units which are more familiar to diode laser engineers. As a result of these works, the complicated formulas derived by many-body physicists have been translated to a form more user-friendly so that electrical engineers can implement them into computer codes for device simulation of QW diode lasers.

In the experimental part of this work, a number of well-developed IR InGaAs strained QW lasers and relatively new blue-green CdZnSe strained QW lasers were fabricated. Since the laser threshold current and peak wavelength change with laser cavity length, different models for the physical mechanism of optical gain and spontaneous emission were tested by investigating these length dependences. Since the emphasis in this work has been placed on the CdZnSe QW laser, further measurements on the temperature dependence of lasing wavelength were performed on the CdZnSe QW lasers.

This dissertation is organized such that the theoretical models are described and developed first, experiments and experimental results are then presented, predictions by using the theoretical models and their comparisons with experiments are made and finally the conclusions are drawn. Several comparisons and comments on the differences between the InGaAs and CdZnSe QW lasers are made throughout each chapter.

In Chapter 2, the gain and spontaneous emission functions based on a single-particle model are discussed in detail. It begins by introducing the epitaxial structures for the two QW lasers of interest: III-V InGaAs and II-VI CdZnSe QW lasers. Effect of strain on the bandgap of the QW material are discussed and the active region model used in the theoretical simulation for the QW laser structures described. Finally, the optical gain and spontaneous emission spectra in the single-particle model are calculated.

In Chapter 3, many-body effects, such as CS, BGR and CE, on the gain and spontaneous emission functions are discussed sequentially. Semi-derivations of BGR and CE are presented. Calculation results of the optical gain and spontaneous emission spectra with many-body effects included are shown and comments on how CS, BGR and CE modify the single-particle spectra are made.

In Chapter 4, experimental measurements of laser threshold characteristics for InGaAs/GaAs QW and CdZnSe/ZnSSe QW lasers are presented and compared to predictions. The first question mentioned above "Can the operations of CdZnSe QW lasers be simulated by using the EHP theory with inclusion of CE?" is answered.

In Chapter 5, the other question "Is optical gain in CdZnSe QW lasers of excitonic nature?" is answered by comparing several spectral features of the calculated gain/absorption and spontaneous emission spectra with the inclusion of CE to those of the experimental observations.

In Chapter 6, the carrier-induced antiguiding factor is calculated for the CdZnSe QW lasers and its effect on the quality of laser beam is described. Near-field patterns are measured and compared qualitatively to the predictions.

Finally, in Chapter 7, conclusions are drawn and future works are suggested.

CHAPTER 2
SINGLE-PARTICLE MODEL

2.1 Introduction

The chapter begins by introducing the epitaxial structures for the two QW lasers of interest: III-V InGaAs and II-VI CdZnSe QW lasers. Due to the mismatch of the in-plane lattice constant between a thin QW layer and thick barrier layers, the thin QW layer is subject to lattice deformation and under biaxial strain. Then, effect of strain on the bandgap of the QW material will be discussed. A common approach is used to determine the bandgap lineup at the interface between the QW and barrier layers by assuming a conduction band offset ratio. Strain calculation will be performed on both InGaAs and CdZnSe QW laser structures. Next, we consider an active region model to be used in the theoretical simulation for the QW laser structures. It consists of a QW layer and two barrier layers of infinite thickness on each side. A flat-band approximation is assumed in constructing the potential well diagram for the active region model. A typical quantum well problem is then solved for the quantized energy levels in the CB and VB (including HH and LH bands) potential wells. Numerical results from the calculation for the two material systems will be shown and summarized. Finally, from the active region model developed, we will be able to explore the optical gain and spontaneous emission functions using the single-particle model. A set of calculated gain and spontaneous emission spectra as a function of carrier density in the QW for both InGaAs and CdZnSe QW lasers will be presented. Comparison between two material systems will be made.

Several appendices will serve as the supplements for more in-depth discussions of many relevant subjects in this chapter. In brief, derivation of material parameters for CdZnSe and ZnSSe ternary alloys from the material parameters of the related binary alloys, based on an interpolation scheme, can be found in Appendix A. In Appendix B, the transition matrix element, which determines the strength of interaction between two states, and its polarization-dependent effects are discussed.

2.2 Laser Structures

2.2.1 InGaAs QW Laser

The InGaAs/GaAs graded-index separate-confinement heterostructure (GRIN-SCH) single QW diode laser structure studied in this work, for which the schematic sketch of cross-section epitaxial layers and the corresponding diagram of Al and In composition profile are shown in Fig. 2.1, consists of a 25 nm graded $Al_xGa_{1-x}As$ layer ($x = 0.05 - 0.6$) grown on a n-GaAs substrate, a 1400 nm n-$Al_{0.6}Ga_{0.4}As$ cladding layer, a 200 nm graded $Al_yGa_{1-y}As$ (undoped) guiding layer ($y = 0.6 - 0.3$), an 8 nm undoped $In_zGa_{1-z}As$ ($z \sim 0.15$) compressively-strained quantum well centered between two 7 nm GaAs layers, a 200 nm graded $Al_yGa_{1-y}As$ (undoped) guiding layer ($y = 0.3 - 0.6$), a 1300 nm p-$Al_{0.6}Ga_{0.4}As$ cladding layer, a 25 nm graded $Al_xGa_{1-x}As$ layer ($x = 0.6 - 0.05$) and a 100 nm p^+-GaAs cap layer. The guiding and cladding layers provide for electrical and optical confinement respectively in the growth direction.

2.2.2 CdZnSe QW Laser

A cross-section diagram of the epitaxial layers of the CdZnSe/ZnSSe SCH SQW diode laser studied in this work is shown in Fig. 2.2. It consists of a GaAs buffer layer grown by MBE on an n-type GaAs (001) substrate [Gai93], a ZnSe buffer layer, a quaternary n-

ZnMgSSe cladding layer, a 4 nm $Cd_xZn_{1-x}Se$ (x ~ 0.3) compressively-strained quantum well (QW) centered between n- and p-$ZnS_{0.06}Se_{0.94}$ guiding layers, a p-ZnMgSSe cladding layer and a graded p^+-$ZnSe_xTe_{1-x}$ (x = 1 to 0) contact layer. This contact scheme provides a reasonably low resistance p-contact to the laser structure [Fan92].

2.3 Strained Quantum Wells

2.3.1 Strained Bandgaps

When a very thin layer of QW is grown out of a material with a larger native lattice constant than that of the surrounding barrier layers, the lattice compresses in the plane of the well (in-plane direction denoted as ||) to match that of the barrier layers and elongates in the growth direction (normal to the plane of well and denoted as ⊥) to keep the volume of each unit cell the same, as shown in Fig. 2.3. In this case, QW is said to be under biaxial compressive strain. If the native lattice constant of QW is smaller than that of the barrier layers, QW is then under biaxial tensile strain. Degree of lattice-mismatch can be described with a lattice-mismatch parameter ε defined as follows [Col95]:

$$\varepsilon = 1 - \frac{a_b}{a_w}, \tag{2.1}$$

where a_b is the in-plane lattice constant of the barrier material and a_w is the native unstrained in-plane lattice constant of the strained QW material. From Eq. (2.1), we have $\varepsilon > 0$ for biaxial compressive strain ($a_w > a_b$) and $\varepsilon < 0$ for biaxial tensile strain ($a_w < a_b$). The lattice distortion of the crystal due to the stress resulting from lattice-mismatch is usually defined mathematically by a strain tensor ε_{ij}. Assuming the shear component of stress ($i \neq j$) can be ignored, which is valid in typical semiconductor application, we thus only need to consider the three diagonal components of the strain tensor: ε_{xx}, ε_{yy} and ε_{zz}, where x and y subscripts indicate the in-plane directions (||) and z subscript is the growth direction (⊥).

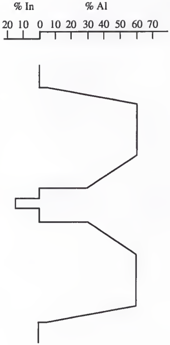

cap	100 nm p^+-GaAs
buffer	25 nm p-AlGaAs
cladding	1300 nm p-AlGaAs
guiding	200 nm AlGaAs
bounding	7 nm GaAs
QW	8 nm InGaAs
bounding	7 nm GaAs
guiding	200 nm AlGaAs
cladding	1400 nm n-AlGaAs
buffer	25 nm n-AlGaAs
substrate	n-GaAs

Figure 2.1 Schematic diagrams of the cross-section epitaxial layers and the corresponding aluminum and indium composition profile for the $In_{0.15}Ga_{0.85}As$/GaAs GRIN-SCH single QW laser.

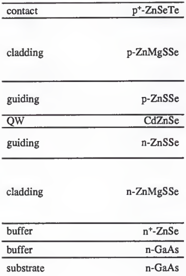

Figure 2.2 Schematic diagram of the cross-section epitaxial layers for the $Cd_{0.3}Zn_{0.7}Se$/ $ZnS_{0.06}Se_{0.94}$ SCH single QW laser.

By symmetry, the strain in both x and y directions must be equal and we obtain

$$\varepsilon_{\parallel} \equiv \varepsilon_{xx} = \varepsilon_{yy} = -\varepsilon. \tag{2.2}$$

Using Eq. (2.1) in Eq. (2.2), we find that ε_{xx}, $\varepsilon_{yy} < 0$ for biaxial compressive strain and ε_{xx}, $\varepsilon_{yy} > 0$ for biaxial tensile strain. With no stress applied to the z direction and the cubic symmetry of the crystal, the strain in the growth direction is related to the strain in the in-plane direction by [Col95]

$$\varepsilon_{\perp} \equiv \varepsilon_{zz} = -2\frac{C_{12}}{C_{11}}\varepsilon_{\parallel}, \tag{2.3}$$

where C_{11} and C_{12} are referred to as the Young's elastic moduli (usually described in the units of 10^{10} N/m^2). Since C_{11} and C_{12} are both positive in common semiconductors (usually $C_{11} > C_{12}$), the lattice deformation along $\perp$ direction will be opposite to the deformation along $\parallel$ directions, as depicted in Fig. 2.3.

Because the bandgap of a semiconductor material is related to its lattice spacing, the distortion in crystal lattice due to the strain should lead to modifications in the bandgap of the strained QW layer. Putting aside the bandgap changes due to the quantum confinement for the present moment, which is left to be discussed in Section 2.4.1, there are two modifications in the strained bandgap. The first modification originates from the hydrostatic component of the strain and under biaxial compressive strain, it produces an upward shift in the conduction band (CB) as well as a downward shift in both heavy hole (HH) and light hole (LH) valence bands (VB), as sketched in Fig. 2.4(a). All the energy shifts are in the opposite directions under biaxial tensile strain. As a result of the hydrostatic strain, the bandgap is changed by an amount $\delta\varepsilon_H$ which is given by [Col95]

$$\delta\varepsilon_H = 2a\varepsilon_{\parallel}\frac{C_{11}-C_{12}}{C_{11}}, \tag{2.4}$$

where a is the hydrostatic deformation potential and $a < 0$ in common semiconductors. We find that the bandgap is increased ($\delta\varepsilon_H > 0$) for biaxial compressive strain and decreased ($\delta\varepsilon_H < 0$) for biaxial tensile strain. The second modification originates from the shear com-

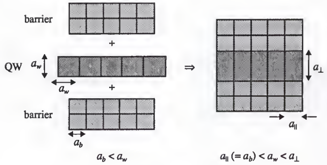

biaxial compressive strain

(a)

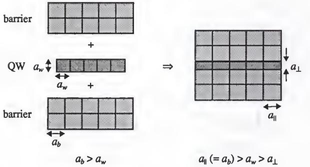

biaxial tensile strain

(b)

Figure 2.3 Illustration of the crystal lattice deformation resulting from the epitaxial growth of a thin layer of QW with a native lattice constant a_w between two thick barrier layers with lattice constant (a) $a_b < a_w$ (biaxial compressive strain); (b) $a_b > a_w$ (biaxial tensile strain).

ponent of the strain (the shear strain should not be confused with the shear stress which is zero in this case [Col95]) and separates the LH band from the HH band, as sketched in Fig. 2.4(a). Under biaxial compressive strain, the shear strain produces an upward shift in HH band by an amount $\delta\varepsilon_{S,\,hh}$ and a downward shift in LH band by an amount $\delta\varepsilon_{S,\,lh}$ which can be expressed as

$$\delta\varepsilon_{S,\,hh} = b\varepsilon_{\parallel}\frac{C_{11}+2C_{12}}{C_{11}}, \tag{2.5}$$

$$\delta\varepsilon_{S,\,lh} = \delta\varepsilon_{S,\,hh}\left(1-\frac{2\delta\varepsilon_{S,\,hh}}{\Delta}\right), \tag{2.6}$$

where b is the shear deformation potential and $b < 0$ in common semiconductors and Δ is the spin-orbit energy which separates the split-off (SO) band from both the HH and LH bands. Under biaxial tensile strain, the shear strain produces an downward shift in HH band ($\delta\varepsilon_{S,\,hh} < 0$) and an upward shift in LH band ($\delta\varepsilon_{S,\,lh} < 0$). As a consequence of the shear strain, the band edge degeneracy of the HH and LH bands is removed and two strained bandgaps are now needed to be defined as follows:

$$\begin{aligned} E_g(\mathrm{HH}) &= E_g(\mathrm{bulk}) + \delta\varepsilon_H - \delta\varepsilon_{S,\,hh} \\ E_g(\mathrm{LH}) &= E_g(\mathrm{bulk}) + \delta\varepsilon_H + \delta\varepsilon_{S,\,lh} \end{aligned}, \tag{2.7}$$

where E_g(bulk) is the unstrained bulk bandgap, E_g(HH) is the C-HH strained bandgap and E_g(LH) is the C-LH strained bandgap. The splitting of the HH and LH bands is usually quantified by the splitting energy S which can be defined as

$$\begin{aligned} S &\equiv E_g(\mathrm{LH}) - E_g(\mathrm{HH}) \\ &= \delta\varepsilon_{S,\,lh} + \delta\varepsilon_{S,\,hh} \\ &= 2\delta\varepsilon_{S,\,hh}\left(1-\frac{\delta\varepsilon_{S,\,hh}}{\Delta}\right) \end{aligned}, \tag{2.8}$$

where Eqs. (2.7) and (2.6) are utilized in the last two expressions, respectively.

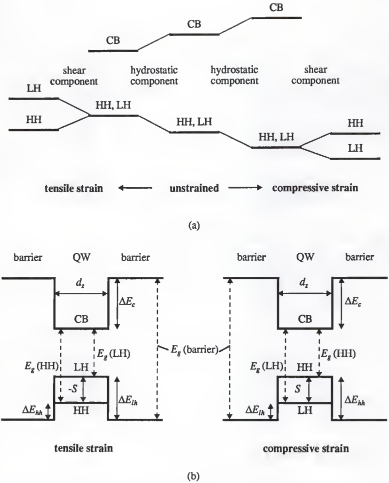

Figure 2.4 Effects of the biaxial tensile and compressive strains on (a) the bulk bandgap of QW material and (b) the bandgap lineup with two barrier layers.

2.3.2 Bandgap Lineup

The bandgap difference between QW and barrier materials causes band discontinuities in both CB and VB at the interfaces of the heterostructure, as sketched in Fig. 2.4(b). The CB offset is defined as ΔE_c and the VB offsets are defined as ΔE_{hh} and ΔE_{lh} for HH and LH bands since they are split by the shear strain. Defining ΔE_g as the bandgap difference between the C-HH strained bandgap of QW and the bandgap of barrier layers, we obtain

$$\Delta E_g = E_g\,(\text{barrier}) - E_g\,(\text{HH})\,, \tag{2.9}$$

where E_g (barrier) is the bandgap of barrier material. As shown in Fig. 2.4(a), CB edge of the strained QW, as well as VB edge, experiences a shift due to the hydrostatic strain. In reality, it is difficult to experimentally separate the CB shift from the total bandgap shift [Cor93]. A common approach is, first, not to worry about how the total shift is divided up between the CB and VB, and then for heterostructures, the lineup of the strained QW bandgap with the barrier bandgaps is typically determined by a CB offset fraction Q_c which can be experimentally measured. In this approach, the CB offset can therefore be expressed as

$$\Delta E_c = Q_c \Delta E_g \tag{2.10}$$

and the VB offset for HH band is given by

$$\Delta E_{hh} = (1 - Q_c)\,\Delta E_g\,. \tag{2.11}$$

Since the LH band is pushed away from the HH band by an amount S as defined in Eq. (2.8), the VB offset for LH band can be shown to be

$$\Delta E_{lh} = \Delta E_{hh} - S\,, \tag{2.12}$$

which means $\Delta E_{lh} < \Delta E_{hh}$ under biaxial compressive strain ($S > 0$) and $\Delta E_{lh} > \Delta E_{hh}$ under biaxial tensile strain ($S < 0$), as depicted in Fig. 2.4(b).

2.3.3 Numerical Results

InGaAs QW. The material parameters as functions of In and Al mole fractions for InGaAs/AlGaAs system have been summarized in Table III of [Cor93]. As shown in Fig. 2.5(a), for the unstrained $In_{0.15}Ga_{0.85}As$, we have E_g (bulk) $\cong$ 1.194 eV and for the strained $In_{0.15}Ga_{0.85}As$ QW/GaAs barrier, we obtain E_g (barrier) $\cong$ 1.424 eV, E_g (HH) $\cong$ 1.267 eV, E_g (LH) $\cong$ 1.329 eV and $S \cong 0.062$ eV. The CB offset in the strained InGaAs/GaAs system is uncertain at present. Various values for Q_c have been reported anywhere in the range from 0.4 to 0.8 [Cor93]. We will assume that $Q_c = 0.55$ for the InGaAs/GaAs system in this work [Wu94, Hsu97a]. As a consequence, with $\Delta E_g = 0.157$ eV, we obtain $\Delta E_c \cong 0.087$ eV, $\Delta E_{hh} \cong 0.071$ eV and $\Delta E_{lh} \cong 0.025$ eV, as sketched in Fig. 2.5(b). Numerical values of the material parameters used in this work for the strained $In_{0.15}Ga_{0.85}As$ QW/GaAs barrier system are summarized in Table 2.1.

CdZnSe QW. For II-VI CdZnSe/ZnSSe system, the ternary material parameters are less well known. In this work, we derive some material parameters used in the calculation for CdZnSe and ZnSSe ternary alloys from the material parameters of the related binary alloys based on an interpolation scheme. Given the present focus on how strain modifies the bandgap of CdZnSe QW, we leave the derivation of the ternary material parameters to Appendix A. Then plugging the II-VI ternary material parameters derived in Appendix A into Eqs. (2.1) through (2.8), we have E_g (bulk) $\cong$ 2.373 eV for the unstrained $Cd_{0.3}Zn_{0.7}Se$ and for the strained $Cd_{0.3}Zn_{0.7}Se$ QW/$ZnS_{0.06}Se_{0.94}$ barrier, we obtain E_g (barrier) $\cong$ 2.729 eV, $\delta\varepsilon_H \cong 0.081$ eV, $\delta\varepsilon_{S,\,hh} \cong 0.057$ eV, $\delta\varepsilon_{S,\,lh} \cong 0.041$ eV, E_g (HH) $\cong$ 2.396 eV, E_g (LH) $\cong$ 2.494 eV and $S \cong 0.098$ eV, as depicted in Fig. 2.6(a). Assuming $Q_c = 0.6$ for the CdZnSe/ZnSSe heterostructure [Hsu97b] and with $\Delta E_g = 0.333$ eV, we obtain $\Delta E_c \cong 0.200$ eV, $\Delta E_{hh} \cong 0.133$ eV and $\Delta E_{lh} \cong 0.035$ eV, as sketched in Fig. 2.6(b). Numerical values of the material parameters used in this work for the strained $Cd_{0.3}Zn_{0.7}Se$ QW/$ZnS_{0.06}Se_{0.94}$ barrier system are summarized in Table 2.2.

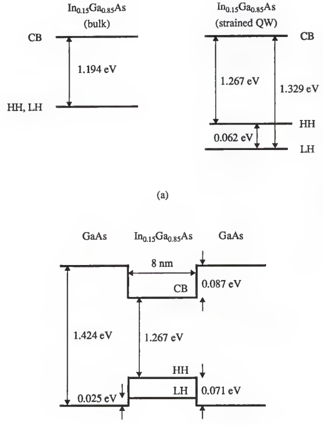

(a)

(b)

Figure 2.5 The strain modified (a) bulk bandgap and (b) potential wells of the 8 nm $In_{0.15}Ga_{0.85}As$/GaAs QW under biaxial compressive strain.

Parameters	$In_{0.15}Ga_{0.85}As$	GaAs
bulk bandgap E_g (eV)	1.194	1.424
Luttinger Parameter γ_1 ($\times \hbar^2/2m_o$)	8.773	6.85
Luttinger Parameter γ_2 ($\times \hbar^2/2m_o$)	3.041	2.1
electron effective mass m_c ($\times m_o$)	0.061	0.067
growth-direction HH effective mass $m_{hh\perp}$ ($\times m_o$)	0.372	0.377
growth-direction LH effective mass $m_{lh\perp}$ ($\times m_o$)	0.067	0.091
background refractive index $\bar{n}$	3.6	
static dielectric constant ε_s	13.33	
$In_{0.15}Ga_{0.85}As$/GaAs strained parameters		
$In_{0.15}Ga_{0.85}As$ HH strained bandgap $E_g(HH) = 1.267$ eV		
$In_{0.15}Ga_{0.85}As$ LH strained bandgap $E_g(HH) = 1.329$ eV		
$In_{0.15}Ga_{0.85}As$ splitting energy $S \equiv E_g(LH) - E_g(HH) = 0.062$ eV		
Bandgap difference $\Delta E_g = 0.157$ eV		
CB offset fraction $Q_c \equiv \Delta E_c/\Delta E_g = 0.55$		
CB offset $\Delta E_c = 0.087$ eV		
HH band offset $\Delta E_{hh} = 0.071$ eV		
LH band offset $\Delta E_{lh} = 0.025$ eV		
$In_{0.15}Ga_{0.85}As$ in-plane HH effective mass $m_{hh\parallel} = 0.085\ m_o$		
$In_{0.15}Ga_{0.85}As$ in-plane LH effective mass $m_{lh\parallel} = 0.174\ m_o$		

Table 2.1 List of material parameters for the $In_{0.15}Ga_{0.85}As$/GaAs strained QW.

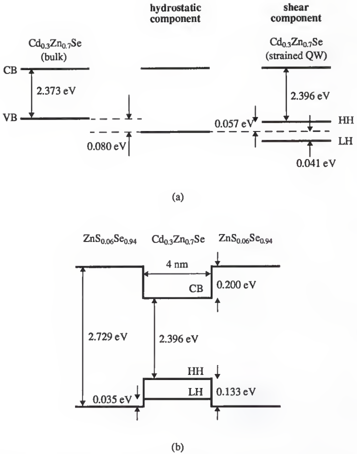

Figure 2.6 The strain modified (a) bulk bandgap and (b) potential wells of the 4 nm $Cd_{0.3}Zn_{0.7}Se/ZnS_{0.06}Se_{0.94}$ QW under biaxial compressive strain.

Parameters	$Cd_{0.3}Zn_{0.7}Se$	$ZnS_{0.06}Se_{0.94}$
bulk bandgap E_g (eV)	2.373	2.729
Luttinger Parameter γ_1 ($\times \hbar^2/2m_o$)	4.495	4.3
Luttinger Parameter γ_2 ($\times \hbar^2/2m_o$)	1.206	1.14
electron effective mass m_c ($\times m_o$)	0.139	0.152
growth-direction HH effective mass $m_{hh\perp}$ ($\times m_o$)	0.480	0.571
growth-direction LH effective mass $m_{lh\perp}$ ($\times m_o$)	0.145	0.157
background refractive index $\bar{n}$	2.947	2.726
static dielectric constant ε_s	9.524	9.23
$Cd_{0.3}Zn_{0.7}Se/ZnS_{0.06}Se_{0.94}$ strained parameters		
$Cd_{0.3}Zn_{0.7}Se$ HH strained bandgap $E_g(HH) = 2.396$ eV		
$Cd_{0.3}Zn_{0.7}Se$ LH strained bandgap $E_g(HH) = 2.494$ eV		
$Cd_{0.3}Zn_{0.7}Se$ splitting energy $S \equiv E_g(LH) - E_g(HH) = 0.098$ eV		
Bandgap difference $\Delta E_g = 0.333$ eV		
CB offset fraction $Q_c \equiv \Delta E_c/\Delta E_g = 0.6$		
CB offset $\Delta E_c = 0.200$ eV		
HH band offset $\Delta E_{hh} = 0.133$ eV		
LH band offset $\Delta E_{lh} = 0.035$ eV		
$Cd_{0.3}Zn_{0.7}Se$ in-plane HH effective mass $m_{hh\parallel} = 0.175\ m_o$		
$Cd_{0.3}Zn_{0.7}Se$ in-plane LH effective mass $m_{lh\parallel} = 0.304\ m_o$		

Table 2.2 List of material parameters for the $Cd_{0.3}Zn_{0.7}Se/ZnS_{0.06}Se_{0.94}$ strained QW.

2.4 Active Region Model

So far, we have determined the bandgap lineups at interfaces of the strained heterostructures. The next step, before going ahead to introduce the gain and spontaneous emission functions, is to define an active region model for the laser structures to be simulated. For the QW laser structures studied, as shown earlier in Figs. 2.1 and 2.2 for the InGaAs QW and CdZnSe QW respectively, they both have an active region structure consisting of a strained QW material sandwiched between two barrier layers. It is conventional to model the actual active region structure with the barrier layers on each side of QW extending to infinity. It is also assumed that the potential wells associated with the active region are symmetric and rectangular, like the ones shown in Figs. 2.5(a) and 2.6(a). As discussed in [Blo96], there is good reason to believe that this so-called flat-band approximation is valid for QW lasers under typical operating conditions.

With the active region model described above, in the following subsections we first will solve the quantized electron and hole states for the one-dimensional potential wells in CB and VB respectively. Then we will discuss the in-plane subband structures in a parabolic band approximation.

2.4.1 Potential Wells and Quantized States

Fig. 2.7(a) shows a generic potential well diagram along the growth direction of the active region model used in the simulation. For the CB electrons and VB holes moving along the growth direction, they will experience potential wells with barrier heights equal to the CB offset ΔE_c and VB offset ΔE_v, respectively. As a result, energies are quantized in the potential wells. We define E_{cj} and E_{vj} as the energies of the jth quantized states in the CB and VB potential wells, respectively, and are measured relative to the bottoms of their corresponding potential wells. In the VB, there are HH and LH bands in our active region model. Therefore, there is the need to clarify that the HH quantized energy E_{HHj} and LH quantized energy E_{LHj} are measured from the bottoms of the HH and LH potential wells of barrier heights ΔE_{hh} and ΔE_{lh}, respectively. Finding E_{cj} and E_{vj} now becomes solving a quantum well problem.

Details of solving this quantum well problem can be found in many basic quantum mechanics textbooks, here we refer it to the treatment in [Cor93]. Basically, first it is to solve the Schrödinger's equation for each section of the active region (two barrier and one QW). Then by matching proper boundary conditions across two well-barrier interfaces, a pair of characteristic equations are obtained

$$\tan\left(k_{nj\perp}\frac{d_z}{2}\right)-\frac{m_{nj\perp}}{m_{nb}}\frac{\alpha_{nj}}{k_{nj\perp}} = 0 \quad \text{for } j \text{ is odd}, \tag{2.13}$$

$$\cot\left(k_{nj\perp}\frac{d_z}{2}\right)+\frac{m_{nj\perp}}{m_{nb}}\frac{\alpha_{nj}}{k_{nj\perp}} = 0 \quad \text{for } j \text{ is even}, \tag{2.14}$$

with

$$k_{nj\perp} = \frac{\sqrt{2m_{nj\perp}E_{nj}}}{\hbar}, \tag{2.15}$$

$$\alpha_{nj} = \frac{\sqrt{2m_{nb}(\Delta E_n - E_{nj})}}{\hbar}, \tag{2.16}$$

where d_z is the thickness of QW, $m_{nj\perp}$ is the growth-direction effective mass of the QW material, m_{nb} is the effective mass of the barrier material, $k_{nj\perp}$ is referred later in Chapter 3 to as the equivalent growth-direction component of the wavevector in QW associated with E_{nj}, α_{nj} is the magnitude of the complex wavevector in the barrier layer associated with E_{nj} and ΔE_n is the barrier height. The n subscript indicates CB for electrons and HH and LH bands in VB for heavy and light holes, respectively. Eqs. (2.13) and (2.14) can only be satisfied by a set of discrete energies E_{nj} which represent the bound solutions of the corresponding quantum well.

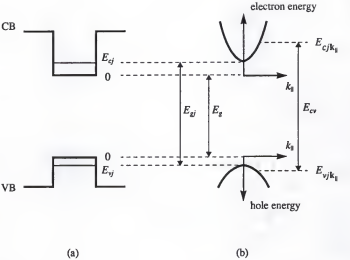

Figure 2.7 Generic diagrams of (a) the flat-band potential wells and (b) the parabolic subband structure of the QW active region model.

2.4.2 Parabolic In-plane Subband Structures

As discussed above, the potential wells are one-dimensional along the growth direction. Within the plane of the well, carriers (electrons and holes) are not confined and still behave like "free." Thus, for each quantized energy level in the QW, an in-plane energy subband exists, as shown in Fig. 2.7(b). The subband structure is usually characterized by defining an in-plane effective mass as [Kit86]

$$m_{nj\|} = \left[\frac{1}{\hbar^2}\frac{d^2E_{nj\mathbf{k}_\|}}{dk_\|^2}\right]^{-1}, \tag{2.17}$$

where $m_{nj\|}$ is the in-plane effective mass, $E_{nj\mathbf{k}_\|}$ is the in-plane energy measured relative to the bottom of the well and $\mathbf{k}_\|$ is the in-plane wavevector associated with $E_{nj\mathbf{k}_\|}$. The j subscript indicates the jth subband in the well and the n subscript indicates CB for electrons, HH and LH bands for heavy and light holes, respectively. If the parameter $m_{nj\|}$ is a constant with respect to $E_{nj\mathbf{k}_\|}$, the subband structure is said to be parabolic. In a nondegenerate band, such as the CB (excluding spin degeneracy), all the subbands are assumed to be parabolic and the electron effective masses along the $\perp$ and $\|$ directions are identical ($m_{cj\perp} = m_{cj\|}$). However, the in-plane subband structure in a degenerate band, such as the VB, is more complicated, since band coupling between the HH and LH bands can be very strong. In that case, the VB subbands become nonparabolic band due to this so-called valence band mixing effect. Since the quantum wells are under biaxial compressive strain for the laser structures studied in this work, the LH band is pushed away from the HH bands due to the shear component of the strain. This greatly reduces the valence band mixing effect between the HH and LH bands and allows us to assume that the subband structures in the VB are also parabolic. In any event, the growth-direction HH and LH effective masses are not affected by the strain and are given by [Cor93]

$$m_{hh\perp} = \frac{1}{\gamma_1 - 2\gamma_2}\frac{\hbar^2}{2}, \quad m_{lh\perp} = \frac{1}{\gamma_1 + 2\gamma_2}\frac{\hbar^2}{2}, \tag{2.18}$$

where the material constants γ_1 and γ_2 are referred to as the Luttinger parameters [Lut56]. In the high strain approximation, the in-plane HH and LH effective masses can be expressed in close forms with in terms of Luttinger parameters γ_1 and γ_2 (in the units of $\hbar^2/2m_o$) [Cor93]

$$m_{hh\parallel} = \frac{1}{\gamma_1 + \gamma_2}\frac{\hbar^2}{2}, \quad m_{lh\parallel} = \frac{1}{\gamma_1 - \gamma_2}\frac{\hbar^2}{2}. \tag{2.19}$$

From the preceding discussion of strain and by comparing Eqs. (2.18) and (2.19), we find that not only do the HH and LH bands split apart, but also the HH band becomes "lighter" and the LH band becomes "heavier" in the plane of compression. Thus, this is contrary to the bulk material where the effective masses along ⊥ and ∥ directions are identical.

2.4.3 Numerical Results

InGaAs QW. For the $In_{0.15}Ga_{0.85}As$ QW, we obtain electron effective mass $m_c = m_{cj\perp} = m_{cj\parallel} = 0.061m_o$, Luttinger parameters $\gamma_1 = 8.773$, $\gamma_2 = 3.041$ and for the GaAs barrier, we have $m_c = m_{cb} = 0.067m_o$, $\gamma_1 = 6.85$ and $\gamma_2 = 2.1$ using the material parameters for the InGaAs/AlGaAs system summarized in Table III of [Cor93]. Plugging the numerical values for γ_1 and γ_2 in Eqs. (2.18) and (2.19), we obtain $m_{hh\perp} = 0.372m_o$, $m_{lh\perp} = 0.067m_o$, $m_{hh\parallel} = 0.085m_o$ and $m_{lh\parallel} = 0.174m_o$ for the $In_{0.15}Ga_{0.85}As$ QW and $m_{hh\perp} = 0.377m_o$ and $m_{lh\perp} = 0.091m_o$ for the GaAs barrier. Having all the values of effective masses plugged into Eqs. (2.13) through (2.16), we solve the quantized levels for the CB and VB (HH and LH) potential wells of width $d_z = 8$ nm, as shown in Fig. 2.5(b). The calculation yields one electron subband in the CB ($E_{C1} = 31.6$ meV relative to the bottom of CB potential well), two HH subbands ($E_{HH1} = 9.2$ meV and $E_{HH2} = 35.4$ meV relative to the bottom of HH potential well) and one LH subband ($E_{LH1} = 6.6$ meV relative to the bottom of LH potential well) in the VB. Numerical values of the material parameters used in this work for the strained $In_{0.15}Ga_{0.85}As$ QW/GaAs barrier system are summarized in Table 2.1.

CdZnSe QW. For the $Cd_{0.3}Zn_{0.7}Se$ QW, we obtain electron effective mass $m_c = m_{cj\perp} = m_{cj\parallel} = 0.139m_o$, Luttinger parameters $\gamma_1 = 4.495$, $\gamma_2 = 1.206$ and for the $ZnS_{0.06}Se_{0.94}$ barrier, we have $m_c = m_{cb} = 0.152m_o$, $\gamma_1 = 4.3$ and $\gamma_2 = 1.14$ using the ternary material parameters for CdZnSe/ZnSSe system derived in Appendix A. Using the numerical values for γ_1 and γ_2 in Eqs. (2.18) and (2.19), we obtain $m_{hh\perp} = 0.480m_o$, $m_{lh\perp} = 0.145m_o$, $m_{hh\parallel} = 0.175m_o$ and $m_{lh\parallel} = 0.304m_o$ for the $Cd_{0.3}Zn_{0.7}Se$ QW and $m_{hh\perp} = 0.571m_o$ and $m_{lh\perp} = 0.157m_o$ for the $ZnS_{0.06}Se_{0.94}$ barrier. Plugging all the values of effective masses into Eqs. (2.13) through (2.16), we solve the quantized levels for the CB, HH and LH potential wells of width $d_z = 4$ nm, as shown in Fig. 2.6(b). The calculation yields one electron subband in the CB ($E_{C1} = 62.6$ meV), two HH subbands ($E_{HH1} = 23.9$ meV, $E_{HH2} = 90.3$ meV) and one LH subband ($E_{LH1} = 23.1$ meV) in the VB. Numerical values of the material parameters used in this work for the strained $Cd_{0.3}Zn_{0.7}Se$ QW/$ZnS_{0.06}Se_{0.94}$ barrier system are summarized in Table 2.2.

Comparison. As shown above, electron and hole effective masses of the CdZnSe/ZnSSe system are much larger than those of the InGaAs/GaAs system. In Section 2.6.3, the difference in the effective masses will be shown to play an important role in the difference of the transparency carrier densities between the two QW diode laser systems.

2.5 Single-Particle Gain and Spontaneous Emission Functions

2.5.1 Transition Energy

In Section 2.4, we have shown how the strain modifies the bandgap of a QW and how the quantum effect modifies its strained bandgap. As illustrated in Fig. 2.7(a), we define E_{gj} as the "modified" energy gap between the *j*th conduction and valence subbands

$$E_{gj} = E_g + E_{cj} + E_{vj}, \tag{2.20}$$

where E_g is E_g(HH) for the C-HH strained bandgap or E_g(LH) for the C-LH strained bandgap, E_{cj} and E_{vj} are the quantized energy levels in the QW. For an electron-hole-pair participating in a transition with energy E_{cv}, as depicted in Fig. 2.7(b), we obtain

$$E_{cv} = E_g + E_{cj\mathbf{k}_\parallel} + E_{vj\mathbf{k}_\parallel}, \tag{2.21}$$

where $E_{cj\mathbf{k}_\parallel}$ and $E_{vj\mathbf{k}_\parallel}$ are the energies of electrons and holes respectively participating in this transition and are measured relative to the bottoms of CB and VB potential wells. In terms of the in-plane wavevector $\mathbf{k}_\parallel$, the expressions for $E_{cj\mathbf{k}_\parallel}$ and $E_{vj\mathbf{k}_\parallel}$ are given by

$$E_{cj\mathbf{k}_\parallel} = E_{cj} + \frac{\hbar^2 k_\parallel^2}{2m_{cj\parallel}}, \quad E_{vj\mathbf{k}_\parallel} = E_{vj} + \frac{\hbar^2 k_\parallel^2}{2m_{vj\parallel}}, \tag{2.22}$$

where $m_{cj\parallel}$ and $m_{vj\parallel}$ are the in-plane effective masses and both conduction and valence subbands are assumed to be parabolic as discussed in Section 2.4.2.

2.5.2 Gain and Spontaneous Emission

In simulating the operating characteristics of standard QW diode lasers, it is customary to utilize two functions which describe the dependence of QW gain and spontaneous emission on photon energy $\hbar\omega$. In deriving these functions, defining $g(\hbar\omega)$ as the spectral gain function and $R_{sp}(\hbar\omega)$ as the spontaneous emission function, approximations with various levels of accuracy can be made. In the first level approximation, one ignores many-body effects and assumes that electrons trapped in the QW interact only with the electromagnetic field. In this "single-particle" model, where $\hbar\omega$ is equal to the transition energy E_{cv}, we have $g(\hbar\omega) = g(E_{cv})$ and $R_{sp}(\hbar\omega) = R_{sp}(E_{cv})$. $g(E_{cv})$ and $R_{sp}(E_{cv})$ are calculated by summing over the contributions from all the allowed subband transition pairs as given by

$$g(E_{cv}) = \sum_j g_j(E_{cv}), \tag{2.23}$$

$$R_{sp}(E_{cv}) = \sum_j R_{spj}(E_{cv}), \tag{2.24}$$

where $g_j(E_{cv})$ and $R_{spj}(E_{cv})$ are the spectral gain function and spontaneous emission function for an allowed subband transition pair, respectively. Since there is only one subband in the CB in our structure, there are two allowed transition pairs, viz. C1-HH1 and C1-LH1. In the single-particle model, one ignores many-body effects and assumes that momentum is conserved (k-selection holds) in the photon emission and absorption processes. In this case, it can be shown that $g_j(E_{cv})$ and $R_{spj}(E_{cv})$ are given by [Cor93]

$$g_j(E_{cv}) = \left(\frac{1}{\hbar\omega}\right)\frac{\pi e^2 \hbar}{\varepsilon_o c m_o^2 \bar{n}}|M_T|^2 \rho_{red}\,[f_c(E_{cj\mathbf{k}_\parallel}) + f_h(E_{vj\mathbf{k}_\parallel}) - 1]\,, \tag{2.25}$$

$$R_{spj}(E_{cv}) = (\hbar\omega)\frac{e^2 \bar{n}}{\pi \hbar^2 \varepsilon_o c^3 m_o^2}|\overline{M}_T|^2 \rho_{red}\,[f_c(E_{cj\mathbf{k}_\parallel}) f_h(E_{vj\mathbf{k}_\parallel})]\,, \tag{2.26}$$

where e is the electron charge, ε_o is the vacuum permittivity, c is the vacuum light speed, m_o is the electron rest mass, $\bar{n}$ is the background refractive index of the QW material, $|M_T|^2$ is the transition matrix element, $|\overline{M}_T|^2$ is the average transition matrix element, ρ_{red} is the reduced density of states, f_c is the Fermi-Dirac distribution for CB electrons and $f_h \equiv 1 - f_v$ is the distribution for VB holes. The transition matrix element $|M_T|^2$ is given by

$$\frac{|M_T|^2}{|M|^2} = \begin{cases} \frac{1}{2} + \frac{1}{2}\cos^2\theta_j & \text{for C-HH TE gain} \\ 1 - \cos^2\theta_j & \text{for C-HH TM gain} \\ \frac{5}{6} - \frac{1}{2}\cos^2\theta_j & \text{for C-LH TE gain} \\ \frac{1}{3} + \cos^2\theta_j & \text{for C-LH TM gain} \end{cases}\,, \tag{2.27}$$

where

$$|M|^2 = \left(\frac{m_o}{m_c} - 1\right)\frac{(E_g + \Delta)}{2\left(E_g + \frac{2}{3}\Delta\right)} m_o E_g\,, \tag{2.28}$$

$$\cos^2\theta_j = \frac{(E_{cj} + E_{vj})\,\dfrac{m_{rj\perp}}{m_{rj\parallel}}}{(E_{cv} - E_g - E_{cj} - E_{vj}) + (E_{cj} + E_{vj})\,\dfrac{m_{rj\perp}}{m_{rj\parallel}}}\,. \tag{2.29}$$

For the $In_xGa_{1-x}As$ QW, $|M|^2$ can be simplified and expressed as a function of indium mole fraction [Cor93]

$$|M|^2 = \frac{1}{2}(28.8 - 6.6x)\ (em_o)\,. \tag{2.30}$$

The parameters $m_{rj\perp}$ and $m_{rj\parallel}$ are the reduced effective masses along the growth and in-plane directions, respectively and are defined as follows:

$$\frac{1}{m_{rj\perp}} = \frac{1}{m_{cj\perp}} + \frac{1}{m_{vj\perp}}\,, \quad \frac{1}{m_{rj\parallel}} = \frac{1}{m_{cj\parallel}} + \frac{1}{m_{vj\parallel}}\,. \tag{2.31}$$

The average transition matrix element $|\overline{M}_T|^2$ can be shown to be

$$\frac{|\overline{M}_T|^2}{|M|^2} = \frac{2}{3} \quad \text{for both C-HH and C-LH spontaneous emission}\,. \tag{2.32}$$

Derivations of Eqs. (2.27) and (2.32), as well as Eq. (2.29) which shows that θ_j is a function of transition energy, are given in Appendix B. The reduced density of states ρ_{red} (spin not included) is given by [Cor93]

$$\rho_{red} = \begin{cases} \dfrac{m_{rj\parallel}}{2\pi\hbar^2}\left(\dfrac{1}{d_z}\right) & \text{for } E_{cv} \geq E_{gj} \\ 0 & \text{for } E_{cv} < E_{gj} \end{cases}\,. \tag{2.33}$$

The Fermi-Dirac functions f_c and f_h are given by

$$f_c(E_{cj\mathbf{k}_\parallel}) = \frac{1}{1 + \exp\left[\,(E_{cj\mathbf{k}_\parallel} - E_{fc})/k_BT\right]}\,, \tag{2.34}$$

$$f_h(E_{vj\mathbf{k}_\parallel}) = \frac{1}{1 + \exp\left[\,(E_{vj\mathbf{k}_\parallel} - E_{fv})/k_BT\right]}\,, \tag{2.35}$$

where E_{fc} and E_{fv} are the quasi-Fermi levels in the CB and VB respectively and are measured from the CB and VB edges into the bands, k_B is the Boltzmann constant and T is the temperature of the structure. For parabolic conduction and valence subbands, we can write the electron concentration N and hole concentration P in the quantum well as

$$N = \frac{k_BT}{\pi\hbar^2 d_z}\sum_j m_{cj\parallel}\ln\left\{1 + \exp\left[-(E_{cj} - E_{fc})/k_BT\right]\right\} \tag{2.36}$$

$$P = \frac{k_B T}{\pi \hbar^2 d_z} \sum_j m_{vj\parallel} \ln \{ 1 + \exp [- (E_{vj} - E_{fv}) / k_B T] \} \tag{2.37}$$

The summation is over all subbands which includes HH and LH subbands for P in the VB. Under the condition of overall charge neutrality in the quantum well, we have $N = P$. For a given value of N, we can solve for the values of E_{fc} and E_{fv} which satisfy Eqs. (2.36) and (2.37) at a given T.

2.6 Simulation Results

The general procedure for calculating the single-particle $g(E_{cv})$ and $R_{sp}(E_{cv})$ functions is summarized as follows: (1) Specify N and T; (2) Input numerical values of material parameters discussed in Section 2.4.3; (3) Input the quantized energy levels solved in Section 2.4.3; (4) Solve E_{fc} and E_{fv} from a plot of E_{fc} and E_{fv} as a function of N using Eqs. (2.36) and (2.37); (5) Calculate $g(E_{cv})$ and $R_{sp}(E_{cv})$ using Eqs. (2.23) through (2.26).

2.6.1 InGaAs QW

Fig. 2.8 shows plots of E_{fc} and E_{fv} vs. N for the 8 nm $In_{0.15}Ga_{0.85}As$ strained QW with GaAs barriers. Because the QW is under biaxial compressive strain, the first VB subband to be filled up with holes is a HH subband. From Eq. (2.27), it indicates that the TE transition matrix element is stronger than its TM counterpart for a C-HH transition. As a result, TE gain dominates over TM gain for the InGaAs strained QW lasers. Typical TE gain spectra for $N = 1.3 \times 10^{18}$ and 1.7×10^{18} cm^{-3} at $T = 300$ K, calculated from Eqs. (2.23) and (2.25), are shown in Fig. 2.9(a). It shows that gain increases with increasing N. The spectral position of the peak gain occurs at $E_{g1,hh}$, which corresponds to the energy gap between C1 and HH1 subbands defined in Eq. (2.20), and remains there as N increases. Since no transition is allowed for E_{cv} smaller than $E_{g1,hh}$, the gain for photons with energies below

$E_{g1,hh}$ is zero. Fig. 2.9(b) shows the spontaneous emission spectra for the corresponding N, calculated from Eqs. (2.24) and (2.26). Two unrealistic discontinuous peaks occurring at $E_{g1,hh}$ and $E_{g1,lh}$ in the spontaneous emission spectra are due to the step-like density of states in a QW structure [Cor93]. For the gain spectra shown in Fig. 2.9(a), only the discontinuity at $E_{g1,hh}$ is obvious. The one at $E_{g1,lh}$ should also show up, but it is in the absorption region which is beyond the scale of the plot.

2.6.2 CdZnSe QW

Fig. 2.10 shows plots of E_{fc} and E_{fv} vs. N for the 4 nm $Cd_{0.3}Zn_{0.7}Se$ strained QW with $ZnS_{0.06}Se_{0.94}$ barriers. Typical TE gain spectra for $N = 4.6 \times 10^{18}$ and 5.4×10^{18} cm^{-3} at $T = 300$ K, calculated from Eqs. (2.23) and (2.25), are shown in Fig. 2.11(a). Similar to the gain spectra in Fig. 2.9(a), only the discontinuity at $E_{g1,hh}$ is obvious. In Chapter 5, when we discuss the absorption spectra in the CdZnSe QW lasers, we will show clearly that both discontinuities exist within single-particle model. Fig. 2.11(b) shows the spontaneous emission spectra for the corresponding N, calculated from Eqs. (2.24) and (2.26). They also show unrealistic spectral features of discontinuity due to the step-like density of states for C-HH1 and C-LH1 transitions.

2.6.3 Comparison

From Eq. (2.25), we see that when

$$f_c(E_{cjk_\|}) + f_h(E_{vjk_\|}) - 1 > 0, \tag{2.38}$$

$g_j(E_{cv})$ is positive and an incoming light wave with photon energy E_{cv} will be amplified by the material. Using Eqs. (2.34) and (2.35) in Eq. (2.38), one can show that this inequality is equivalent to saying that

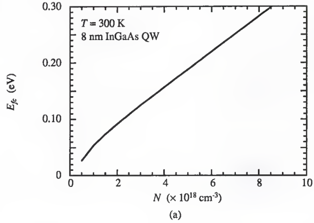

(a)

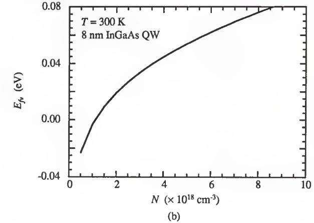

(b)

Figure 2.8 Quasi-Fermi level as a function of carrier density for (a) CB electrons and (b) VB holes of the 8 nm $In_{0.15}Ga_{0.85}As/GaAs$ QW.

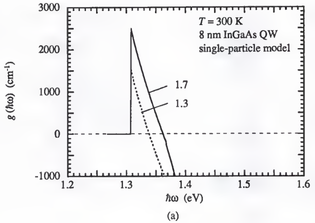

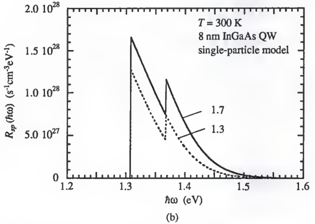

Figure 2.9 Single-particle (a) TE gain and (b) spontaneous emission spectra for the 8 nm $In_{0.15}Ga_{0.85}As/GaAs$ QW at various indicated carrier densities (in units of 10^{18} cm^{-3}) at room temperature.

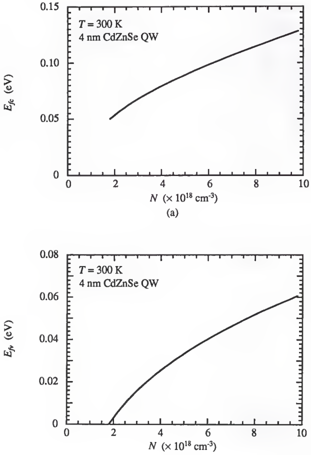

(a)

(b)

Figure 2.10 Quasi-Fermi level as a function of carrier density for (a) CB electrons and (b) VB holes of the 4 nm $Cd_{0.3}Zn_{0.7}Se/ZnS_{0.06}Se_{0.94}$ QW.

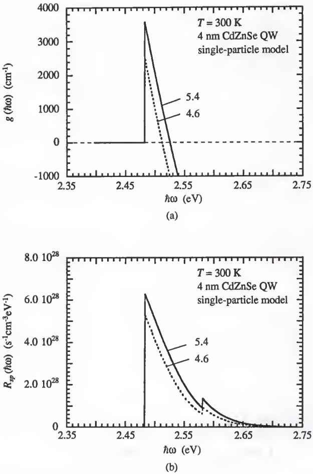

Figure 2.10 Single-particle (a) TE gain and (b) spontaneous emission spectra for the 4 nm $Cd_{0.3}Zn_{0.7}Se/ZnS_{0.06}Se_{0.94}$ QW at various indicated carrier densities (in units of 10^{18} cm^{-3}) at room temperature.

$$E_{gj} < E_{cv} < E_{gj} + E_{fc} + E_{fv} \equiv \Delta E_f \qquad (2.39)$$

is the requirement for gain at a photon energy E_{cv}. In other words, the quasi-Fermi level separation ΔE_f must be greater than the QW subband energy gap E_{gj} (or $\Delta E_f - E_{gj} > 0$) to achieve optical gain in the material. Eq. (2.39) is similar to the one for bulk semiconductors given in [Cas78, Cor93] where E_{gj} is replaced by bulk E_g. For a QW under biaxial compressive strain, E_{gj} indicates the smallest C1-HH1 subband energy gap $E_{g1,hh}$. Plots of ($\Delta E_f - E_{g1,hh}$) vs. N are shown in Fig. 2.12 for both the InGaAs QW and CdZnSe QW structures studied. The cross-over of the ($\Delta E_f - E_{g1,hh}$) vs. N curve on the N-axis is defined as the transparency carrier density N_{tr}, which is the electron-hole plasma density required to provide the quasi-Fermi level separation so that the material will become transparent for photon energy equal to E_{gj} according to Eq. (2.39). Optical gain in the material is attained when we inject a carrier density $N > N_{tr}$, such that $\Delta E_f > E_{g1,hh}$. From the curves, we find that $N_{tr} \cong 0.9 \times 10^{18}$ cm^{-3} for the strained InGaAs QW which is smaller than $N_{tr} \cong 3.1 \times 10^{18}$ cm^{-3} for the strained CdZnSe QW. This is mainly due to that the density of states for the CdZnSe QW is larger than that for the InGaAs QW. From Eq. (2.33), the density of states is found to be proportional to the carrier effective masses of the material system and, as discussed in Section 2.4.3, the effective masses of the CdZnSe QW are much larger than those of the InGaAs QW. Another observation is that the slope of the curve for the InGaAs QW is larger than that for the CdZnSe QW. This means that carrier fills up the subbands in the InGaAs QW faster than in the CdZnSe QW. Effect of density of states on the transparency condition is discussed in great detail in [Cor93]. In Chapter 4, we will see how the difference in N_{tr} contributes to the difference in transparency current densities for the two material systems.

2.7 Summary

Optical gain and spontaneous emission spectra are calculated for both InGaAs and

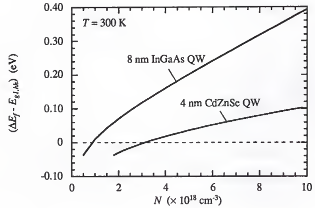

Figure 2.12 Difference between the quasi-Fermi level separation and C1-HH1 QW sub-band energy gap as a function of carrier density for both the 8 nm $In_{0.15}Ga_{0.7}As/GaAs$ and the 4 nm $Cd_{0.3}Zn_{0.7}Se/ZnS_{0.06}Se_{0.94}$ QW at room temperature.

CdZnSe QW laser structures using the single-particle model. Since the measured spectra do not have sharp features, it is clear that this single-particle model is incomplete. In Chapter 3, we show that when many-body effects are incorporated into the single-particle model, realistic gain and spontaneous spectra are obtained. However, it is interesting to note that in the limit of very thick QWs, the single-particle model gives realistic-looking spectra. This is due to the fact that the stair-step density of states function gradually smooths out as QW thickness increases [Cor93]. As a consequence, the single-particle model applied to thick active layer lasers generates spectra which look realistic and it is not obvious that the model is incomplete.

CHAPTER 3
MANY-BODY EFFECTS

3.1 Introduction

In Chapter 2, we have discussed the optical gain and spontaneous emission functions based on a single-particle model where mutual interactions among carriers are ignored. However, upon current injection into the semiconductor QW diode lasers, the carrier densities in the QW are typically on the order of $10^{17} \sim 10^{18}$ cm^{-3}. In the presence of such high density of electron-hole plasma, mutual interactions among the carriers are expected to be important. These mutual interactions are usually referred as "many-body effects" and include carrier scattering (CS), bandgap renormalization (BGR) and Coulomb enhancement (CE). In this chapter, effects of CS, BGR and CE on the single-particle $g\,(E_{cv})$ and $R_{sp}\,(E_{cv})$ functions will be discussed sequentially.

3.2 Carrier Scattering (CS)

3.2.1 Gain and Spontaneous Emission Functions

In high quality QW laser material, CS is the main contributor to spectral broadening and is taken into account by convolving the single-particle $g_j\,(E_{cv})$ and $R_{spj}\,(E_{cv})$ functions for a given subband transition pair with a spectral-broadening lineshape function. The convolved gain function can be expressed as [Asa93]

$$g_B(\hbar\omega) = Real\{\sum_j \int_{E_{gj}}^{\infty} g_j(E_{cv}) \times L_j(\hbar\omega - E_{cv})\left[1 - i\frac{E_{cv} - \hbar\omega}{\Gamma_{cv}(\hbar\omega, E_{cv})}\right] dE_{cv}\Big\} \tag{3.1}$$

and the convolved spontaneous emission is given by

$$R_{spB}(\hbar\omega) = Real\{\sum_j \int_{E_{gj}}^{\infty} R_{spj}(E_{cv}) \times L_j(\hbar\omega - E_{cv})\left[1 - i\frac{E_{cv} - \hbar\omega}{\Gamma_{cv}(\hbar\omega, E_{cv})}\right] dE_{cv}\Big\}, \tag{3.2}$$

where the notation *Real* refers to the real part of a complex quantity. The subscript B indicates the spectral broadening due to carrier scattering. Since $g_j(E_{cv})$, $R_{spj}(E_{cv})$ and, as shown later, $L_j(\hbar\omega - E_{cv})$ are all real quantities, Eqs. (3.1) and (3.2) are often rewritten as

$$g_B(\hbar\omega) = \sum_j \int_{E_{gj}}^{\infty} g_j(E_{cv}) L_j(\hbar\omega - E_{cv})\, dE_{cv} \tag{3.3}$$

$$R_{spB}(\hbar\omega) = \sum_j \int_{E_{gj}}^{\infty} R_{spj}(E_{cv}) L_j(\hbar\omega - E_{cv})\, dE_{cv}, \tag{3.4}$$

by dropping the square brackets which are the only complex terms in these equations and thus dropping the notations *Real*. Eqs. (3.3) and (3.4) mean that, for a given subband transition pair, the transitions with energy $E_{cv} \neq \hbar\omega$ contribute to optical gain and spontaneous emission at $\hbar\omega$ with the weight $L_j(\hbar\omega - E_{cv})$ and the total optical gain and spontaneous emission are the summation over the contributions from all the allowed subband transition pairs.

The width of the spectral-broadening lineshape function is closely related to the time constants associated with various carrier scattering processes [Asa93, Yam87]. The parameters τ_{cj} and τ_{vj} denote the electron scattering time and hole scattering time in the *j*th subbands of CB and VB respectively. Various CS processes contributing to τ_{cj} are electron-electron (e-e), electron-hole (e-h) and electron-LO phonon (e-LO) and those contributing to τ_{vj} are hole-hole (h-h), hole-electron (h-e) and hole-LO phonon (h-LO). Details concerning the calculation of the these scattering times can be found in [Asa93].

The non-Lorentzian form used for the lineshape function is given by [Asa93, Hsu97a, Yam87]

$$L_j(\hbar\omega - E_{cv}) \cong \frac{1}{\pi} \frac{\Gamma_{cv}(\hbar\omega, E_{cv})}{(\hbar\omega - E_{cv})^2 + \Gamma_{cv}^2(\hbar\omega, E_{cv})}, \tag{3.5}$$

where

$$\Gamma_{cv}(\hbar\omega, E_{cv}) = \Gamma_{cj\mathbf{k}_\parallel}(\hbar\omega - E_{cv} + E_{cj\mathbf{k}_\parallel}) + \Gamma_{vj\mathbf{k}_\parallel}(\hbar\omega - E_{cv} + E_{vj\mathbf{k}_\parallel}). \tag{3.6}$$

This lineshape function differs from a Lorentzian function in that Γ_{cv} depends on photon energy $\hbar\omega$. $\Gamma_{vj\mathbf{k}_\parallel}$ for the jth VB subband can be approximated as [Asa93]

$$\Gamma_{vj\mathbf{k}_\parallel}(E) \cong \frac{\hbar}{2\tau_{vj}} \frac{1 + e^{(E - E_{vj\mathbf{k}_\parallel} - E_{fv})/kT}}{1 + e^{-E_{fv}/kT}} e^{-K\left|E - E_{vj\mathbf{k}_\parallel}\right|/kT}, \tag{3.7}$$

where

$$K = \frac{e^4 \tau_{vj}}{48\pi\varepsilon_o^2\varepsilon_s^2\hbar kT d_{vj}^2} \frac{T(0, k_{vj\perp}, k_{vj\perp})}{1 + e^{-E_{fv}/kT}} \left(\frac{2m_{vj\parallel}kT}{\hbar^2}\right)^2, \tag{3.8}$$

with

$$\begin{aligned} T(0, k_{vj\perp}, k_{vj\perp}) = \{ & \frac{2}{\lambda_s^2} + \frac{1}{\lambda_s^2 + 4k_{vj\perp}^2} - \frac{2}{d_{vj}\lambda_s}[1 - \exp(-d_{vj}\lambda_s)] \\ & \left[\frac{1}{\lambda_s^2} - \frac{\lambda_s^2 + 8k_{vj\perp}^2}{(\lambda_s^2 + 4k_{vj\perp}^2)^2} \right. \\ & \left. + \frac{d_{vj}k_{vj\perp}(d_{vj}k_{vj\perp} - \pi)(\lambda_s^2 - 4k_{vj\perp}^2)}{4(\lambda_s^2 + 4k_{vj\perp}^2)^2[\exp(d_{vj}\lambda_s) - 1]}\right]\}^2 \end{aligned} \quad . \tag{3.9}$$

The parameter λ_s is the inverse screening length and is given by [Asa93]

$$\lambda_s^2 = \frac{e^2}{\pi\hbar^2\varepsilon_o\varepsilon_s} \sum_j \left[\frac{m_{cj\parallel} f_c(E_{cj})}{d_{cj}} + \frac{m_{vj\parallel} f_v(E_{vj})}{d_{vj}}\right], \tag{3.10}$$

where ε_s is the static dielectric constant of the quantum well material, d_{nj} is the effective well width for the jth subband in the CB and VB ($n = c$ and v, respectively). The summation over j means that the screening effect is considered with inclusion of all the subbands in CB and VB. d_{nj} is defined by [Hsu97a]

$$d_{nj} = j\frac{\pi\hbar}{\sqrt{2m_n E_{nj}}} = j\frac{\pi}{k_{nj\perp}}, \tag{3.11}$$

where the parameter $k_{nj\perp}$ is the equivalent growth-direction component of the wavevector associated with the quantized energy level E_{nj}. For the jth CB subband, $\Gamma_{cjk_\parallel}$ can be calculated by replacing all the subscripts v with c in Eqs. (3.7) through (3.9). Details concerning the derivation of Eq. (3.7) and the associated parameters are given in [Asa93].

3.2.2 Simulation Results

InGaAs QW. The convolved TE gain and spontaneous emission spectra with inclusion of spectral broadening due to carrier scattering are plotted as the solid curves in Figs. 3.1(a) and (b), respectively, at $N = 1.7 \times 10^{18}$ cm^{-3} and $T = 300$ K. It is evident that these spectra are broadened and smoothed relative to their single-particle counterparts which are replotted as the dotted curves in Figs. 3.1(a) and (b) for easy comparison. The peak gain is reduced significantly and its spectral location is shifted away from the C1-HH1 subband energy gap $E_{g1,\,hh}$ to higher photon energy (in this case by about 11 meV). As discussed later in Chapter 4, this shift is important in determining the dependence of lasing wavelength on cavity length.

CdZnSe QW. The solid curves in Figs. 3.2(a) and (b) are the convolved TE gain and spontaneous emission spectra, respectively, of their single-particle counterparts plotted as the dotted curves for the 4 nm $Cd_{0.3}Zn_{0.7}Se/ZnS_{0.06}Se_{0.94}$ QW at $N = 5.4 \times 10^{18}$ cm^{-3} and T =300 K. In this case, peak gain is also reduced and its spectral location is blue-shifted from $E_{g1,\,hh1}$ to higher photon energy by about 11.5 meV.

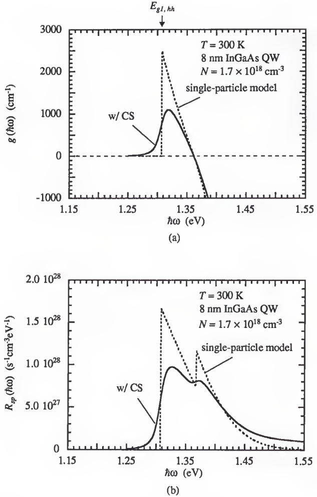

Figure 3.1 The convolved (a) TE gain and (b) spontaneous emission spectra (solid curves) of their single-particle counterparts (dotted curves) for the 8 nm $In_{0.15}Ga_{0.85}As/GaAs$ QW at $N = 1.7 \times 10^{18}$ cm^{-3} and $T = 300$ K. The convolution takes into account the spectral broadening due to carrier scattering.

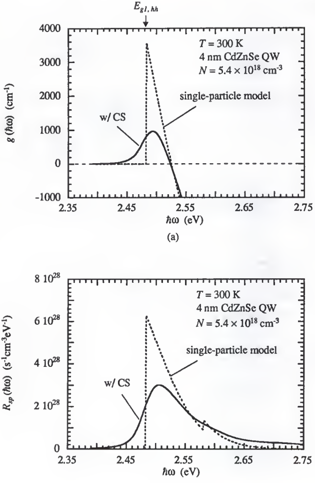

(a)

(b)

Figure 3.2 The convolved (a) TE gain and (b) spontaneous emission spectra (solid curves) of their single-particle counterparts (dotted curves) for the 4 nm $Cd_{0.3}Zn_{0.7}Se/ZnS_{0.06}Se_{0.94}$ QW at $N = 5.4 \times 10^{18}$ cm^{-3} and $T = 300$ K. The convolution takes into account the spectral broadening due to carrier scattering.

3.3 Bandgap Renormalization (BGR)

3.3.1 Plasma Screening

One of the most important many-body interactions in an electron-hole plasma (EHP) is the screening of the Coulomb potential. In a two-dimensional (2D) quantum well system, the Fourier transformation of the unscreened Coulomb potential in the real space to the momentum space (or wavevector **k** space) is given by [Cho94, Hau90]

$$V_{q_\parallel} = \frac{e^2}{2\varepsilon_o\varepsilon_s q_\parallel A} \tag{3.12}$$

where A is the in-plane area of the quantum well. The parameter $q_\parallel$ is the magnitude of a $\mathbf{q}_\parallel$ vector which is defined as the difference between in-plane wavevector $\mathbf{k}_\parallel'$ and $\mathbf{k}_\parallel$, that is $\mathbf{q}_\parallel = \mathbf{k}_\parallel' - \mathbf{k}_\parallel$. Given the angle θ between $\mathbf{k}_\parallel'$ and $\mathbf{k}_\parallel$, q‖ can be given from the law of cosine

$$q_\parallel^2 = k_\parallel'^2 + k_\parallel^2 - 2k_\parallel' k_\parallel \cos\theta . \tag{3.13}$$

Defining the exciton Bohr radius a_o and exciton Rydberg constant E_R as (in M.K.S. units) [Cho94, Hau90]

$$a_o = \frac{4\pi\hbar^2\varepsilon_o\varepsilon_s}{e^2 m_{rj\parallel}}, \tag{3.14}$$

$$E_R = \frac{\hbar^2}{2m_{rj\parallel}a_o^2}, \tag{3.15}$$

we obtain

$$a_o E_R = \frac{e^2}{8\pi\varepsilon_o\varepsilon_s}, \tag{3.16}$$

where $a_o E_R$ depends only on the static dielectric constant ε_s of the material. Unlike in [Cho94, Hau90], we use the in-plane reduced effective mass discussed in Chapter 2 to take the effective-mass anisotropy into account in Eqs. (3.14) and (3.15). Using (3.16) in Eq.

(3.12), the unscreened Coulomb potential can be expressed in terms of a_o and E_R as

$$V_{q_\parallel} = \frac{4\pi a_o E_R}{q_\parallel A}. \tag{3.17}$$

The screened Coulomb potential is given by [Cho94, Hau90]

$$V_{sq_\parallel} = \frac{V_{q_\parallel}}{\varepsilon_\parallel (q_\parallel, \omega)}, \tag{3.18}$$

where $\varepsilon_\parallel (q_\parallel, \omega)$ is the longitudinal dielectric function and is frequency dependent (dynamic). At high temperature where screening is governed by free carriers (not excitons), screening effect can be described within the so-called random phase approximation (RPA) [Cho94, Hau90]. Replacing a continuum of poles in RPA by a single effective plasmon-pole and neglecting the frequency dependence of screening effect, one obtains the much simpler static plasmon-pole approximation (SPPA) [Cho94, Hau90]. In this case, the longitudinal dielectric function can be expressed as

$$\frac{1}{\varepsilon_\parallel (q_\parallel, 0)} = 1 - \frac{\omega_{pl}^2}{\omega_{q_\parallel}^2}, \tag{3.19}$$

where ω_{pl} is the plasma frequency and $\omega_{q_\parallel}$ is the effective plasmon frequency. For a general multi-subband QW system, ω_{pl} can be expressed as [Cam94]

$$\begin{aligned} \omega_{pl}^2 &= A V_{q_\parallel} q_\parallel^2 \sum_j \left(\frac{n_j}{m_{cj\parallel}} + \frac{p_j}{m_{vj\parallel}} \right) \\ &= 4\pi a_o E_R q_\parallel \sum_j \left(\frac{n_j}{m_{cj\parallel}} + \frac{p_j}{m_{vj\parallel}} \right) \end{aligned}, \tag{3.20}$$

where the summation is overall all the conduction and valence subbands. In the last form of ω_{pl}^2, the expression for $V_{q_\parallel}$ in Eq. (3.17) is used. The effective plasmon frequency $\omega_{q_\parallel}$ is related to ω_{pl} by [Cho94, Hau90]

$$\omega_{q_\parallel}^2 = \left(1 + \frac{q_\parallel}{\lambda_s} \right) \omega_{pl}^2 + \left(\frac{\hbar q_\parallel^2}{2 m_{rj\parallel}} \right)^2, \tag{3.21}$$

where the inverse screening length λ_s is given in Eq. (3.10) with inclusion of all the subbands. Dividing both sides of Eq. (3.21) by ω_{pl}^2 and taking the inverse, we obtain

$$\frac{\omega_{pl}^2}{\omega_{q_\parallel}^2} = \frac{1}{\left(1+\frac{q_\parallel}{\lambda_s}\right)+\frac{1}{\omega_{pl}^2}\left(\frac{\hbar q_\parallel^2}{2m_{rj\parallel}}\right)^2} \tag{3.22}$$

and therefore,

$$1-\frac{\omega_{pl}^2}{\omega_{q_\parallel}^2} = \left[\frac{q_\parallel}{\lambda_s}+\frac{1}{\omega_{pl}^2}\left(\frac{\hbar q_\parallel^2}{2m_{rj\parallel}}\right)^2\right]\left[1+\frac{q_\parallel}{\lambda_s}+\frac{1}{\omega_{pl}^2}\left(\frac{\hbar q_\parallel^2}{2m_{rj\parallel}}\right)^2\right]^{-1}. \tag{3.23}$$

Before further expanding Eq. (3.23), we introduce several new parameters which, in analogy to a_o and E_R defined Eqs. (3.14) and (3.15), are defined as

$$a_{oc} \equiv \frac{4\pi\hbar^2\varepsilon_o\varepsilon_s}{e^2 m_{cj\parallel}}, \quad a_{ov} \equiv \frac{4\pi\hbar^2\varepsilon_o\varepsilon_s}{e^2 m_{vj\parallel}}, \tag{3.24}$$

$$E_{Rc} \equiv \frac{\hbar^2}{2m_{cj\parallel}a_{oc}^2}, \quad E_{Rv} \equiv \frac{\hbar^2}{2m_{vj\parallel}a_{ov}^2}. \tag{3.25}$$

These parameters a_{oc}, a_{ov}, E_{Rc} and E_{Rv} don't have any physical meaning except for the convenience of mathematical manipulation. Similar to Eq. (3.16), we obtain

$$a_{oc}E_{Rc} = a_{ov}E_{Rv} = \frac{e^2}{8\pi\varepsilon_o\varepsilon_b} = a_oE_R \tag{3.26}$$

Using Eq. (3.26) in Eq. (3.24) to solve for the effective masses, we have

$$\frac{1}{m_{cj\parallel}} = \frac{2}{\hbar^2}(a_oE_R)\,a_{oc}, \quad \frac{1}{m_{vj\parallel}} = \frac{2}{\hbar^2}(a_oE_R)\,a_{ov}. \tag{3.27}$$

For the terms containing ω_{pl}^2 in both square brackets of Eq. (3.23), we use Eq. (3.20) for ω_{pl}^2 and Eq. (3.27) for $m_{cj\parallel}$ and $m_{vj\parallel}$ to obtain

$$\begin{aligned}\frac{1}{\omega_{pl}^2}\left(\frac{\hbar q_\parallel^2}{2m_{rj\parallel}}\right)^2 &= \frac{1}{4\pi a_oE_Rq_\parallel\sum\limits_j\left(\frac{n_j}{m_{cj\parallel}}+\frac{p_j}{m_{vj\parallel}}\right)}\left(\frac{\hbar q_\parallel^2}{2m_{rj\parallel}}\right)^2 \\ &= \frac{q_\parallel^3a_o^2}{8\pi\sum\limits_j(n_ja_{oc}+p_ja_{ov})}\end{aligned} \tag{3.28}$$

We have generalized the expression of Eq. (3.28) for a multi-subband QW system. But for a single-subband QW system in both the CB and VB, which is an assumption always made in [Cho94, Hau90], we have $n_j = p_j = n_{2D}$ and therefore the summation over j can be simplified as

$$\begin{aligned}\sum_j (n_j a_{oc} + p_j a_{ov}) &= n_{2D}(a_{oc} + a_{ov}) \\ &= n_{2D} a_o\end{aligned}, \tag{3.29}$$

where it can be shown that

$$\begin{aligned}a_{oc} + a_{ov} &= \frac{4\pi\hbar^2\varepsilon_o\varepsilon_s}{e^2}\left(\frac{1}{m_{cj\|}} + \frac{1}{m_{vj\|}}\right) \\ &= \frac{4\pi\hbar^2\varepsilon_o\varepsilon_s}{e^2}\frac{1}{m_{rj\|}} \\ &= a_o\end{aligned}. \tag{3.30}$$

Finally with the use of Eq. (3.29), Eq. (3.28) reduces to

$$\frac{1}{\omega_{pl}^2}\left(\frac{\hbar q_\|^2}{2m_{rj\|}}\right)^2 = \frac{q_\|^3 a_o}{8\pi n_{2D}}. \tag{3.31}$$

For a multi-subband QW system, which is the real case of the two QW laser systems discussed in Chapter 2, it can be shown that Eq. (3.31) still gives a close numerical result to that Eq. (3.28) gives. To simplify the calculation, Eq. (3.31) will be used hereinafter for the multi-subband system as well. Plugging Eq. (3.31) into Eq. (3.23), we have

$$1 - \frac{\omega_{pl}^2}{\omega_{q_\|}^2} = \left[\frac{q_\|}{\lambda_s} + \frac{a_o q_\|{}^3}{8\pi n_{2D}}\right]\left[1 + \frac{q_\|}{\lambda_s} + \frac{a_o q_\|{}^3}{8\pi n_{2D}}\right]^{-1}. \tag{3.32}$$

Finally, using Eq. (3.32) in Eq. (3.19) for $\varepsilon_\|$ and then plugging $\varepsilon_\|$ into Eq. (3.18), the screened Coulomb potential can be expressed as

$$V_{sq_\|} = \frac{4\pi a_o E_R}{q_\| A}\left[\frac{q_\|}{\lambda_s} + \frac{a_o q_\|{}^3}{8\pi n_{2D}}\right]\left[1 + \frac{q_\|}{\lambda_s} + \frac{a_o q_\|{}^3}{8\pi n_{2D}}\right]^{-1}. \tag{3.33}$$

With this expression for $V_{q_\|}$, we can discuss the effects of bandgap renormalization due to plasma screening next.

3.3.2 Bandgap Renormalization

As carrier density increases, more unoccupied states become available to the VB electrons. As a consequence, the VB electron distribution can change in such a way that the Coulomb repulsion with the CB electrons is more effectively screened. This slight rearrangement of the charge carriers results in decreases in the single-particle energies and, as a consequence, a reduction in bandgap. In this case, the total bandgap renormalization (BGR) ΔE_{BGR} is the sum of Coulomb-hole (CH) self-energy ΔE_{CH} and screened-exchange (SX) self-energy ΔE_{SX}. The first contribution ΔE_{CH} describes the energy reduction of electrons (holes) with different spin by avoiding each other because of the mutual Coulomb repulsion and is the difference between screened and unscreened Coulomb potential [Cho94, Hau90],

$$\Delta E_{CH} = \sum_{\mathbf{q}_{\parallel}} (V_{sq_{\parallel}} - V_{q_{\parallel}}) \, . \tag{3.34}$$

Using Eqs. (3.17) and (3.33), we obtain

$$V_{sq_{\parallel}} - V_{q_{\parallel}} = -\frac{4\pi a_o E_R}{q_{\parallel} A}\left[1 + \frac{q_{\parallel}}{\lambda_s} + \frac{a_o q_{\parallel}{}^3}{8\pi n_{2D}}\right]^{-1} . \tag{3.35}$$

Eq. (3.34) can be then rewritten as

$$\Delta E_{CH} = -\sum_{\mathbf{q}_{\parallel}} \frac{4\pi a_o E_R}{q_{\parallel} A}\left[1 + \frac{q_{\parallel}}{\lambda_s} + \frac{a_o q_{\parallel}{}^3}{8\pi n_{2D}}\right]^{-1} . \tag{3.36}$$

To evaluate the summation over $\mathbf{q}_{\parallel}$, we first must be able to count the available $\mathbf{q}_{\parallel}$ states. For a QW, within the plane of QW, a 2D vector $\mathbf{q}_{\parallel}$ sweeps out a circle of radius $q_{\parallel}$ in $q_{\parallel}$ space, as shown in Fig. 3.3. One $\mathbf{q}_{\parallel}$ state occupies a square of area in $q_{\parallel}$ space equal to $4\pi^2/A$, which is just like that a $\mathbf{k}_{\parallel}$ state takes up a square area of $4\pi^2/A$ in $k_{\parallel}$ space [Cor93]. Therefore, number of $\mathbf{q}_{\parallel}$ states within the area defined by increments in $q_{\parallel}$ and

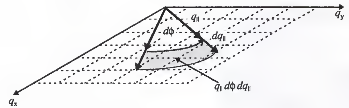

Figure 3.3 Distribution of $\mathbf{q}_\parallel$ vector states in $q_\parallel$ space for a QW. One $\mathbf{q}_\parallel$ state takes up a square area of $4\pi^2/A$ indicated by a mesh of dashed lines. The shaded area of $q_\parallel d\phi dq_\parallel$ represents the infinitesimal area defined by an increment of $dq_\parallel$ in the magnitude of $\mathbf{q}_\parallel$ and an increment of $d\phi$ in its sweep angle ϕ. The number N_s of $\mathbf{q}_\parallel$ states within this shaded area is just the number of the squares within it. Every $\mathbf{q}_\parallel$ state can be taken into account by an integration of N_s over the whole $q_\parallel$ space.

sweep angle ϕ (shown as the shaded area in Fig. 3.3) can be written as

$$N_s = \frac{q_\parallel d\phi dq_\parallel}{\frac{4\pi^2}{A}}, \tag{3.37}$$

where the spin degeneracy is not included. The summation over $\mathbf{q}_\parallel$ can be replaced by an integration of N_s over the whole $q_\parallel$ space

$$\sum_{\mathbf{q}_\parallel} \rightarrow \int_0^\infty \int_0^{2\pi} \frac{q_\parallel d\phi dq_\parallel}{\frac{4\pi^2}{A}}. \tag{3.38}$$

Since the function to be summed in Eq. (3.36) is independent of ϕ, its integration over ϕ is equal to 2π and Eq. (3.36) becomes

$$\Delta E_{CH} = -2a_o E_R \int_0^\infty \left[1 + \frac{q_\parallel}{\lambda_s} + \frac{a_o q_\parallel^3}{8\pi n_{2D}}\right]^{-1} dq_\parallel. \tag{3.39}$$

To perform the integration in Eq. (3.39), we evaluate the integrand at two extreme cases:

$$\left[1 + \frac{q_\parallel}{\lambda_s} + \frac{a_o q_\parallel^3}{8\pi n_{2D}}\right]^{-1} \cong \begin{cases} \left[1 + \frac{q_\parallel}{\lambda_s}\right]^{-1} & \text{for } q_\parallel \ll \sqrt{\frac{8\pi n_{2D}}{\lambda_s a_o}} \\ 0 & \text{for } q_\parallel \gg \sqrt{\frac{8\pi n_{2D}}{\lambda_s a_o}} \end{cases}. \tag{3.40}$$

Using the evaluation in Eq. (3.40), Eq. (3.39) can be approximated as

$$\begin{aligned} \Delta E_{CH} &\cong -2a_o E_R \int_0^{\sqrt{\frac{8\pi n_{2D}}{a_o \lambda_s}}} \left[1 + \frac{q_\parallel}{\lambda_s}\right]^{-1} dq_\parallel \\ &= -2a_o E_R \lambda_s \ln\left[1 + \sqrt{\frac{8\pi n_{2D}}{\lambda_s^3 a_o}}\right] \end{aligned}. \tag{3.41}$$

The second contribution ΔE_{SX} results from the change in electron (hole) self-energies due to the fact that electrons (holes) with equal spin avoid each other (Pauli exclusion principle) and is given by [Cho94, Hau90]

$$\Delta E_{SX} = -\sum_{q_\parallel} V_{sq_\parallel}(f_{cq_\parallel} + f_{hq_\parallel}). \tag{3.42}$$

We substitute Eq. (3.33) for the screened Coulomb potential $V_{sq_\parallel}$ and Eq. (3.38) for the summation over $\mathbf{q}_\parallel$ in Eq. (3.42) to obtain

$$\begin{aligned}\Delta E_{SX} &= -2a_o E_R \int_0^\infty dq_\parallel \left[\frac{q_\parallel}{\lambda_s} + \frac{a_o q_\parallel{}^3}{8\pi n_{2D}}\right]\left[1 + \frac{q_\parallel}{\lambda_s} + \frac{a_o q_\parallel{}^3}{8\pi n_{2D}}\right]^{-1} (f_{cq_\parallel} + f_{hq_\parallel}) \\ &= -\frac{2a_o E_R}{\lambda_s}\int_0^\infty q_\parallel dq_\parallel \left[1 + \frac{\lambda_s a_o q_\parallel{}^2}{8\pi n_{2D}}\right]\left[1 + \frac{q_\parallel}{\lambda_s} + \frac{a_o q_\parallel{}^3}{8\pi n_{2D}}\right]^{-1} (f_{cq_\parallel} + f_{hq_\parallel})\end{aligned}, \tag{3.43}$$

where a factor of $q_\parallel/\lambda_s$ is pulled out of the first bracket in last form of ΔE_{SX}. Often, the weak-momentum dependence of ΔE_{SX} is neglected and at the subband edge $q_\parallel = k'_\parallel$ with $k_\parallel = 0$ in Eq. (3.13), then we have

$$\begin{aligned}\Delta E_{SX} = &-\frac{2a_o E_R}{\lambda_s}\int_0^\infty k'_\parallel dk'_\parallel \left[1 + \frac{\lambda_s a_o k'_\parallel{}^2}{8\pi n_{2D}}\right]\left[1 + \frac{k'_\parallel}{\lambda_s} + \frac{a_o k'_\parallel{}^3}{8\pi n_{2D}}\right]^{-1} \\ &\times [f_c(E_{cj\mathbf{k}'_\parallel}) + f_h(E_{vj\mathbf{k}'_\parallel})]\end{aligned}. \tag{3.44}$$

3.3.3 Simulation Results

InGaAs QW. Plots of ΔE_{CH}, ΔE_{SX} and ΔE_{BGR} as a function of volume carrier density N for C1-HH1 and C1-LH1 transitions are shown as the dash-dotted, dashed and solid lines in Fig. 3.4, respectively. Often, if the weak momentum dependence of BGR is neglected, BGR can be taken into account by rigidly shifting the gain and spontaneous emission by an amount of ΔE_{BGR}, where the negative sign on the values of ΔE_{BGR} means a red shift of spectra to lower photon energy. The corresponding BGR-shifted TE gain and spontaneous emission spectra of Figs. 3.1(a) and (b) are shown in Figs. 3.5(a) and (b). As discussed later in Chapter 4, the red shift in gain spectra gives an opposite direction in predicting the dependence of lasing wavelength on cavity length.

CdZnSe QW. Plots of ΔE_{CH}, ΔE_{SX} and ΔE_{BGR} as a function of N for C1-HH1 and C1-LH1 transitions are shown as the dash-dotted, dashed and solid lines in Fig. 3.6, respectively. The corresponding BGR-shifted spectra of Figs. 3.2(a) and (b) are shown in Fig. 3.7(a) and (b) where the resulting peak gain location is well below $E_{g1,hh}$ by about 55 meV. This situation, which will be discussed later in Chapter 5, was often mistakenly elucidated as the evidence for existence of excitonic gain in CdZnSe QW lasers even at room temperature [Ding94].

Comparison. By comparing Fig. 3.4 with Fig. 3.6, we find that ΔE_{BGR} vs. N curves are about the same for the InGaAs QW and CdZnSe QW, although their ΔE_{CH} and ΔE_{SX} components are different. This could be an coincidence, however, it agrees with an universal formula commonly used for ΔE_{BGR} that goes with one-third power of N [Chi88, Col95].

3.4 Coulomb Enhancement (CE)

3.4.1 Coulomb Enhancement Factor

The Coulomb attraction between electrons in the CB and holes in the VB tends to keep electrons and holes within the vicinity of each other. This increases the radiative recombination rate and results in an enhancement in optical gain as well as spontaneous emission rate. To investigate the effects of Coulomb enhancement on optical gain $g(\hbar\omega)$ and spontaneous emission $R_{sp}(\hbar\omega)$, we start with the complex optical susceptibility $\tilde{\chi}(\hbar\omega)$, since both $g(\hbar\omega)$ and $R_{sp}(\hbar\omega)$ are related to $\tilde{\chi}(\hbar\omega)$. In a multi-subband system, the total optical susceptibility $\tilde{\chi}(\hbar\omega)$ is the summation over the contributions $\tilde{\chi}_j(\hbar\omega)$ from the allowed subband transition pairs and is expressed as

$$\tilde{\chi}(\hbar\omega) = \sum_j \tilde{\chi}_j(\hbar\omega) , \tag{3.45}$$

where the subscript j indicates the jth subband transition pair. With inclusion of Coulomb enhancement, $\tilde{\chi}_j(\hbar\omega)$ is given by (in C.G.S. units) [Cho94, Hau90]

$$\tilde{\chi}_j(\hbar\omega) = \frac{4\pi}{\varepsilon_\infty V} \sum_k \frac{d_{cv}\chi_k^o}{1 - q_{1k}} , \tag{3.46}$$

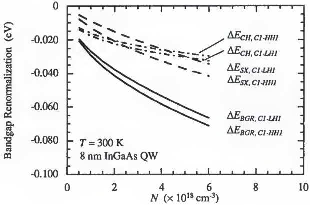

Figure 3.4 Bandgap renormalization as a function of carrier density N for C1-HH1 and C1-LH1 subband transitions in the 8 nm $In_{0.15}Ga_{0.85}As$/GaAs QW at $T = 300$ K. The solid curves are the total bandgap renormalization (BGR), the dash-dotted curves are the Coulomb-hole components (CH) and the dashed curves are the screen-exchange (SX) components.

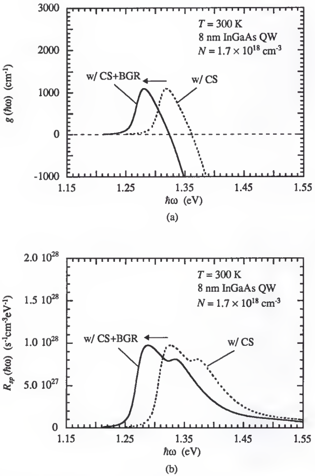

Figure 3.5 The rigidly shifted (a) TE gain and (b) spontaneous emission spectra (solid curves) for the 8 nm $In_{0.15}Ga_{0.85}As/GaAs$ QW at $N = 1.7 \times 10^{18}$ cm^{-3} and T = 300 K by the bandgap renormalization due to plasma screening. The dashed curves are the spectra without BGR shifts.

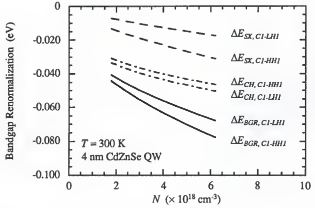

Figure 3.6 Bandgap renormalization as a function of carrier density N for C1-HH1 and C1-LH1 subband transitions in the 4 nm $Cd_{0.3}Zn_{0.7}Se/ZnS_{0.06}Se_{0.94}$ QW at T = 300 K. The solid curves are the total bandgap renormalization (BGR), the dash-dotted curves are the Coulomb-hole components (CH) and the dashed curves are the screen-exchange (SX) components.

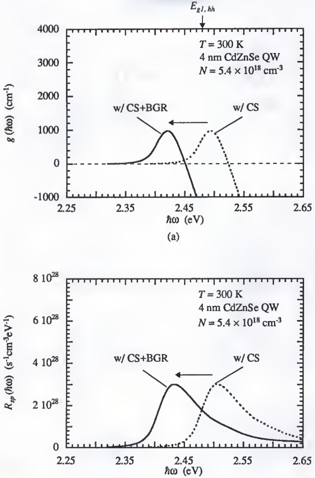

(a)

(b)

Figure 3.7 The rigidly shifted (a) TE gain and (b) spontaneous emission spectra (solid curves) for the 4 nm $Cd_{0.3}Zn_{0.7}Se/ZnS_{0.06}Se_{0.94}$ QW at $N = 5.4 \times 10^{18}$ cm^{-3} and $T = 300$ K by the bandgap renormalization due to plasma screening. The dashed curves are the spectra without BGR shifts.

with

$$\begin{aligned}\chi_k^o &= -d_{cv}\frac{(1-f_{ek}-f_{hk})}{\hbar(\omega+i\delta-e_{ek}-e_{hk})}\\ &= -id_{cv}\frac{(f_{ek}+f_{hk}-1)}{\hbar\delta+i(e_{ek}+e_{hk}-\hbar\omega)}\end{aligned} \tag{3.47}$$

and

$$q_{1k} = \frac{1}{d_{cv}}\sum_{k'}\bar{V}_{s,k,k'}\chi_{k'}^o, \tag{3.48}$$

where V is the volume of QW, $\varepsilon_\infty = \bar{n}^2$ is the background dielectric constant of QW, d_{cv} is the square root of the dipole moment matrix element at transition involving in-plane wavevector $\mathbf{k}_{\|}$, $1/(1 - q_{1k})$ is the Coulomb enhancement factor in Padé approximation, $\bar{V}_{s,k,k'}$ is the screened Coulomb potential, f_{ek} and f_{hk} are the Fermi-Dirac distributions of electrons and holes with energies e_{ek} and e_{hk} in the CB and VB respectively and $\hbar\delta$ is the dephasing or broadening factor due to carrier scattering. Originally, Eqs. (3.45) to (3.47) are derived under the assumption of a single-subband system and solved from the Bethe-Salpeter equation for the only one existing subband transition pair [Cho94, Hau90]. Since in a multi-subband system a set of Bethe-Salpeter equations for various allowed subband transition pairs can be solved independently for each allowed subband transition pair as long as the screening effect is considered with inclusion of all the subbands (as we have done in Section 3.3.1) [Cam94], we are allowed to generalize Eqs. (3.46) to (3.48) to be used in Eq. (3.37) of a multi-subband system.

Now we want to expand Eqs. (3.47) and (3.48) in terms of the parameters that we are familiar with. We begin with the dipole moment matrix element. The relationship between the transition matrix element and the dipole moment matrix element in M.K.S. units is given by [Col95]

$$e^2|M_T|^2 = 2m_o^2\omega^2e^2|x|^2, \tag{3.49}$$

where $e^2|x|^2$ is the dipole moment matrix element and x is the position operator. The factor of 2 in the front counts for the spin degeneracy buried in $|M_T|^2$ and is not included in the reduced density of states ρ_{red} given in Eq. (2.33). On the contrary, in [Col95] the spin degeneracy is taken into account in ρ_{red} instead of $|M_T|^2$. From Eq. (3.49), we can relate the dipole moment matrix element d_{cv}^2 in C.G.S. units to $|M_T|^2$ in M.K.S. units as follows

$$d_{cv}^2 = \frac{e^2|x|^2}{4\pi\varepsilon_o} = \frac{e\,|M_T|^2}{8\pi\varepsilon_o m_o^2\omega^2}, \tag{3.50}$$

where the factor of $1/(4\pi\varepsilon_o)$ is the converting constant between C.G.S. and M.K.S. units. By the following substitutions in Eqs. (3.47) and (3.48)

$$\begin{aligned}
& k \rightarrow k_{\|}, \quad k' \rightarrow k_{\|}' \\
& d_{cv} \rightarrow \frac{e|M_T|}{\sqrt{8\pi\varepsilon_o}m_o\omega}, \quad d_{cv}' \rightarrow \frac{e|M_T'|}{\sqrt{8\pi\varepsilon_o}m_o\omega} \\
& f_{ek} \rightarrow f_c(E_{cj\mathbf{k}_{\|}}), \quad f_{hk} \rightarrow f_h(E_{cj\mathbf{k}_{\|}}) \\
& \bar{V}_{s,k,k'} \rightarrow V_{sq_{\|}} \\
& \hbar\delta \rightarrow \Gamma_{cv}(\hbar\omega, E_{cv}) \\
& e_{ek} + e_{hk} \rightarrow E_{cv}
\end{aligned} \tag{3.51}$$

we obtain

$$\chi_{k_{\|}}^{o} = -i\frac{e|M_T|}{\sqrt{8\pi\varepsilon_o}m_o\omega}\frac{[f_c(E_{cj\mathbf{k}_{\|}}) + f_h(E_{vj\mathbf{k}_{\|}}) - 1]}{\Gamma_{cv}(\hbar\omega, E_{cv}) + i(E_{cv} - \hbar\omega)} \tag{3.52}$$

and

$$\begin{aligned}
q_{1j}(\hbar\omega, E_{cv}) = {} & \frac{\sqrt{8\pi\varepsilon_o}m_o\omega}{e|M_T|}\sum_{\mathbf{k}_{\|}'}\frac{4\pi a_o E_R}{\lambda_s A}\left[1 + \frac{\lambda_s a_o q_{\|}^2}{8\pi n_{2D}}\right]\left[1 + \frac{q_{\|}}{\lambda_s} + \frac{a_o q_{\|}^3}{8\pi n_{2D}}\right]^{-1} \\
& \times\left\{-i\frac{e|M_T'|}{\sqrt{8\pi\varepsilon_o}m_o\omega}\frac{[f_c(E_{cj\mathbf{k}_{\|}'}) + f_h(E_{vj\mathbf{k}_{\|}'}) - 1]}{\Gamma_{cv}(\hbar\omega, E_{cv}') + i(E_{cv}' - \hbar\omega)}\right\}
\end{aligned}, \tag{3.53}$$

where Eq. (3.33) is used for $V_{sq_{\|}}$. The superscript $'$ indicates the parameters involving transition energy E_{cv}' and the associated wavevector $\mathbf{k}_{\|}'$. We also use the $\hbar\omega$ dependent broadening factor Γ_{cv} defined in Eq. (3.6) in the CE expression above instead of the $\hbar\omega$

independent broadening factor $\hbar\delta$ usually used in previous literatures discussing many-body effects [Cho94, Hau90]. Similar to Eq. (3.38), we replace the summation over $\mathbf{k}_{\parallel}'$ in Eq. (3.53) with

$$\sum_{\mathbf{k}_{\parallel}'} \rightarrow \frac{A}{4\pi^2}\int_0^{\infty}\int_0^{2\pi} k_{\parallel}' d\theta dk_{\parallel}' \tag{3.54}$$

to obtain

$$\begin{aligned} q_{1j}(\hbar\omega, E_{cv}) &= -i\frac{a_o E_R}{\pi\lambda_s|M_T|} \\ &\quad \times \int_0^{\infty} k_{\parallel}' dk_{\parallel}' |M_T'| \frac{[f_c(E_{cj\mathbf{k}_{\parallel}'}) + f_h(E_{vj\mathbf{k}_{\parallel}'}) - 1]}{\Gamma(\hbar\omega, E_{cv}') + i(E_{cv}' - \hbar\omega)} \Theta(\mathbf{k}_{\parallel}, \mathbf{k}_{\parallel}') \end{aligned} , \tag{3.55}$$

where

$$\Theta(\mathbf{k}_{\parallel}, \mathbf{k}_{\parallel}') = \int_0^{2\pi}\left[1 + \frac{\lambda_s a_o q_{\parallel}^2}{8\pi n_{2D}}\right]\left[1 + \frac{q_{\parallel}}{\lambda_s} + \frac{a_o q_{\parallel}^3}{8\pi n_{2D}}\right]^{-1} d\theta . \tag{3.56}$$

Since $q_{\parallel}$ is θ dependent as defined in Eq. (3.13), the integrand can not be pulled out of integration over θ. So far, we have successfully derived the Coulomb enhancement factor to be in a form such that we can use. Next, we will show how it can corporate into the optical gain and spontaneous emission functions.

3.4.2 Gain and Spontaneous Emission Functions

The optical gain $g(\hbar\omega)$ is related to the complex optical susceptibility $\tilde{\chi}(\hbar\omega)$ by [Cho94, Hau90]

$$\begin{aligned} g(\hbar\omega) &= -\frac{\omega\bar{n}}{c} Imag[\tilde{\chi}(\hbar\omega)] \\ &= \frac{\omega\bar{n}}{c} Real[i\tilde{\chi}(\hbar\omega)] \end{aligned} , \tag{3.57}$$

where the notations *Imag* and *Real* refer to the imaginary and real parts of a complex parameter, respectively. Plugging Eq. (3.47) into Eq. (3.46) for $\tilde{\chi}_j(\hbar\omega)$, we can rewrite Eq.

(4.45) as

$$\tilde{\chi}(\hbar\omega) = -i\sum_j\left[\frac{4\pi}{\varepsilon_\infty V}\sum_k\frac{d_{cv}^2}{1-q_{1k}}\frac{(f_{ek}+f_{hk}-1)}{\hbar\delta+i(e_{ek}+e_{hk}-\hbar\omega)}\right]. \tag{3.58}$$

Applying Eq. (3.58) to Eq. (3.57) and substituting ε_∞ with $\bar{n}^2$, we have

$$g(\hbar\omega) = \sum_j Real\left[\frac{1}{V}\sum_k\frac{d_{cv}^2}{1-q_{1k}}\frac{4\pi\omega}{\bar{n}c}\frac{(f_{ek}+f_{hk}-1)}{\hbar\delta+i(e_{ek}+e_{hk}-\hbar\omega)}\right]. \tag{3.59}$$

The summation over k can be replaced by

$$\frac{1}{V}\sum_k \to \int_{E_{gj}}^{\infty}2\rho_{red}\,dE_{cv} \tag{3.60}$$

where the lower limit of the integral is chosen to be E_{gj} because ρ_{red} is zero for $E_{cv} < E_{gj}$ for a given transition pair. Using the substitutions in Eqs. (3.51) and (3.60), Eq. (3.59) becomes

$$\begin{aligned} g(\hbar\omega) = Real\Bigg\{\sum_j\int_{E_{gj}}^{\infty}\left(\frac{1}{\hbar\omega}\right)\frac{\pi e^2\hbar}{\varepsilon_o c m_o^2\bar{n}}\rho_{red}\frac{[f_c(E_{cjk_\parallel})+f_h(E_{vjk_\parallel})-1]}{1-q_{1j}(\hbar\omega,E_{cv})} \\ \times\frac{1}{\pi}\frac{1}{\Gamma_{cv}(\hbar\omega,E_{cv})+i(E_{cv}-\hbar\omega)}dE_{cv}\Bigg\} \end{aligned}. \tag{3.61}$$

It can be shown that

$$\frac{1}{\pi}\frac{1}{\Gamma_{cv}(\hbar\omega,E_{cv})+i(E_{cv}-\hbar\omega)} = L_j(\hbar\omega-E_{cv})\left[1-i\frac{(E_{cv}-\hbar\omega)}{\Gamma_{cv}(\hbar\omega,E_{cv})}\right], \tag{3.62}$$

where $L_j(\hbar\omega - E_{cv})$ is defined in Eq. (3.5). Using Eqs. (2.25) and (3.62) in Eq. (3.61), finally the optical gain with Coulomb enhancement can be expressed as

$$\begin{aligned} g_E(\hbar\omega) = Real\Bigg\{\sum_j\int_{E_{gj}}^{\infty}\frac{g_j(E_{cv})}{1-q_{1j}(\hbar\omega,E_{cv})} \\ \times L_j(\hbar\omega-E_{cv})\left[1-i\frac{(E_{cv}-\hbar\omega)}{\Gamma_{cv}(\hbar\omega,E_{cv})}\right]dE_{cv}\Bigg\} \end{aligned}, \tag{3.63}$$

where the E subscript indicates the Coulomb enhanced gain. If q_{1j} is zero, the optical gain function with CE, $g_E(\hbar\omega)$, in Eq. (3.62) will reduce to its counterpart without CE, $g_B(\hbar\omega)$, in Eq. (3.1).

Recalling Eq. (3.58), $\tilde{\chi}(\hbar\omega)$ contains the factor associated with the Fermi-Dirac distributions which can be subdivided into two components as

$$(f_{ek}+f_{hk}-1) = [f_{ek}f_{hk}] - [(1-f_{ek})(1-f_{hk})]. \tag{3.64}$$

The first square bracket is referred as the emission component, since it is the joint probability of finding an occupied state in the CB and an unoccupied state in the VB. The second square bracket is referred as the absorption component, since it is the joint probability of finding an occupied state in the VB and an unoccupied state in the CB. Using this subdivision in Eq. (3.58), $\tilde{\chi}(\hbar\omega)$ can be subdivided into two components as follows

$$\begin{aligned} \tilde{\chi}_{em}(\hbar\omega) &= -i\sum_j\left[\frac{4\pi}{\varepsilon_\infty V}\sum_k\frac{d_{cv}^2}{1-q_{1k}}\frac{(f_{ek}f_{hk})}{\hbar\delta+i(e_{ek}+e_{hk}-\hbar\omega)}\right] \\ \tilde{\chi}_{ab}(\hbar\omega) &= -i\sum_j\left[\frac{4\pi}{\varepsilon_\infty V}\sum_k\frac{d_{cv}^2}{1-q_{1k}}\frac{(1-f_{ek})(1-f_{hk})}{\hbar\delta+i(e_{ek}+e_{hk}-\hbar\omega)}\right] \end{aligned}, \tag{3.65}$$

where $\tilde{\chi}(\hbar\omega) \equiv \tilde{\chi}_{em}(\hbar\omega) - \tilde{\chi}_{ab}(\hbar\omega)$. The subscripts *em* and *ab* indicate emission and absorption, respectively. The spontaneous emission function is related to the imaginary of $\tilde{\chi}_{em}(\hbar\omega)$, which can be seen as an analogy to Eq. (3.57). Similar to the derivation of Eq. (3.63), the Coulomb enhanced spontaneous emission function $R_{spE}(\hbar\omega)$ can be expressed as

$$\begin{aligned} R_{spE}(\hbar\omega) = Real\Bigg\{&\sum_j\int_{E_{gj}}^{\infty}\frac{R_{spj}(E_{cv})}{1-q_{1j}(\hbar\omega,E_{cv})} \\ &\times L_j(\hbar\omega-E_{cv})\left[1-i\frac{(E_{cv}-\hbar\omega)}{\Gamma_{cv}(\hbar\omega,E_{cv})}\right]dE_{cv}\Bigg\} \end{aligned}. \tag{3.66}$$

As we recall, the emission component of Eq. (3.64) appears in the expression for single-particle $R_{spj}(\hbar\omega)$ function given in Eq. (2.26). For the spontaneous emission function, the Coulomb enhancement factor $1/(1 - q_{1j})$ is slightly different from that of the gain function by replacing $|M_T|$ in the denominator and $|M_T'|$ in the numerator in Eq. (3.55) with $|\overline{M}_T|$ and $|\overline{M}_T'|$. As a consequence, $|\overline{M}_T|$ and $|\overline{M}_T'|$ cancel with each other since they are both equal to $\sqrt{2/3}|M|$ as shown in Eq. (2.15). Again, the spontaneous function $R_{spE}(\hbar\omega)$ with CE included in Eq. (3.66) reduces to its counterpart $R_{spB}(\hbar\omega)$ without CE included in Eq.

(3.2) if $q_{1j} = 0$.

3.4.3 Simulation Results

InGaAs QW. Fig. 3.8(a) shows plots of $g_B(\hbar\omega)$ and $g_E(\hbar\omega)$ vs. $\hbar\omega$, with inclusion of the rigid shift due to BGR, for $N = 1.7 \times 10^{18}$ cm^{-3}. In this case, CE increases the peak material gain g by a factor of 1.4 and blue shifts its spectral position E by 4 meV. This blue shift is very important in predicting the slope of cavity length dependence of lasing energy as would be discussed in Chapter 4. Fig. 3.8(b) shows plots of $R_{spB}(\hbar\omega)$ and $R_{spE}(\hbar\omega)$ vs. $\hbar\omega$, with inclusion of the rigid shift due to BGR, for $N = 1.7 \times 10^{18}$ cm^{-3}. The increase in spontaneous emission due to CE is evident and is also important in predicting the threshold current of diode lasers (see Chapter 4).

CdZnSe QW. In Fig. 3.9(a), $g_B(\hbar\omega)$ and $g_E(\hbar\omega)$ vs. $\hbar\omega$, which include the rigid shift due to BGR, are plotted as the dotted and solid curves for $N = 5.4 \times 10^{18}$ cm^{-3}, respectively. It is shown that CE increases g by a factor of 2.35 and blue shifts E by 6 meV. Fig. 3.9(b) shows plots of $R_{spB}(\hbar\omega)$ and $R_{spE}(\hbar\omega)$ vs. $\hbar\omega$, with inclusion of the rigid shift due to BGR, for $N = 5.4 \times 10^{18}$ cm^{-3}.

Comparison. Comparing the TE gain spectra in Figs. 3.8(a) and 3.9(a), it is clear that CE is stronger in the wide bandgap II-VI CdZnSe QW than in the III-V InGaAs QW. A stronger Coulomb attractive effect can be indicated by a larger exciton binding energy ΔE_{ex} in the semiconductors. For a 2D QW structure, ΔE_{ex} is equal to $4E_R$ where E_R is the Rydberg constant defined in Eq. (3.12). By plugging the material parameters listed in Tables 2.1 and 2.2, ΔE_{ex} of the $n = 1$ HH excitons is found to be about 11 meV in an $In_{0.15}Ga_{0.85}As$ QW while it is about 46 meV (about a factor of 4) in a $Cd_{0.3}Zn_{0.7}Se$ QW.

Comment. In Eq. (3.46), the Coulomb enhancement factor is derived in the Padé approximation which is a good approximation for carrier densities above the so-called Mott density N_{Mott}. At the Mott density, the exciton binding energy vanishes and excitons cease

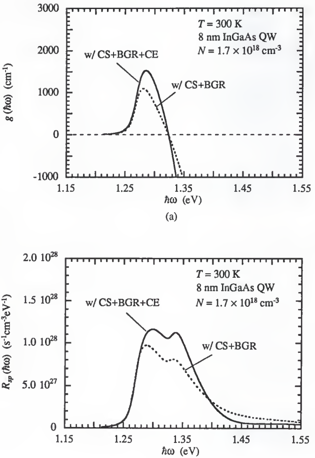

(a)

(b)

Figure 3.8 The inclusion of Coulomb enhancement on (a) TE gain and (b) spontaneous emission spectra (solid curves) for the 8 nm $In_{0.15}Ga_{0.85}As$/GaAs QW at $N = 1.7 \times 10^{18}$ cm^{-3} and $T = 300$ K. The dashed curves are the spectra without CE.

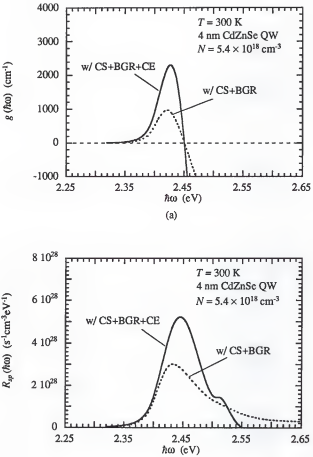

(a)

(b)

Figure 3.9 The inclusion of Coulomb enhancement on (a) TE gain and (b) spontaneous emission spectra (solid curves) for the 4 nm $Cd_{0.3}Zn_{0.7}Se/ZnS_{0.06}Se_{0.94}$ QW at $N = 5.4 \times 10^{18}$ cm^{-3} and T = 300 K. The dashed curves are the spectra without CE.

to exist due to the screening of charged carriers in semiconductors [Hau90, Zim88]. The value for N_{Mott} can be simply found from a plot of ΔE_{BGR} vs. N at which $|\Delta E_{BGR}|$ is equal to ΔE_{ex} [Zim88]. For an 8 nm $In_{0.15}Ga_{0.85}As$ QW, with $\Delta E_{ex} = 11$ meV, we thus find $N_{Mott} << 5 \times 10^{17}$ cm^{-3} from Fig. 3.4. For a 4 nm $Cd_{0.3}Zn_{0.7}Se$ QW, with $\Delta E_{ex} = 46$ meV, N_{Mott} is found to be about 2×10^{18} cm^{-3} (or 8×10^{11} cm^{-2} in sheet density) from Fig. 3.6. Because of this large value for N_{Mott} in II-VI CdZnSe QW, it has always been a suspicion that lasing in CdZnSe QW lasers is excitonic in nature [Ding92, Ding93, Ding94]. In Chapter 4, we will show that even for the CdZnSe QW lasers, the carrier densities required to achieve lasing thresholds at room temperature are higher than the Mott density.

3.5 Summary

In this chapter, we have discussed many-body effects, such as carrier scattering, bandgap renormalization and Coulomb enhancement, on the optical gain and spontaneous emission spectra of the semiconductor quantum wells. We have also demonstrated that CE is in fact stronger in the CdZnSe QW than in the InGaAs QW structures.

In next chapter, we will use these gain and spontaneous emission functions developed in Chapters 2 and 3 to make predictions on laser characteristics at threshold and compare them with experiments using both InGaAs and CdZnSe QW lasers.

CHAPTER 4
LASER THRESHOLD CHARACTERISTICS

4.1 Introduction

In Chapter 2 and 3, models of optical gain and spontaneous emission based on electron-hole plasma (EHP) were described. In the so-called conventional EHP theory, only carrier scattering (CS) and bandgap renormalization (BGR) are taken into account [Asa93,Col95, Cor93] and Coulomb enhancement (CE) is left out mostly due to its involvement with complicated computation. In the case of the wide bandgap lasers, such ignorance of CE can be a mistake since it has been reported that CE should be more important in blue-green CdZnSe and InGaN quantum well (QW) lasers [Cho95a, Cho95b, Ree95a, Ree95b, Ree96] than in infrared InGaAs QW lasers. In fact, the calculations in Chapter 3 have shown that CE has larger effects on the shapes and magnitudes of the optical gain and spontaneous emission spectra for the 4 nm $Cd_{0.3}Zn_{0.7}Se$ QW than for the 8 nm $In_{0.15}Ga_{0.85}As$ QW.

In this chapter, we will investigate effects of CE on the simulation of laser threshold characteristics for both the well-developed narrow-bandgap InGaAs QW lasers and the relatively new wide-bandgap CdZnSe QW lasers. In order to see if the inclusion of CE in the simulation yields improved agreement with experiment, a number of InGaAs/GaAs QW and CdZnSe/ZnSSe QW lasers were fabricated, characterized and compared to predictions.

In Section 4.2, the laser devices characterized are described. Comparisons between experiments and predictions on cavity length dependence of lasing energy and threshold current are discussed in Section 4.3 and 4.4, respectively. Lasing energy dependence on temperature is investigated in Section 4.5 and the work is summarized in Section 4.6.

4.2 Laser Devices

4.2.1 InGaAs QW

The epitaxial layers of the InGaAs/AlGaAs GRIN-SCH single QW diode lasers are described in section 2.2.1. Using standard photolithographic techniques, 100 μm stripes on 500 μm centers were defined on the p^+-GaAs cap layer. The p-side of the wafer was then metalized using Au pulsed electroplating technique. After thinning the n-substrate down to a wafer thickness of about 100 μm, the n-side was also Au-electroplated, as shown in Fig. 4.1. The wafer was cleaved into bars with three cavity lengths (L = 500, 1000 and 1500 μm) and then characterized.

4.2.2 CdZnSe QW

The epitaxial layers of the CdZnSe/ZnSSe SCH single QW diode laser are described in section 2.2.2. Fig. 4.2 shows the 5 μm wide buried-ridge index-guided devices fabricated from this structure where the p-contact metal stack is Pd/Pt/Au annealed at 200°C for 15 minutes in forming gas and the n-contact metal stack is Pd/Ge/Au annealed at 200 °C up to an hour in forming gas [Hab97]. These state-of-the-art CdZnSe QW laser devices were provided by the 3M Company. Laser bars with three cavity lengths (L = 740, 1220 and 2010 μm) were characterized.

4.3 Cavity Length Dependence of Lasing Energy

As discussed in Section 3.4.3, CE has effects on the spectral location and the magni-

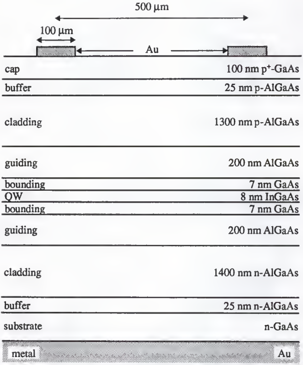

Figure 4.1 Cross-section sketch of the InGaAs/AlGaAs GRIN-SCH single QW diode lasers. Au stripes with widths of 100 μm on 500 μm centers were deposited on the p^+-GaAs cap layer using pulsed electroplating technique. After thinning the n-GaAs substrate down to a wafer thickness of about 100 μm, Au was deposited everywhere on the n-GaAs substrate.

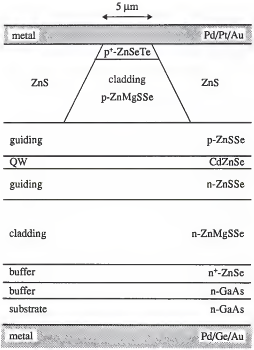

Figure 4.2 Cross-section sketch of the 5 μm wide buried-ridge index-guided CdZnSe/ ZnSSe SCH single QW laser devices provided by the 3M Company. The p-contact metal stack is Pd/Pt/Au annealed at 200°C for 15 minutes in forming gas and the n-contact metal is Pd/Ge/Au annealed at 200°C up to an hour in forming gas [Hab97].

tude of the peak of a gain spectrum. As a consequence, the lasing wavelength λ (or lasing energy *E*) for conventional cleaved facet lasers (Fabry-Perot lasers) should depend on CE, since they lase at the peak of the gain spectra. Due to the fact that an accurate prediction of *E* depends on a precise knowledge of various QW bandgap determining parameters such as QW material composition and degree of biaxial compression, QW thickness, band offsets etc., it is not practical to test the importance of CE by comparing measured and calculated *E* values. However, it can be shown that the dependence of *E* on carrier density *N* is relatively insensitive to the choice of these bandgap-determining parameters but is sensitive to CE. Since this dependence can be determined easily by measuring the dependence of *E* on laser cavity length *L*, it is practical to determine the importance of CE by comparing calculations of the *E* vs. *L* dependence with experiment.

4.3.1 Experiment

InGaAs QW. The arrangement of experimental setup is sketched in Fig. 4.3. The lasers were characterized in the bar form on a Cu probing stage at $T = 300$ K using 2 μsec pulses at 1 kHz repetition rate to avoid heating effect. The laser beam from the laser facet was focused using a spherical lens on to the front slit of the monochromator which in addition has two plane mirrors, a grating and a rear slit, as depicted in Fig. 4.4. The prime mirror brings the laser beam to the grating and the secondary mirror images the diffracted beam from the grating to the rear slit. A silicon PIN-10D photo-detector is placed after the rear slit and plugged into a digital voltmeter to measure the photo voltage. The reading of the voltmeter reaches a maximum once the laser beam is exactly imaged to the rear slit by rotating the grating to a certain angle for a given lasing wavelength λ. Since the angle has been calibrated to the corresponding wavelength by the manufacture of the monochromator, the value of λ is easily read out. At each cavity length *L*, λ was therefore recorded for several lasers and converted to an average emission energy *E* for that *L* value using the following relation

$$E = \frac{hc}{\lambda}, \tag{4.1}$$

where *h* is the Plank constant. The measured dependence of *E* on $1/L$ for the InGaAs QW lasers is plotted in Fig. 4.5. As shown, *E* increases by about 3 meV as *L* decreases from 1500 to 500 μm (i.e. $1/L$ increases from 6.7 to 20 cm^{-1}).

CdZnSe QW. The arrangement of experimental setup is sketched in Fig. 4.6. The lasers were characterized in the bar form on a Cu probing stage at $T = 300$ K using 2 μsec pulses at 1 kHz repetition rate to avoid heating effect. The edge emission spectra from the laser facet were imaged using a microscope objective on to the front slit of the optical multichannel analyzer (OMA). Basically OMA is similar to a monochromator which has an array of 1024 photodetectors (1024 channels) at the rear image plane instead of a rear slit. Photon counts received by each channels are sent to the computer and reconstructed as a spectrum with each channel corresponding to a specific wavelength. Spectra obtained from a typical CdZnSe QW laser, below and just above lasing threshold, are shown in Fig. 4.7. The lasing wavelength λ, defined at the peak of the spectrum just above lasing threshold, was recorded for several lasers at each cavity length *L* and converted to average emission energy *E* for that *L* value using Eq. (3.1). Fig. 4.8 shows the measured dependence of *E* on $1/L$ for CdZnSe QW lasers. In this case, *E* increases by about 6 meV as *L* decreases from 2010 to 740 μm (i.e. $1/L$ increases from 5 to 13.5 cm^{-1}).

4.3.2 Prediction

For typical cleaved-facet lasers (Fabry-Perot lasers) with a cavity length *L*, the frequency spacing Δν between longitudinal modes is given by [Ver89]

$$\Delta\nu = \frac{c}{2nL}, \tag{4.2}$$

where *n* is the refractive index of the cavity. For example, a GaAs laser cavity with $n = 3.6$

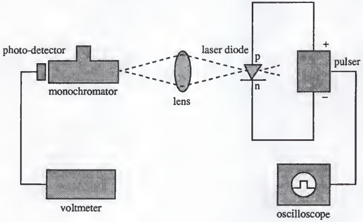

Figure 4.3 Illustration of experimental setup for measuring the lasing wavelength for the InGaAs QW diode lasers. The lasers were tested in a pulsed mode and edge emission from the laser facet was imaged to a monochromator using a spherical lens.

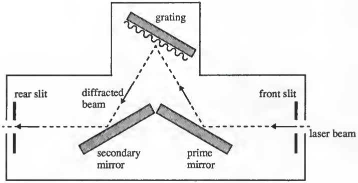

Figure 4.4 Sketch of the components inside the monochromator used in Fig. 4.3. The prime mirror brings the laser beam imaged at the front slit to the grating and the secondary mirror images the diffracted beam to the rear slit by rotating the grating to a proper angle for a given lasing wavelength.

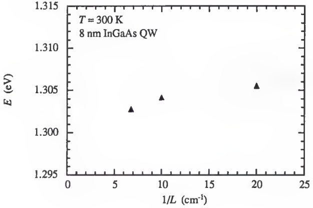

Figure 4.5 Measured lasing energies E of various laser cavity lengths L for the 8 nm $In_{0.15}Ga_{0.85}As$ QW lasers. An increase of about 3 meV in E is found as $1/L$ increases from 6.7 to 20 cm^{-1} (i.e. L decreases from 1500 to 500 μm).

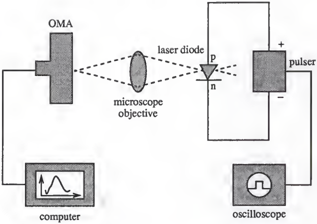

Figure 4.6 Illustration of experimental setup for measuring the edge emission spectra for the CdZnSe QW diode lasers. The lasers were tested in a pulsed mode and edge emission from the laser facet was imaged to an optical multichannel analyzer (OMA) using a microscope objective.

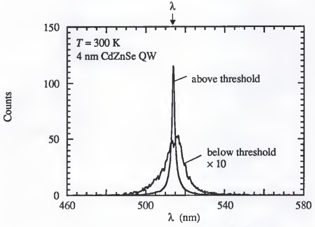

Figure 4.7 Edge emission spectra obtained from a typical 4 nm $Cd_{0.3}Zn_{0.7}Se$ QW diode laser. The spectrum below the threshold, which is magnified 10 times in the plot, is wide. Just above the threshold, the spectrum becomes very narrow and the lasing wavelength λ is defined at the peak of the spectrum.

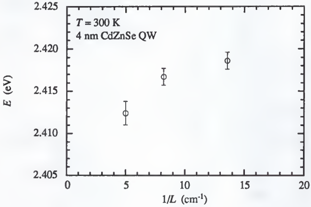

Figure 4.8 Measured lasing energies E of various laser cavity lengths L for the 4 nm $Cd_{0.3}Zn_{0.7}Se$ QW lasers. In this case, E increases by about 6 meV as L decreases from 2010 to 740 μm (i.e. $1/L$ increases from 5 to 13.5 cm^{-1}). The error bars show the variation of E obtained from each laser bar and the open circles are the corresponding average values of E.

and $L = 1000$ μm, $\Delta\nu$ is 42 GHz calculated using Eq. (4.2) which corresponds to an energy spacing $h\Delta\nu$ of 0.17 meV. This spacing is relatively small compared to the spectral width of the gain function $g(\hbar\omega)$ which is typically in the order of 100 meV at threshold. As a consequence, the Fabry-Perot lasers will lase at the peak of $g(\hbar\omega)$ and the lasing energy E is essentially determined by the spectral location of the peak of $g(\hbar\omega)$. The value of E is associated to L by the fact that the magnitude of the peak gain g of $g(\hbar\omega)$ required for lasing at L is given by the expression [Chi88, Col95]

$$g = g_{th} = \frac{1}{\Gamma}\left[\frac{1}{L}\ln\frac{1}{R} + \alpha_i\right], \tag{4.3}$$

where Γ is the transverse mode overlap factor which can be calculated using the software MODEIG, R is the modal reflectivity at the facets and α_i is the mode loss coefficient. The value of α_i can be determined from an experimental plot of the inverse differential quantum efficiency $1/\eta_d$ vs. L [Col95, Hsu96].

The procedures for obtaining E as a function of L, depicted in Fig. 4.9, are summarized as follows: (1) Specify N and T; (2) Calculate and plot the spectral gain function $g(\hbar\omega)$ using Eqs. (2.3) and (2.5) for single-particle model, Eq. (3.1) for the inclusion of CS, Eqs. (3.41) and (3.44) for the addition of BGR, and Eq. (3.63) for the inclusion of CE; (3) Determine the spectral location E of the peak of $g(\hbar\omega)$ and the peak gain g of $g(\hbar\omega)$; (4) Use this value of g in Eq. (4.3) to solve for L; (5) Plot this E vs. $1/L$ pair; (6) Vary N and repeat steps (1) through (5). Finally, a plot of E vs. $1/L$ curve is obtained.

InGaAs QW. For the wide-stripe InGaAs QW lasers used in our experiment, the lateral mode overlap factor is assumed to be unity. Using $\Gamma \cong 0.022$, $R \cong 0.32$ and $\alpha_i = 1.7$ cm^{-1} in Eq. (4.3), the estimated g_{th} are 422, 595, 1113 cm^{-1} for lasers with $L = 1500$, 1000 and 500 μm, respectively. Using the CS-modified gain function $g_B(\hbar\omega)$ given in Eq. (3.1), Fig. 4.10(a) shows the calculated TE gain spectra for $N = 1.2, 1.4, 1.6, 1.8 \times 10^{18}$ cm^{-3} which produce g in the range of interest (~ 300 to 1200 cm^{-1}). The plots indicate that E blue shifts as N increases. Using the procedures described in Fig. 4.9, we translate these plots to an E vs. $1/L$ curve in Fig. 4.10(b). An increase in E (blue shift) of about 5 meV is obtained as L decreases from 1500 to 500 μm (i.e. $1/L$ increases from 6.7 to 20 cm^{-1}). The corresponding change in the experimental data is about 3 meV, a factor of 1.7 smaller. If the BGR shown in Fig. 3.4 is added to the gain spectra of Fig. 4.10(a), the resulting rigidly shifted gain spectra in Fig. 4.11(a) show essentially no shift of peak gain position as N increases. As a consequence, the corresponding E vs. $1/L$ curve in Fig. 4.11(b) shows that the BGR shift essentially cancels the CS shift. It is interesting to note that this CS/BGR cancellation-type effect has been reported previously in the modeling of the dependence of E on L in GaAs SQW lasers [Che93, Chi88]. It is suggested in those works that BGR is overestimated or some other many-body effect needs to be taken into account. We expect that CE may be the answer to this problem. Therefore, we use the CE-modified gain function $g_E(\hbar\omega)$ given Eq. (3.63) to calculate the TE gain spectra for $N = 1.1, 1.2, 1.3, 1.4 \times 10^{18}$ cm^{-3} as shown in Fig. 4.12(a). It clearly shows that E increases with N and the corresponding E vs. $1/L$ curve in Fig. 4.12(b) shows a blue shift in E of about 3 meV as L decreases from 1500 to 500 μm, in good agreement with the experimental shift. Consequently, we conclude from this comparison that CE needs to be included in predicting the dependence of E on L in InGaAs QW lasers. The importance of CE in determining the dependence of operating wavelength on temperature in InGaAs/GaAs vertical-cavity surface-emitting lasers (VCSEL) has been reported previously [Cho95].

CdZnSe QW. For the CdZnSe QW lasers used in our experiment, we have $\Gamma \cong 0.01$, $R \cong 0.243$ and $\alpha_i \cong 10$ cm^{-1}. With these numbers, the estimated g_{th} are 1703, 2159 and 2910 cm^{-1} for $L = 2010$, 1220 and 740 μm, respectively. With inclusion of CS, the calculated TE gain spectra for $N = 6.5, 7.4, 8.3, 9.2 \times 10^{18}$ cm^{-3} produce g in the range of interest (~ 1700 to 3000 cm^{-1}) as shown in Fig. 4.13(a). The corresponding E vs. $1/L$ curve in Fig. 4.13(b) shows an increase in E (blue shift) of about 7 meV as L decreases from 2010 to 740 μm. While this is close to the 6 meV blue shift obtained experimentally (see Fig. 4.8), the predicted values of E are about 85 meV higher than the measured ones. If the BGR shown in

Fig. 3.6 is added to the gain spectra of Fig. 4.13(a), the resulting rigidly shifted gain spectra in Fig. 4.14(a) show a red shift of peak gain position as N increases. As a consequence, Fig. 4.14(b) shows a red shift of the predicted E with decreasing L, opposite to the observed blue shift. With inclusion of CE, the TE gain spectra for $N = 5.0, 5.4, 5.7, 6.0 \times 10^{18}$ cm^{-3} in Fig. 4.15(a) show that E increase with N. As shown in Fig. 4.15(b), one obtains a blue shift in E of about 4 meV as L decreases from 2010 to 740 µm, in good agreement with the experimental shift. It also shows that the predicted absolute values of E are close to the measured values, differing only by about 10 meV. Consequently, we conclude from this comparison that CE needs to be included in predicting the dependence of E on L in CdZnSe QW lasers.

Comment #1. With respect to the discrepancy between the measured absolute value of E and the prediction with CE included, we believe that this is due to a lack of precise knowledge of various QW bandgap determining parameters as stated in the beginning of this section. Since the dependence of E on L is relatively insensitive to the choices of these parameters, we believe that the above conclusions about the importance of CE in both the InGaAs and CdZnSe QW lasers is justified.

Comment #2. In Section 3.5, we discussed a little bit on the definition of Mott density N_{mott} where bound excitons cease to exist and the Padé approximation for CE factor works better. For the 8 nm $In_{0.15}Ga_{0.85}As$ QW lasers, N_{mott} is much less than 5×10^{17} cm^{-3} and for the 4 nm $Cd_{0.3}Zn_{0.7}Se$ QW lasers, it is about 2×10^{18} cm^{-3}. As we have just shown in Figs. 4.12 and 4.15, the carrier densities required to achieve lasing action in the InGaAs and CdZnSe QW lasers are in the order of 1×10^{18} cm^{-3} and 5×10^{18} cm^{-3}, respectively, which are higher than the their associated N_{mott} values. This rules out the possibility of excitonic gain at room temperature even in CdZnSe QW lasers for which excitons were said to be responsible for providing material gain [Ding94]. In Chapter 5, we will show more evidences that electron-hole plasma, not excitons, is the source for gain/absorption in the CdZnSe QW lasers by comparing the theoretical calculations using model with CE taken into account to the experiments.

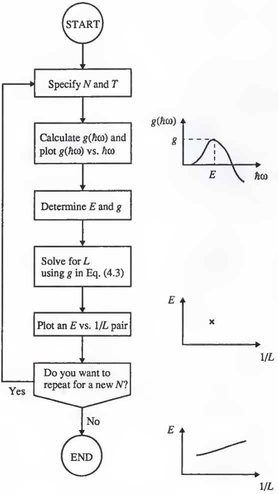
START
Specify N and T
Calculate $g(\hbar\omega)$ and plot $g(\hbar\omega)$ vs. $\hbar\omega$
Determine E and g
Solve for L using g in Eq. (4.3)
Plot an E vs. $1/L$ pair
Do you want to repeat for a new N?
Yes
No
END
$g(\hbar\omega)$
g
E
$\hbar\omega$
E
×
$1/L$
E
$1/L$

Figure 4.9 Flow chart of the procedures for obtaining a theoretical E vs. $1/L$ curve.

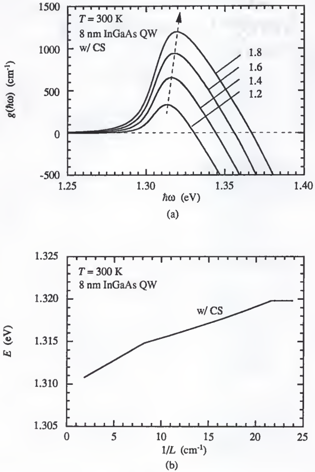

Figure 4.10 With CS included, (a) the calculated TE gain spectra for the 8 nm $In_{0.15}Ga_{0.85}As$ QW lasers at various N ($\times 10^{18}$ cm^{-3}) indicated by the numbers. The arrow indicates that E increases with N; and (b) the corresponding E vs. $1/L$ curve. An increase in E (blue shift) of about 5 meV is obtained as $1/L$ increases from 6.7 to 20 cm^{-1} (i.e. L decreases from 1500 to 500 μm).

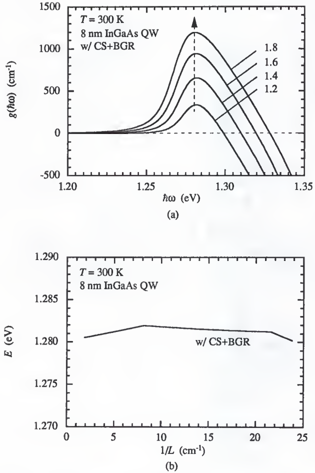

Figure 4.11 With CS and BGR included, (a) the calculated TE gain spectra for the 8 nm $In_{0.15}Ga_{0.85}As$ QW lasers at various N (× 10^{18} cm^{-3}) indicated by the numbers. The arrow indicates essential no shift in E with N; and (b) the corresponding E vs. $1/L$ curve. BGR shift essentially cancels the CS shift.

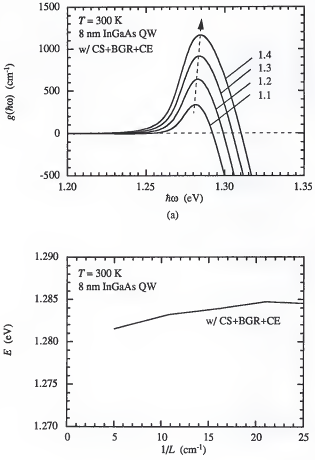

(a)

(b)

Figure 4.12 With CS, BGR and CE included, (a) the calculated TE gain spectra for the 8 nm $In_{0.15}Ga_{0.85}As$ QW lasers at various N (× 10^{18} cm^{-3}) indicated by the numbers. The arrow indicates that E increases with N; and (b) the corresponding E vs. $1/L$ curve. A blue shift in E of about 3 meV is obtained as $1/L$ increases from 6.7 to 20 cm^{-1} (i.e. L decreases from 1500 to 500 μm).

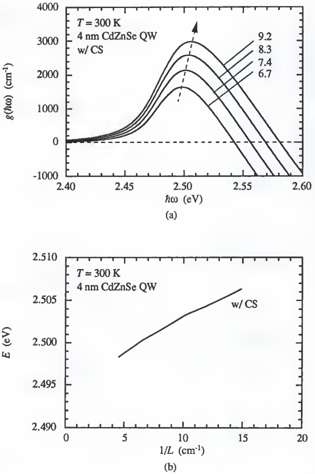

Figure 4.13 With CS included, (a) the calculated TE gain spectra for the 4 nm $Cd_{0.3}Zn_{0.7}Se$ QW lasers at various N ($\times 10^{18}$ cm^{-3}) indicated by the numbers. The arrow indicates that E increases with N; and (b) the corresponding E vs. $1/L$ curve. An increase in E (blue shift) of about 7 meV is obtained as $1/L$ increases from 5 to 13.5 cm^{-1} (i.e. L decreases from 2010 to 740 μm).

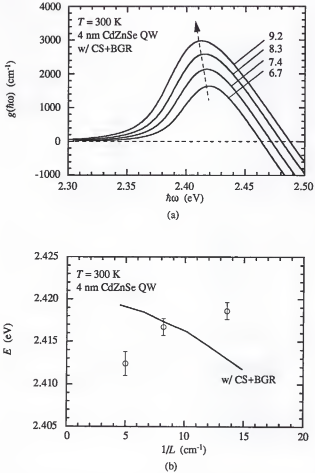

(a)

(b)

Figure 4.14 With CS and BGR included, (a) the calculated TE gain spectra for the 4 nm $Cd_{0.3}Zn_{0.7}Se$ QW lasers at various N ($\times 10^{18}$ cm^{-3}) indicated by the numbers. The arrow indicates that E decreases with N; and (b) the corresponding E vs. $1/L$ curve and the measured data. The predicted shift in E with $1/L$ is in the opposite direction to the measured shift.

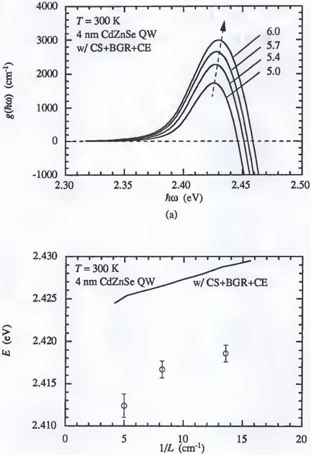

(a)

(b)

Figure 4.15 With CS, BGR and CE included, (a) the calculated TE gain spectra for the 4 nm $Cd_{0.3}Zn_{0.7}Se$ QW lasers at various N (× 10^{18} cm^{-3}) indicated by the numbers. The arrow indicates that E increases with N; and (b) the corresponding E vs. 1/L curve with the measured data. A blue shift in E of about 4 meV is obtained as 1/L increases from 5 to 13.5 cm^{-1}.

Comment #3. In previous work on the theory of CdZnSe QW lasers [Cho95b], it was predicted that E should shift to lower energies (longer wavelengths) as N increases from 4 to 5×10^{18} cm^{-3} in an 8 nm thick QW. In this work, we report on E vs. L measurements using 4 nm thick CdZnSe QW buried ridgeguide lasers [Hsu97b], which indicate that E shifts to higher energies (shorter wavelengths) as N increases. In addition, we use a single particle model [Cor93] modified by the addition of CE [Hau90, Cho94], carrier scattering [Asa93, Yam87] and bandgap renormalization [Cho94, Hau90] to calculate a dependence of E on N which is in good agreement with the experimental results.

4.4 Cavity Length Dependence of Threshold Current

Since the threshold gain increases with decreasing cavity length, the threshold current should also change as a function of cavity length. By investigating the cavity length dependence of threshold current, we are able to demonstrate the true mechanism behind the optical gain and spontaneous emission of semiconductor lasers.

4.4.1 Experiment

The experimental geometry is shown schematically in Fig. 4.16. The laser bar is put on probing stage with p-side up. The probe and stage are connected to "+" and "–", respectively, of a HP 214A pulse generator via co-axial cables with a current-varying pot in the circuit. A PIN-10D photo-detector is used to measure the laser output power from one facet. The measured voltage and current pulses in the circuit alone with output power pulse are sent to three separate channels of a Stanford Research System (SRS) where a pulse signal is averaged over a very short sampling gate placed in the middle of the pulse duration and converted to a DC signal representing the averaged value. Then a set of DC signals, representing voltage, current and output power, are sent to a personal computer (PC) for further data processing and a real-time output power P_o vs. current I curve is displayed on the PC monitor. By extrapolating the linear region of P_o vs. I curve back to the I axis, the cross-over is defined as the threshold current I_{th}. The voltage, current and power pulse signals can also be monitored simultaneously on an oscilloscope and compared to the reading shown on PC monitor.

InGaAs QW. Fig. 4.17 shows the measured I_{th} vs. L for the 8 nm $In_{0.15}Ga_{0.85}As$ single QW lasers with 100 μm stripe width. The open circle is the averaged I_{th} for the good laser devices tested from the same laser bar and the error bars represent the span of variation in I_{th}.

CdZnSe QW. Fig. 4.18 shows the measured I_{th} vs. L for the 4 nm $Cd_{0.3}Zn_{0.7}Se$ single QW lasers with 5 μm wide buried-ridge.

4.4.2 Prediction

In Section 4.3, we have shown that a certain value of N in QW is needed to provide a peak material gain g required for lasing at a given cavity length L. For diode lasers, N is provided by injecting current through metal contacts, as depicted in Fig. 4.19, where electrons and holes are injected to the active layer (or QW in the laser structures studied) from n- and p-side, respectively, and then recombine with each other. Under steady state condition, rate of injected electrons into QW is equal to the rate of recombining electron in QW which can be expressed mathematically as

$$\frac{\eta_i I}{e} = R_{rec} w L d_z, \tag{4.4}$$

where η_i is the injection efficiency which is defined as the fraction of current being injected into QW, I is the injected current, w is the stripe width, L is the cavity length, d_z is the QW thickness and R_{rec} is the rate of recombining electron per unit volume (in units of $s^{-1}cm^{-3}$). The recombination processes include a spontaneous recombination rate R_{sp}, a nonradiative

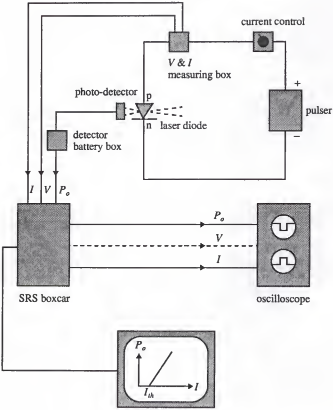

Figure 4.16 Illustration of experimental setup for measuring the output power P_o as a function of injection current I for diode lasers. By extrapolating the linear region of P_o vs. I curve back to the I axis, the cross-over is defined as the threshold current I_{th}.

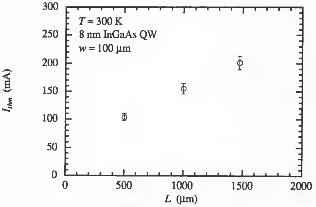

Figure 4.17 Measured threshold currents I_{thm} of various laser cavity lengths L for the 8 nm $In_{0.15}Ga_{0.85}As$ QW lasers. The error bars show the variation of I_{thm} obtained from each laser bar and the open circles are the corresponding average values of I_{thm}.

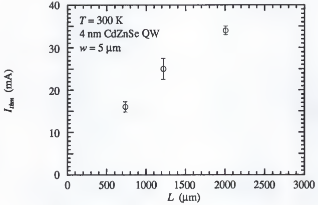

Figure 4.18 Measured threshold currents I_{thm} of various laser cavity lengths L for the 4 nm $Cd_{0.3}Zn_{0.7}Se$ QW lasers. The error bars show the variation of I_{thm} obtained from each laser bar and the open circles are the corresponding average values of I_{thm}.

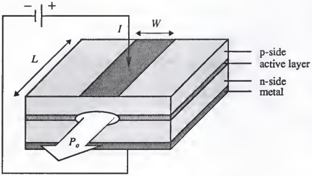

Figure 4.19 Schematic sketch of a current-injected diode laser device. Holes and electrons are injected from the p-side and n-side, respectively, and then radiatively recombine with each other in the active layer.

recombination rate R_{nr}, a carrier leakage rate R_l and a stimulated recombination rate R_{st}. Thus, we can write [Col95]

$$R_{rec} = R_{sp} + R_{nr} + R_l + R_{st}. \tag{4.5}$$

For a laser below or at threshold where the photon density is relatively low, R_{st} is negligible. With $R_{st} \approx 0$ and using Eq. (4.5) in Eq. (4.4), we obtain

$$\frac{\eta_i I}{e} = (R_{sp} + R_{nr} + R_l)\, wLd_z. \tag{4.6}$$

Since the exact dependence of R_{nr} and R_l on I is unknown, a conventional approach to deal with this problem is to define a radiative officiating η_r as

$$\eta_r \equiv \frac{R_{sp}}{R_{sp} + R_{nr} + R_l}. \tag{4.7}$$

Then, substituting $R_{sp} + R_{nr} + R_l$ in Eq. (4.6) in terms of R_{sp} and η_r using Eq. (4.7), we can rewrite Eq. (4.6) as

$$\eta_i \eta_r I = ed_z R_{sp} wL, \tag{4.8}$$

which means that a fraction (= $\eta_i \eta_r$) of I gives rise to the spontaneous recombination rate in QW. For the convenience, we define a radiative current density J_{rad} as the component of I which gives rise to the spontaneous recombination

$$J_{rad} wL \equiv \eta_i \eta_r I. \tag{4.9}$$

Combining Eqs. (4.8) and (4.9), we obtain

$$J_{rad} \equiv ed_z R_{sp}. \tag{4.10}$$

Recalling that $R_{sp}(\hbar\omega)$ is the spontaneous recombination rate per unit volume per unit energy at $\hbar\omega$ (in units of $s^{-1}cm^{-3}eV^{-1}$), R_{sp} (in units of $s^{-1}cm^{-3}$) is then just the integration of $R_{sp}(\hbar\omega)$ over all $\hbar\omega$ [Col95]

$$R_{sp} = \int_0^\infty R_{sp}(\hbar\omega)\, d(\hbar\omega). \tag{4.11}$$

As a consequence of using Eq. (4.11) in Eq. (4.9), J_{rad} can be expressed as

$$J_{rad} = ed_z\int_0^\infty R_{sp}(\hbar\omega)\,d(\hbar\omega)\,. \tag{4.12}$$

Specifying N and T, $R_{sp}(\hbar\omega)$ can be calculated using Eq. (3.2) with inclusion of CS (without CE) and Eq. (3.63) with inclusion of CE. Effect of CE on J_{rad} can thus be calculated by using Eq. (4.12).

4.4.2.1 Gain-current relation

The first step in predicting I_{th} for a given laser is to determine the value of J_{rad} required to achieve g_{th} for that laser. Specifying N and temperature T, we can calculate $g(\hbar\omega)$ and $R_{sp}(\hbar\omega)$ based on the model chosen (see Chapter 2 and 3). The peak material gain g can therefore be found from $g(\hbar\omega)$ and by using Eq. (4.12), J_{rad} can be calculated from $R_{sp}(\hbar\omega)$. As a consequence, a g-J_{rad} pair is generated for a given N. By repeating this procedure for various N, which is illustrated in Fig. 4.20, a g-J_{rad} curve (gain–current relation) is created for a given laser structure. The cross-over of a g-J_{rad} curve at the J_{rad} axis is defined as the transparency current density J_{tr} where the material becomes transparent for $g = 0$.

InGaAs QW. Fig. 4.21 shows the g-J_{rad} curves calculated with and without CE for the 8 nm $In_{0.15}Ga_{0.85}As$ QW lasers. The model with CE included predicts 70 A/cm^2 for J_{tr} while the model without CE included predicts 65 A/cm^2 for J_{tr}. For low J_{rad} values, the model with CE predicts g values lower than those without CE. For J_{rad} values higher than the cross point of the two curves, the model with CE predicts g values a bit higher than those without CE. This difference is important in predicting the threshold current I_{th} discussed in the next subsection.

CdZnSe QW. Fig. 4.22 shows the g-J_{rad} curves calculated with and without CE for the 4 nm $Cd_{0.3}Zn_{0.7}Se$ QW lasers. The model with CE included predicts 150 A/cm^2 for J_{tr} while the model without CE included predicts 120 A/cm^2 for J_{tr}. For low J_{rad} values, the model with CE predicts g values lower than those without CE. For J_{rad} values higher than the cross point of the two curves, the model with CE predicts g values much higher than those without CE. This effect of CE on the g-J_{rad} relation will be shown to be very important in predicting the threshold current I_{th} accurately discussed in the next subsection.

Comparison. Comparing Fig. 4.21 with Fig. 4.22, we observe that CE obviously has a much more profound effect on the g-J_{rad} relation for the CdZnSe QW lasers than for the InGaAs QW lasers. This again demonstrates that, as expected, CE is stronger in wide bandgap materials than in narrow bandgap materials.

As mentioned in Section 2.6, a CdZnSe QW laser structure has a higher transparent carrier density N_{tr} than an InGaAs QW laser structure, resulting from the fact that the CdZnSe QW has heavier carrier effective masses. This larger N_{tr} shows up as higher J_{tr} values in g-J_{rad} curves for the CdZnSe QW than the InGaAs QW (about twice higher), as shown in Figs. 4.21 and 4.22. It looks like that the CdZnSe QW lasers will not be as good as the InGaAs QW lasers, since they require higher transparency to achieve gain in the QW. However, the strong CE effect in the CdZnSe QW lasers results a very steep g-J_{rad} curve, as shown in Fig. 4.22, which indicates that the CdZnSe QW lasers can be as good as the InGaAs QW lasers or ever better. To understand why CE increase the slope of a g-J_{rad} curve, we plot g and J_{rad} as a function of N in Figs. 4.23 and 4.24 for the 8 nm $In_{0.15}Ga_{0.85}As$ and the 4 nm $Cd_{0.3}Zn_{0.7}Se$ QW lasers, respectively. As shown, the enhancements in g due to CE are higher than those in J_{rad}, especially for the CdZnSe QW lasers. As a consequence, the slope of a calculated g-J_{rad} curve is larger with CE included than without CE.

4.4.2.2 Predicting threshold current

Since g_{th} is known for a given L through Eq. (4.3), the predicted value of J_{rad} at threshold, defined as $J_{rad,\,th}$, can be determined from the g-J_{rad} curve, as depicted in Fig. 4.20. To the extent that current and carrier spreading beyond the stripe area (lateral leak-

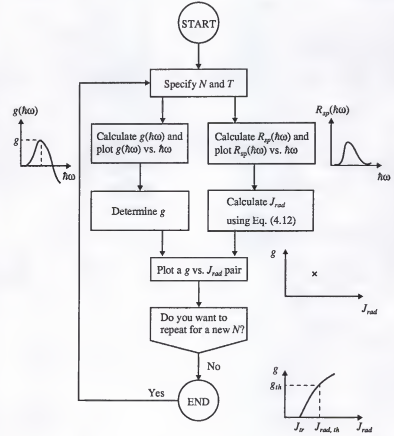
START
Specify N and T
Calculate g(ħω) and plot g(ħω) vs. ħω
Calculate R_sp(ħω) and plot R_sp(ħω) vs. ħω
Determine g
Calculate J_rad using Eq. (4.12)
Plot a g vs. J_rad pair
Do you want to repeat for a new N?
No
Yes
END
g(ħω)
g
ħω
R_sp(ħω)
ħω
g
×
J_rad
g
g_th
J_tr
J_rad, th
J_rad

Figure 4.20 Flow chart of the procedures for obtaining a theoretical g vs. J_{rad} curve.

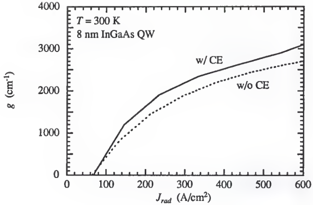

Figure 4.21 Effect of CE on the relation between peak gain g and radiative current density J_{rad} for the 8 nm $In_{0.15}Ga_{0.85}As$ QW lasers. The solid line is calculated with inclusion of CE and the dotted line is calculated without CE.

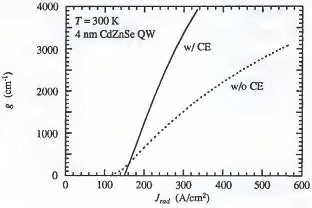

Figure 4.22 Effect of CE on the relation between peak gain g and radiative current density J_{rad} for the 4 nm $Cd_{0.3}Zn_{0.7}Se$ QW lasers. The solid line is calculated with inclusion of CE and the dotted line is calculated without CE.

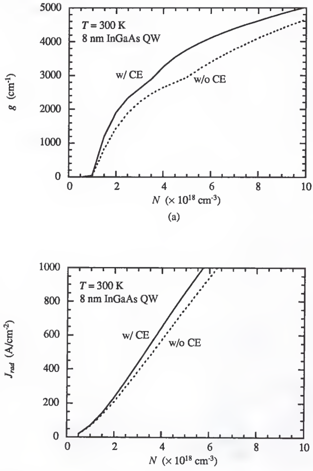

(a)

(b)

Figure 4.23 Effects of CE on peak gain g and radiative current density J_{rad} for the 8 nm $In_{0.15}Ga_{0.85}As$ QW lasers. (a) g as a function of N; and (b) J_{rad} as a function of N. The solid lines are calculated with inclusion of CE and the dotted lines are calculated without CE.

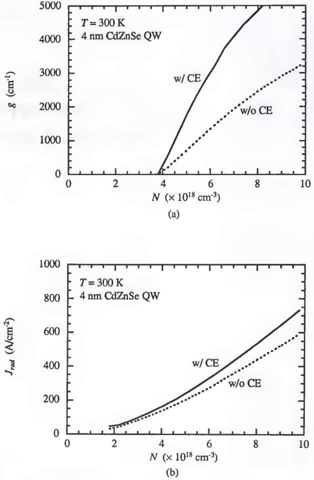

Figure 4.24 Effects of CE on peak gain g and radiative current density J_{rad} for the 4 nm $Cd_{0.3}Zn_{0.7}Se$ QW lasers. (a) g as a function of N; and (b) J_{rad} as a function of N. The solid lines are calculated with inclusion of CE and the dotted lines are calculated without CE.

age) can be ignored, $J_{rad,\,th}\,wL \equiv I_{rad,\,th}$ is the predicted fraction of total current giving rise to spontaneous emission in the QW at threshold. Using Eq. (4.9), we obtain the predicted value of I_{th} for a given L

$$I_{th} = \frac{I_{rad,\,th}}{\eta_r \eta_i}. \tag{4.13}$$

where η_r is assumed to be unity in our lasers.

If the high conductivity p^+ cap layer was not removed in the area outside the stripe region, like the InGaAs QW lasers studied in these experiments (see Fig. 4.1), the lateral leakage current I_{lk} can be significant [Gro94]. As a consequence, I_{lk} must be subtracted from the measured value of I_{th}, that is I_{thm}, in order to compare with the value of I_{th} predicted using Eq. (4.13). However, when I_{lk} is significant, the "measured" value of $\eta_i \equiv \eta_{im}$, determined from the $1/\eta_d$ vs. L plot, must also be corrected [Hu94]. It can be shown that when I_{lk} does not contribute to the laser power (true for our lasers where the lateral width of the laser emission at the facet is about the same as the stripe width $w = 100\ \mu\text{m}$), then the predicted value of threshold current I_{thp} is given by

$$I_{thp} = \frac{I_{rad}}{\eta_r \eta_{im}}. \tag{4.14}$$

As a consequence, one can compare I_{thp} to I_{thm} without actually determining I_{lk}.

InGaAs QW. Given $\eta_{im} = 0.65$ and $\eta_r = 1$, the I_{thp} vs. L curves calculated with and without CE for the 8 nm $In_{0.15}Ga^{0.85}As$ QW lasers are plotted in Fig. 4.25 along with the measured I_{thm} at three cavity lengths. It is clear that the model with CE does a better job than the model without CE in predicting I_{thm}.

CdZnSe QW. Given $\eta_{im} = 0.69$ and $\eta_r = 1$, plots of I_{thp} as a function of L calculated with and without CE for the 4 nm $Cd_{0.3}Zn_{0.7}Se$ QW lasers are shown in Fig. 4.26 along with the measured I_{thm} at three cavity lengths. The model without CE obviously overestimate the threshold currents by about 40% to 50% of the measured threshold currents. With inclusion of CE, the prediction shows improved agreement with the experiment.

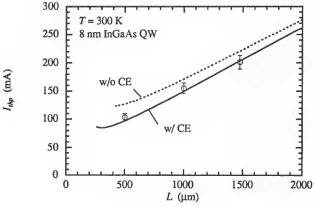

Figure 4.25 Effect of CE on the predicted threshold current I_{thp} as a function of cavity length L for the 8 nm $In_{0.15}Ga_{0.85}As$ QW lasers. The solid line is calculated with inclusion of CE and the dotted line is calculated without CE. Measured threshold currents I_{thm} of three cavity lengths L = 500, 1000 and 1500 μm are also shown as the open circles with error bars.

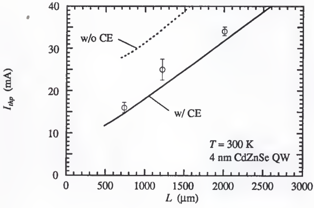

Figure 4.26 Effect of CE on the predicted threshold current I_{thp} as a function of cavity length L for the 4 nm $Cd_{0.3}Zn_{0.7}Se$ QW lasers. The solid line is calculated with inclusion of CE and the dotted line is calculated without CE. Measured threshold currents I_{thm} of three cavity lengths L = 740, 1220 and 2010 μm are also shown as the open circles with error bars.

4.5 Temperature Dependence of Lasing Energy

4.5.1 Experiment

A chip of the 4 nm $Cd_{0.3}Zn_{0.7}Se$ QW laser with the structure shown in Fig. 4.2 was cleaved from the laser bar with L = 1219 μm. Then using EPO-TEK H20E silver epoxy, the laser chip was mounted with p-side up on the Cu-block and Au-wire bonded to one of the Au probing pads evaporated on the tops of two ceramic standoffs, as illustrated in Fig. 4.27(a). To avoid thermally degrading the CdZnSe QW laser, this chip-on-block (COB) package was left in the room temperature for 36 hours and then baked in 50°C for 1 hour to cure the silver epoxy. As sketched in Fig. 4.27(b), the COB was loaded to a Cu-fixture and a Cu-sheet, which was tightened with two plastic screws to the Cu-fixture with a ceramic board in between, was used to make contact with the two standoffs of the COB. The whole fixture was loaded into the Laser Photonics L5736 cryostat and the wire soldered on the Cu-sheet was connected to the circuit board inside the cryostat which was externally connected to the HP214A pulse generator and the Laser Photonics L5720 temperature controller. After the cryostat was sealed and vacuumed down to 20 mtorr, the temperature inside the cryostat was cooled down using liquid nitrogen and controlled by the temperature controller. The laser device was characterized using 1 μsec wide pulses at a 1 kHz repetition rate. The laser beam, emitting from one of cleaved facet and passing through the quartz window of the cryostat, was imaged to the OMA to record the spectra of the light output and determine the lasing wavelength, just like the one shown in Fig. 4.7. Fig. 4.28 shows the measured values of the lasing energy E at various temperatures T in the range from 82 to 300 K. It is found that as T reduces, E shifts to higher energies (a blue shift). Using a linear fit to the data points (plotted as the dotted lines), the increasing rate of E with decreasing T is found to be about 0.48 meV/K for temperatures between 160 K and 300 K while for temperatures below 160 K and above 82 K, the increasing rate is smaller and about 0.32 meV/K.

4.5.2 Prediction

Using Eq. (4.3), the required threshold material gain g_{th} for the 4 nm $Cd_{0.3}Zn_{0.7}Se$ QW laser with $L = 1219$ μm is estimated to be around 2159 cm^{-1}. Using the model with many-body effects included, the TE gain spectra at various temperatures with peak gain value reaching the required g_{th} are calculated. The TE gain spectra in Figs. 4.29(a) are calculated with inclusion of CS at the threshold carrier densities $N_{th} = 7.4$, 5.4 and 3.2×10^{18} cm^{-3} for $T = 300$, 240 and 160 K, respectively, and under the same conditions, the TE gain spectra in Figs. 4.29(b) are calculated with inclusion of CS and BGR. In addition to CS and BGR, the TE gain spectra in Figs. 4.29(c) are calculated with inclusion of CE at the $N_{th} =$ 5.23, 3.65, 2.07×10^{18} cm^{-3} for $T = 300$, 240 and 160 K, respectively. All plots show that the gain spectra blue shift to higher energies as the T decreases. This is mainly due to the fact that the bandgap of semiconductor material increases with decreasing temperature.

As discussed in section 4.3.2 that E is determined by the spectral location of the peak gain at threshold, Fig. 4.30 shows plots of E as a function of T determined from the calculated threshold gain spectra (see Fig. 4.29) at temperatures in the range from 160 to 300 K. With only CS included, the predicted E values are about 65 to 85 meV higher than the measured E values and a blue shift of 49 meV in E is obtained for T decreasing from 300 K to 160 K. The measured shift of E within the same range of T is found to be about 67 meV from Fig. 4.28, a factor of 1.37 larger. With BGR also included, the predicted E values are close to the measured E values, but the corresponding shift of E with T is about 76 meV. In addition to CS and BGR, the model with CE included predicts a blue shift of about 71 meV which is in the best agreement with the experiment among all three models. As a consequence, it is important to include CE in the theory in predicting the dependence of lasing energy on temperature between 160 and 300 K for the 4 nm $Cd_{0.3}Zn_{0.7}Se$ QW lasers.

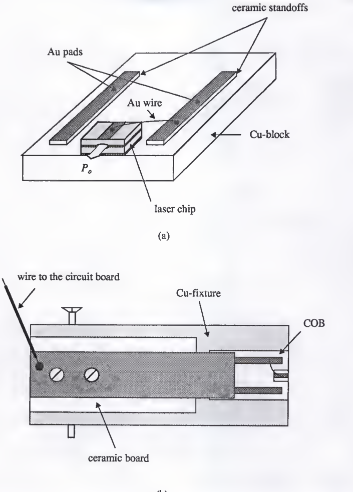

Figure 4.27 Schematic diagrams of (a) mounting the laser chip on the Cu-block (COB) and (b) loading the COB to the Cu-fixture.

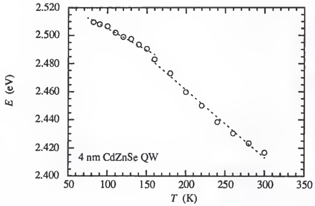

Figure 4.28 The measured lasing energy E as a function of temperature T for the 4 nm $Cd_{0.3}Zn_{0.7}Se$ QW laser with L = 1219 μm. The open circles are the measured data and two dotted lines are linearly fitted to the data over two temperature ranges, between 82 and 160 K and between 160 K and 300 K.

For T lower than 160 K, the CE model reaches its limits due to the random phase approximation (RPA) made in considering the screening effects and the Padé approximation made in deriving the Coulomb enhancement factor, as discussed in Chapter 3. It is interesting to notice that 160 K is also the temperature at which the measured increasing rate in E with decreasing T slows down. This may imply that excitons become important at temperature below 160 K. At cryogenic temperatures, the role of phase transition between excitons and electron-hole plasma in the stimulated emission processes of CdZnSe QW laser structures has been discussed extensively by Cingolani *et al.* in [Cin96].

4.6 Summary

In this chapter, the cavity length dependences of lasing energy and threshold current were both studied using the InGaAs and CdZnSe QW lasers. It has been demonstrated that predictions using the theory with Coulomb enhancement included are in good agreement with the experiments. The importance of Coulomb enhancement in the CdZnSe QW lasers was also justified by the excellent agreement found between the measured temperature dependence of lasing energy and the prediction with CE included at temperatures between 160 K and 300 K.

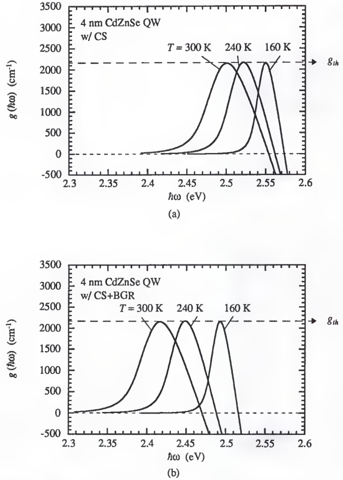

Figure 4.29 Calculated TE gain spectra at T = 300, 240 and 160 K for the 4 nm $Cd_{0.3}Zn_{0.7}Se$ QW laser with L = 1219 μm at threshold, where the required threshold material gain g_{th} is about 2159 cm^{-1}, using models (a) with CS included; (b) with CS and BGR included; (c) with CS, BGR and CE included.

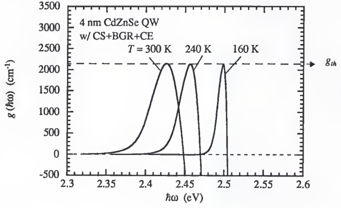

(c)

Figure 4.29 -- continued.

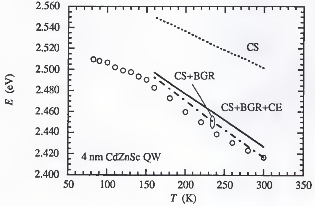

Figure 4.30 Temperature *T* dependence of the lasing energy *E* for the 4 nm $Cd_{0.3}Zn_{0.7}Se$ QW laser with cavity length $L = 1219$ μm. The open circles are the experimental measurements, the dotted curve is calculated with inclusion of CS, the dash-dotted curve is calculated with inclusion of CS and BGR and the solid curve is calculated with inclusion of CS, BGR and CE.

CHAPTER 5
ABSORPTION RESONANCES DUE TO COULOMB ATTRACTION

5.1 Introduction

As discussed in Chapter 3, exciton binding energy in II-VI CdZnSe QW is larger than in III-V InGaAs QW for its heavier electron and hole effective masses and smaller dielectric constant, exciton lasing mechanism in II-VI CdZnSe QW was ever suggested [Din92, Din93, Din94, Hag92]. This excitonic origin of lasing is very different from the conventional EHP theory saying that the optical gain in semiconductor lasers is provided by the recombination of electrons and holes in the active layers or quantum wells of our interests.

In this chapter, first, we will review some of the experiments that were claimed as the evidences for the excitonic gain in CdZnSe QW lasers and excitonic emission in CdZnSe light emitting diodes (LEDs). Then, we will use the models developed in Chapters 2 and 3 to show many-body effects (CS, BGR and CE) also modify the absorption spectra at low carrier densities as well as gain spectra at high carrier densities. Finally, we will compare the calculation results to the experimental observations and, without appealing to excitons, we attempt to explain several spectral features claimed as proofs for excitonic gain and emission in CdZnSe QW.

5.2 Claims of Evidence for Excitonic Gain

As shown in Fig. 5.1, M. Hagerott *et al.* [Hag92] observed close spectral correlation between the so-called exciton absorption and the spontaneous emission spectra of the

CdZnSe QW light emitting diodes (LEDs) at $T = 77$ and 300 K. It was suggested that the room temperature LED emission of the CdZnSe QW is of excitonic origin. J. Ding *et al.* [Din92] reported the first observation of so-called excitonic gain and laser emission in ZnSe-based QWs which drew a great deal of attention in the CdZnSe research society at that time. Fig. 5.2 shows their experimental data measured at $T = 77$ and 295 K where laser emission evolved from the low-energy tail of a resonance-like absorption peak. This absorption peak was attributed to the $n = 1$ HH exciton absorption resonance and the close spectral following of laser emission on its low-energy side was interpreted as excitonic lasing in nature. A phenomenological model of optical gain was proposed based on partial phase-space filling (PSF) of an inhomogeneously broadened exciton resonance and including the effects of exciton-phonon interaction. This phenomenological gain model was used to explain their pump-probe spectroscopic experiments at cryogenic temperature up to 220K [Din93]. The gain/absorption spectra of Fig. 5.3 reconstructed from transient pump-probe techniques show the coexistence of optical gain with the so-called exciton absorption resonance in time frame [Din93]. This was said to, quoted from the paper, "... provide the ultimate proof that the well-defined $n = 1$ HH exciton resonance (absorption peak) provides optical gain at its low-energy side." The room temperature gain/absorption spectra of CdZnSe QW diode lasers, which were determined via a transformation from the unamplified spontaneous emission [Hen80, Kes94] through an opening in the top contact of lasers, were shown in Fig. 5.4 and two resonance-like absorption peaks appearing at low excitation level were attributed to absorption from $n = 1$ HH and LH excitons [Din94].

5.3 Calculation of Gain/Absorption Spectra

In Chapter 3, we have shown how the gain spectra for carrier density N greater than the transparent carrier density N_{tr} change when various many-body effects (CS, BGR and CE) are included one by one in the calculations. As lowering N smaller than N_{tr}, gain spec-

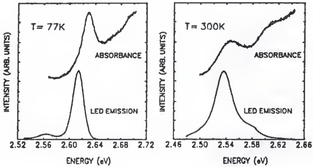

Figure 5.1 Comparison of absorption and spontaneous emission spectra near the so-called $n = 1$ HH exciton resonance of a CdZnSe QW LED at $T = 77$ K and 300 K [Hag92].

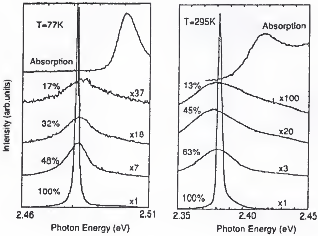

Figure 5.2 Evolution of the edge emission of a CdZnSe QW laser at $T = 77$ and 295 K. The excitation level is indicated by the percentage of what is just above the threshold. The so-called $n = 1$ HH exciton absorption resonance is shown for reference and the close spectral following of laser emission on its low-energy side was interpreted as excitonic lasing in nature [Din92].

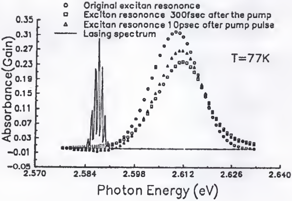

Figure 5.3 The so-called $n = 1$ HH exciton absorption resonance of a CdZnSe QW laser at $T = 77$ K without photoexcitation (circles), 300 fs (squares) and 10 ps (triangles) after the photoexcitation. The laser emission spectrum is also shown. Coexistence of gain and resonance-like absorption was elucidated as that optical gain in CdZnSe QW lasers is provided by excitons [Din93].

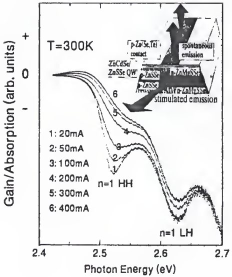

Figure 5.4 Gain/absorption spectrum of a CdZnSe QW diode laser at $T = 300$ K, showing the effects of increasing current injection on the so-called $n = 1$ HH and LH QW exciton states. The inset shows the experimental geometry for recording the spontaneous and stimulated emission spectra [Din94].

tra become absorption spectra. In this section, we will show how many-body effects modify the absorption spectra.

Single-Particle Model. The TE gain/absorption spectra for $N = 2.2 \times 10^{18}$ and 5.4×10^{18} cm^{-3} at $T = 300$ K, calculated using Eq. (2.25), are shown in Fig. 5.5(a). Two discontinuities, resulting from the stair-step density of states in QW structure, occur at photon energies $E_{g1,hh}$ and $E_{g1,lh}$ which correspond to the energy gaps between C1 and HH1 subbands and between C1 and LH1 subbands, respectively. For $N = 2.2 \times 10^{18}$ cm^{-3}, the whole spectrum is under absorption. For $N = 5.4 \times 10^{18}$ cm^{-3}, the spectrum experiences gain at photon energies between $E_{g1,hh}$ and the quasi-Fermi level separation. Since the measured gain/absorption spectra shown in Fig. 5.4 do not have discontinuous features, it is clear that this model is incomplete. Next we will show when many-body effects are incorporated into the single-particle model, realistic gain/absorption spectra are obtained.

Many-body effects – CS. The CS-modified single-particle TE gain/absorption spectra are plotted in Fig. 5.5(b) for $N = 2.2 \times 10^{18}$ and 5.4×10^{18} cm^{-3}. It is evident that these spectra are broadened and smoothed relative to their single-particle counterparts plotted in Fig. 5.5(a). The peak gain for $N = 5.4 \times 10^{18}$ cm^{-3} is reduced significantly and its spectral location is blue-shifted to higher photon energy (in this case by about 11.5 meV). For $N = 2.2 \times 10^{18}$ cm^{-3}, the two absorption steps due to C1-HH1 and C1-LH1 transitions remain visible, but there is no sign of resonance-like absorption peaks as the ones observed in experiment (see Fig. 5.4).

Many-body effects – BGR. The corresponding BGR shifted spectra of Fig. 5.5(b) are shown in Fig. 5.5(c) where low-energy tails of gain and absorption spectra are well below (~ 80 meV) the unexcited C1-HH1 energy gap $E_{g1,hh}$. This situation is often mistakenly elucidated as the evidence for existence of excitons in CdZnSe QW lasers even at room temperature [Din94].

Many-body effects – CE. Plots of calculated TE gain spectra with CE included for $N = 2.2 \times 10^{18}$ and 5.4×10^{18} cm^{-3} are shown in Fig. 5.5(d). Comparing Fig. 5.5(d) to (c), not only does CE increase g for high N, but also enhances the absorption steps to resonance-like absorption peaks for low N. Much resemblance between the theoretical results and experimental observation will be discussed in the following section in details.

5.4 Comparison between Calculations and Experiments

5.4.1 Spectral Correlation between Peaks of Absorption and Spontaneous Emission

As shown in Fig. 5.1, the peak positions of the absorption peak and spontaneous emission peak were found to be very close to each other at both $T = 77$ and 300 K and this close spectral correlation was interpreted as the strong evidence for that the room temperature LED emission is of excitonic origin. Here we use Eq. (3.63) (with CE included) to calculate the spontaneous emission spectrum for $N = 4.2 \times 10^{18}$ cm^{-3}, as shown in Fig. 5.6. The absorption spectrum for $N = 2.2 \times 10^{18}$ cm^{-3} in Fig. 5.4(d) is replotted in Fig. 5.6 with an inverse sign in arbitrary units for reference. We observe that the peak position of the spontaneous emission spectrum is very close to the position of the resonance-like absorption peak. It is clear by comparing to Fig. 5.1 that we are able to predict this correlation at $T = 300$ K without appealing to excitons.

5.4.2 Energy Arrangement of Some Key Spectral Features

In experiment, the lasing emission spectra of CdZnSe QW lasers was found to overlap with the low-energy tails of their resonance-like absorption spectra, as shown in Fig. 5.2, which were often identified as exciton absorption spectra [Din92, Din93]. The lasing energy E, defined as the photon energy at the peak of the stimulated emission spectra, is red shifted with respect to E_x and E_{g1}, defined as the spectral position of the $n = 1$ HH exciton absorption peak and the energy gap between the lowest subbands in CB and VB, on the or-

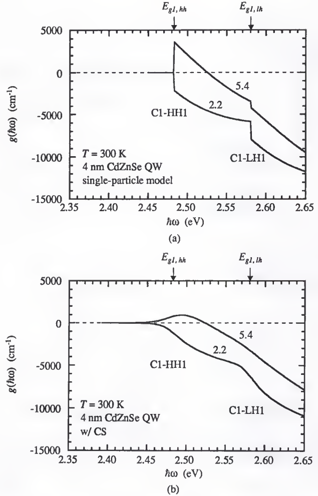

Figure 5.5 Calculated TE gain/absorption spectra for the 4 nm $Cd_{0.3}Zn_{0.7}Se$ QW lasers at carrier densities indicated by the numbers (× 10^{18} cm^{-3}) using (a) single-particle model; (b) with CS; (c) with CS and BGR; (d) with CS, BGR and CE.

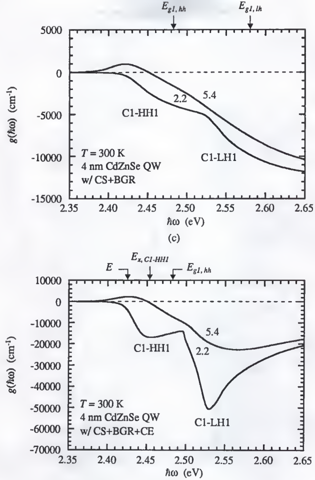

(c)

(d)

Figure 5.5 -- continued.

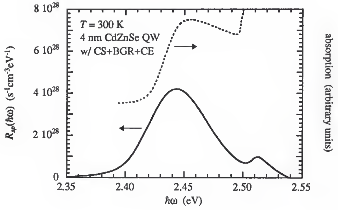

Figure 5.6 Calculated spontaneous emission spectrum for the 4 nm $Cd_{0.3}Zn_{0.7}Se$ QW LEDs at $N = 4.2 \times 10^{18}$ cm^{-3} with CE included. The absorption spectrum for $N = 2.2 \times 10^{18}$ cm^{-3} in Fig. 5.4(d) is replotted as the dotted curve with an inverse sign and in arbitrary units for reference.

der of 20 and 60 meV respectively [Din93].

In theory, for typical cleaved-facet lasers, E can be predicted by the spectral location of the peak of gain spectrum as discussed in Section 4.3. For example, $E = 2.427$ eV, determined from the calculated gain/absorption spectrum for $N = 5.4 \times 10^{18}$ cm^{-3} in Fig. 5.5(d), corresponds to the lasing energy for a CdZnSe QW laser with $L = 1082$ µm. Comparing to the calculated spectrum for $N = 2.2 \times 10^{18}$ cm^{-3} in Fig. 5.5(d), E is related to $E_{x,\,C1\text{-}HH1} =$ 2.455 eV and $E_{g1,\,hh} = 2.482$ eV, defined as the spectral position of the C1-HH1 absorption peak and the C1-HH1 subband energy gap, by a red shift of about 28 and 55 meV respectively. These numbers are comparable to the corresponding experimentally measured values mentioned earlier (20 and 60 meV respectively). In our gain model based on EHP, the red shifts are mainly due to bandgap renormalization from the screening of Coulomb repulsion among charge carriers and the resonance-like absorption peaks are due to the enhanced transition matrix element from Coulomb attraction between electron-hole pairs.

5.4.3 Coexistence of Gain with Absorption

The coexistence of optical gain with the so-called exciton absorption observed at low temperature ($T = 77$ K), as shown in Fig. 5.3, was explained as the "ultimate proof" that the optical gain in CdZnSe QW is provided by the well-defined $n = 1$ HH exciton resonance [Din93]. For this reason, it is interesting for us to perform calculation at temperatures lower than 300 K with CE included. As shown in Fig. 5.7(a), the TE gain/absorption spectrum, calculated at $T = 200$ K for $N = 3 \times 10^{18}$ cm^{-3}, shows the existence of gain while the C1-HH1 absorption peak remains well defined at higher energy. As decreasing the temperature further down to 160 K, observed from the calculation result plotted in Fig. 5.7(b) for $N = 2.1 \times 10^{18}$ cm^{-3}, the C1-HH1 absorption peak becomes sharper and narrower with coexistence of gain on its low-energy side. As mentioned in Section 4.5.2, the CE model used in this work reaches it limits at temperature lower than 160 K where excitons may become important. Although we are not able to make predictions at 77 K using this CE model, coexistence of gain with resonance-like absorption in CdZnSe QW lasers has been predicted for temperature down to 160 K, without appealing to excitons.

5.4.4 Evolution of Gain/Absorption Spectra with Injection Level

Fig. 5.8 shows the TE gain/absorption spectra at T = 300 K for various values of N which correspond to various injection levels. At lower injection levels ($N = 2.2$ and 3.0×10^{18} cm^{-3}), both C1-HH1 and C1-LH1 absorption peaks are well defined. As increasing injection level ($N = 3.8$ and 4.6×10^{18} cm^{-3}), the C1-HH1 absorption peak begins to saturate. For $N > 3.8 \times 10^{18}$ cm^{-3} gain appears on the low-energy side of the spectra. At even higher injection levels corresponding to lasing threshold ($N = 5.4$ and 6.2×10^{18} cm^{-3}), the C1-HH1 absorption peak becomes hardly identifiable while the C1-LH1 absorption peak remains resolvable. These characteristics of the gradual evolution of gain/absorption spectra were also experimentally observed at room temperature for CdZnSe QW lasers [Din94] (see. Fig. 5.4), but the optical gain was said to be excitonic in nature.

5.5 Summary

As just being briefly reviewed in Section 5.2, several key spectral features observed in experiments were identified as the evidence for existence of excitons and the optical gain mechanism in wide bandgap CdZnSe QW lasers was further said to be excitonic in nature, unlike the narrow bandgap III-V QW lasers for which optical gain comes from EHP [Col95, Cor93]. To our best knowledge, no complete theory has ever been reported for the physical mechanism responsible for absorption as well as gain in II-VI CdZnSe QW diode lasers at room temperature. In this chapter, without appealing to excitons, we have success-

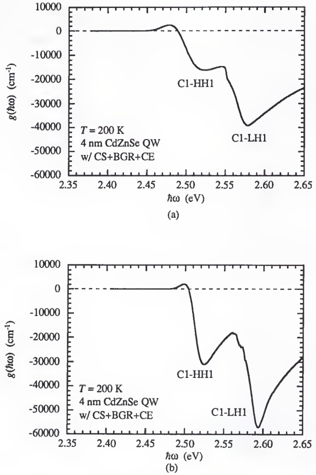

(a)

(b)

Figure 5.7 Calculated TE gain/absorption spectra for the 4 nm $Cd_{0.3}Zn_{0.7}Se$ QW lasers with CE at (a) T = 200 K, $N = 3 \times 10^{18}$ cm^{-3} and (b) T = 160 K, $N = 2.1 \times 10^{18}$ cm^{-3}, showing the coexistence of optical gain and the resonance-like C1-HH1 absorption peak.

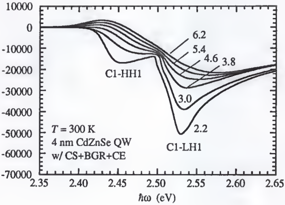

Figure 5.8 Calculated TE gain/absorption spectra for the 4 nm $Cd_{0.3}Zn_{0.7}Se$ QW lasers with CE at carrier densities indicated by the numbers ($\times 10^{18}$ cm^{-3}), showing the effects of increasing carrier density (or increasing injection level) on the resonance-like C1-HH1 and C1-LH1 absorption peaks.

fully demonstrated that these key spectral features at room temperature can be reproduced by using the conventional electron-hole plasma theory modified by many-body effects. Especially, Coulomb attraction effect between electrons and holes in CdZnSe QW lasers has been shown being very important at room temperature.

CHAPTER 6
CARRIER-INDUCED EFFECTS IN II-VI QW LASERS

6.1 Introduction

The optical gain in semiconductor lasers is provided by carrier injection into the active layer and the sequential recombinations of electron-hole pairs. The relationship between the optical gain and the carrier density in the QW structure has been described in Chapters 2 and 3 using the EHP theory with various many-body effects included. Since the imaginary part of the refractive index is linearly related to the optical gain [Col95], any change in the optical gain due to the change in the carrier density would result in a change in the imaginary refractive index. In a conventional approach, the change in the real part of the refractive index can then be determined from the change in its imaginary part using a Kramers-Kronig (KK) transformation [Hen81]. It has been shown both theoretically and experimentally that in III-V GaAs-based bulk and QW lasers, the real refractive indices at gain peaks (or at lasing energies) reduces with increasing carrier density and thus with increasing optical gain [Hen80, Hen81, Kes90, Kes91, Tie92]. For the gain-guided GaAs-based QW laser, the carrier-induced reduction in the real refractive index in the QW has been shown to affect the quality of the laser beam [Col91, Shi89]. However, on the contrary, a theoretical calculation reported that the significant Coulomb enhancement in room-temperature II-VI CdZnSe QW lasers results in increases in the real refractive indices at gain peaks with increasing carrier density [Cho94]. If this prediction is correct, the beam quality of the CdZnSe QW lasers should be different from that of the GaAS-based QW lasers.

This chapter is devoted to investigating the effects of injected carriers on the refractive index and, therefore, on the beam quality of the II-VI CdZnSe QW lasers at room temperature. First, the relations between the optical gain, the complex dielectric function and the complex refractive index will be derived. Without using the KK transformation method [Hen81], the real refractive index, as well as the imaginary refractive index, as a function of photon energy will be calculated using the EHP theory with many-body effects included. Effects of carriers in the QW on the refractive index will be presented. A qualitative description of the effect of carrier-induced refractive index change on the lateral profile of a laser beam at the laser facet (near-field pattern) will be given. Finally, experimental results from the measurement of the near-field patterns using CdZnSe QW lasers will be presented.

6.2 Effect of Injected Carriers on the Refractive Index

6.2.1 Complex Optical Dielectric Function

The complex optical dielectric function $\tilde{\varepsilon}(\hbar\omega)$ is related to the complex optical susceptibility $\tilde{\chi}(\hbar\omega)$ by [Cho94, Hau90, Kli97]

$$\tilde{\varepsilon}(\hbar\omega) = \varepsilon_{\infty}[1 + \tilde{\chi}(\hbar\omega)] , \qquad (6.1)$$

where ε_{∞} is the background dielectric constant. In Eq. (3.57), the relation between the optical gain function $g(\hbar\omega)$ and the imaginary part of $\tilde{\chi}(\hbar\omega)$ is given and in an analogy, one can define a complex function $\tilde{g}(\hbar\omega)$ as

$$\tilde{g}(\hbar\omega) = \frac{\omega\bar{n}}{c} i\tilde{\chi}(\hbar\omega) , \qquad (6.2)$$

where the real part of $\tilde{g}(\hbar\omega)$ is the optical power gain as the one given in Eq. (3.57) and the imaginary part is the carrier-induced phase shift [Cho94]. Using Eq. (6.2) in Eq. (6.1), we obtain

$$\tilde{\varepsilon}(\hbar\omega) = \varepsilon_{\infty}\left[1 - i\frac{c}{\omega\bar{n}}\tilde{g}(\hbar\omega)\right]. \tag{6.3}$$

Equating the real and imaginary parts of the left-hand-side (LHS) to those of the right-hand-side (RHS) with the use of the following definitions for $\tilde{\varepsilon}(\hbar\omega)$ and $\tilde{g}(\hbar\omega)$,

$$\tilde{\varepsilon}(\hbar\omega) \equiv \varepsilon_r(\hbar\omega) + i\varepsilon_i(\hbar\omega), \tag{6.4}$$

$$\tilde{g}(\hbar\omega) \equiv g(\hbar\omega) + ig_i(\hbar\omega), \tag{6.5}$$

we have

$$\begin{aligned} \varepsilon_r(\hbar\omega) &= \varepsilon_{\infty} + \frac{c\bar{n}}{\omega}g_i(\hbar\omega) \\ \varepsilon_i(\hbar\omega) &= -\frac{c\bar{n}}{\omega}g(\hbar\omega) \end{aligned}, \tag{6.6}$$

where the relation $\varepsilon_{\infty} = \bar{n}^2$ has been used. Eq. (6.6) shows that the imaginary part of $\tilde{g}(\hbar\omega)$ gives rise to the real part of $\tilde{\varepsilon}(\hbar\omega)$ and the real part of $\tilde{g}(\hbar\omega)$ gives rise to the imaginary part of $\tilde{\varepsilon}(\hbar\omega)$.

6.2.2 Complex Refractive Index

Since the square of the complex refractive index is equal to the complex dielectric function as shown

$$\tilde{n}^2(\hbar\omega) = \tilde{\varepsilon}(\hbar\omega), \tag{6.7}$$

where

$$\tilde{n}(\hbar\omega) \equiv n_r(\hbar\omega) + in_i(\hbar\omega). \tag{6.8}$$

Using Eqs. (6.8) and (6.4) in the LHS and RHS of Eq. (6.7), respectively, and equating the real and imaginary parts on both sides, respectively, we have

$$\begin{aligned} n_r^2(\hbar\omega) - n_i^2(\hbar\omega) &= \varepsilon_r(\hbar\omega) \\ 2n_r(\hbar\omega)\,n_i(\hbar\omega) &= \varepsilon_i(\hbar\omega) \end{aligned}. \tag{6.9}$$

Solving the dual equations in Eq. (6.9) for the real refractive index $n_r(\hbar\omega)$ in terms of

$\varepsilon_r(\hbar\omega)$ and $\varepsilon_i(\hbar\omega)$, we obtain

$$n_r(\hbar\omega) = \sqrt{\varepsilon_r(\hbar\omega) + \frac{1}{2}\sqrt{\varepsilon_r^2(\hbar\omega) + \varepsilon_i^2(\hbar\omega)}} . \tag{6.10}$$

For the imaginary refractive index $n_i(\hbar\omega)$, we can also solve it from Eq. (6.9) and obtain

$$n_i(\hbar\omega) = \pm\sqrt{-\varepsilon_r(\hbar\omega) + \frac{1}{2}\sqrt{\varepsilon_r^2(\hbar\omega) + \varepsilon_i^2(\hbar\omega)}} , \tag{6.11}$$

or we can use the basic definition that relates the power gain to the imaginary refractive index as [Col95]

$$\frac{g(\hbar\omega)}{2} \equiv -k_o n_i(\hbar\omega) = -\frac{\omega}{c} n_i(\hbar\omega) , \tag{6.12}$$

where k_o is the propagation constant in vacuum. As a consequence, the choice of positive or negative root in Eq. (6.11) for $n_i(\hbar\omega)$ depends on the sign of $g(\hbar\omega)$ due to the fact that they are opposite in sign as shown in Eq. (6.12).

6.2.3 Simulation results

The procedure for calculations of the real and imaginary refractive indices as a function of photon energy, which are $n_r(\hbar\omega)$ and $n_i(\hbar\omega)$, respectively, is summarized as follows: (1) Calculate the complex function $\tilde{g}(\hbar\omega)$ by dropping the notations *Real* in Eqs. (3.1) and (3.63) for models with and without CE, respectively; (2) From $\tilde{g}(\hbar\omega)$, calculate the complex dielectric function using Eq. (6.3); (3) Calculate $n_r(\hbar\omega)$ using Eq. (6.10) and $n_i(\hbar\omega)$ using Eq. (6.11) or Eq. (6.12).

Many-body effects – CS. As shown in Fig. 4.13(a), gain spectra were calculated with inclusion of CS for the 4 nm $Cd_{0.3}Zn_{0.7}Se$ QW lasers at $N = 6.7, 7.4, 8.3, 9.2 \times 10^{18}$ cm^{-3} which are the carrier densities required to reach the laser action. At these values of N, the spectra of the real and imaginary refractive indices are calculated with CS and shown in Fig. 6.1. The real refractive indices around where the gain peaks locate, as indicated by the open circles in Fig. 6.1(a), are found to decrease when N increases. The spectra of the imaginary refractive index in Fig. 6.1(b) and the gain spectra in Fig. 4.13(a) are very alike with opposite signs to each other, as expected from Eq. (6.12).

Many-body effects – BGR. With the shift of BGR shown in Fig. 3.6, the corresponding rigidly-shifted spectra in Figs. 6.1(a) and (b) are shown in Fig. 6.2(a) and (b), respectively. Although the spectral location of peak gain shows a red shift with increasing N, the real refractive indices around gain peaks remain decreasing as N increases.

Many-body effects – CE. With inclusion of CE, in addition to CS and BGR, Figs. 6.3(a) and (b) show the spectra of $n_r(\hbar\omega)$ and $n_i(\hbar\omega)$, respectively, calculated at $N = 5.0$, 5.4, 5.7, 6.0×10^{18} cm^{-3} which are the required N values to reach laser action in this model, as discussed in section 4.3.2 and shown in Fig. 4.15. As comparing to Figs. 6.1(a) and 6.2(a), the real refractive indices in Fig. 6.3(a) are a bit higher at gain peaks and sweep over a wider range around the gain peaks. A reduction in the real refractive index at gain peak is also found with increasing N.

6.3 Beam Quality

6.3.1 Antiguiding Factor

In the former section, the changes in the real and imaginary refractive indices due to the injected carriers are shown. Since the refractive index is important in determining the mode profile in a laser structure, the change in the refractive index will affect the quality of a laser beam. Starting with a relationship between how the real and imaginary indices are affected by the carrier density, it is described using what is referred to as the antiguiding factor

$$\alpha(\hbar\omega) \equiv \frac{\dfrac{dn_r(\hbar\omega)}{dN}}{\dfrac{dn_i(\hbar\omega)}{dN}} . \tag{6.13}$$

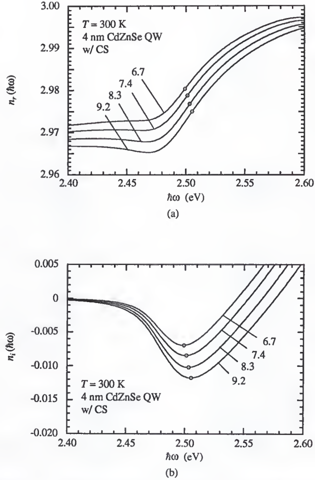

Figure 6.1 Calculated spectra of the (a) real and (b) imaginary refractive indices for the 4 nm $Cd_{0.3}Zn_{0.7}Se$ QW lasers with CS included. The open circles indicate the values of the real and/or imaginary indices at gain peaks for the carrier densities indicated by the numbers ($\times 10^{18}$ cm^{-3}).

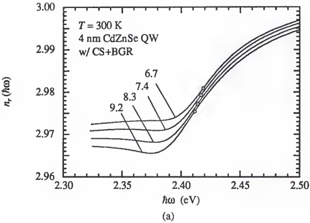

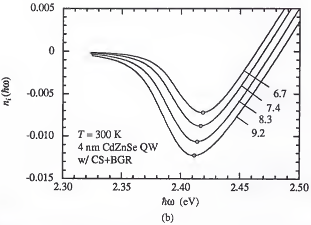

Figure 6.2 Calculated spectra of the (a) real and (b) imaginary refractive indices for the 4 nm $Cd_{0.3}Zn_{0.7}Se$ QW lasers with CS and BGR included. The open circles indicate the values of the real and/or imaginary indices at gain peaks for the carrier densities indicated by the numbers ($\times 10^{18}$ cm^{-3}).

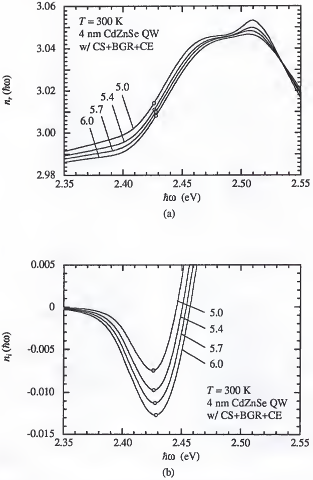

(a)

(b)

Figure 6.3 Calculated spectra of the (a) real and (b) imaginary refractive indices for the 4 nm $Cd_{0.3}Zn_{0.7}Se$ QW lasers with CS, BGR and CE included. The open circles indicate the values of the real and/or imaginary indices at gain peaks for the carrier densities indicated by the numbers ($\times 10^{18}$ cm^{-3}).

Substituting $n_i(\hbar\omega)$ with Eq. (6.12), Eq. (6.13) can be rewritten as

$$\alpha(\hbar\omega) = -\frac{2\omega}{c}\frac{\frac{dn_r(\hbar\omega)}{dN}}{\frac{dg(\hbar\omega)}{dN}} = -\frac{4\pi}{\lambda}\frac{\frac{dn_r(\hbar\omega)}{dN}}{\frac{dg(\hbar\omega)}{dN}}, \tag{6.14}$$

where the changes in optical gain and real refractive index are now combined to determine the antiguiding factor [Cho94]. The parameter $\alpha(\hbar\omega)$ is often also referred to as the linewidth enhancement factor [Kes90, Kes91, Tie92], since it is a key quantity in determining the linewidth and chirp of single mode lasers to be used for optical communications. This topic is beyond the scope of present work and left to the discussion in [Osi87]. The focus of this chapter is placed on how the antiguiding factor is related to the beam quality.

Usually, the term $dg(\hbar\omega)/dN$ in Eq. (6.14) is positive since $g(\hbar\omega)$ increases with N as shown in Figs. 4.10(a), 4.11(a) and 4.12(a) for the InGaAs QW lasers and Figs. 4.13(a), 4.14(a) and 4.15(a) for the CdZnSe QW lasers. If the real refractive index decreases with increasing N, then $dn_r(\hbar\omega)/dN$ is negative which results in a positive value for $\alpha(\hbar\omega)$. From the spectra of $n_r(\hbar\omega)$ shown in Figs. 6.1(a), 6.2(a) and 6.3(a), values of $n_r(\hbar\omega)$ around gain peaks decrease with increasing N in the QW. As a consequence, the spectra of $\alpha(\hbar\omega)$ shown in Figs. 6.4(a), (b) and (c) for all three models have positive antiguiding factors at where gain exists. The calculation with CE included still shows positive antiguiding factors for the CdZnSe QW lasers like what have been observed and predicted in the GaAs-based lasers [Hen80, Hen81, Kes90, Kes91]. However, this calculation result is opposite to the previous prediction where the strong Coulomb enhancement in the CdZnSe QW lasers results in negative values for the antiguiding factor around gain peaks [Cho95b]. A negative antiguiding factor means that the real refractive index increases with the carrier density according Eq. (6.14).

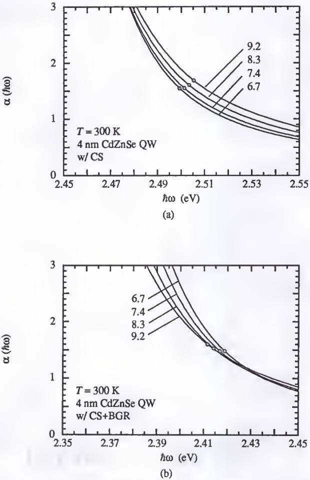

(a)

(b)

Figure 6.4 Calculated spectra of the antiguiding factor for the 4 nm $Cd_{0.3}Zn_{0.7}Se$ QW lasers (a) with CS, (b) with CS and BGR, and (c) with CS, BGR and CE included. The open circles indicate the values of antiguiding factors at gain peaks for the carrier densities indicated by the numbers ($\times 10^{18}$ cm^{-3}).

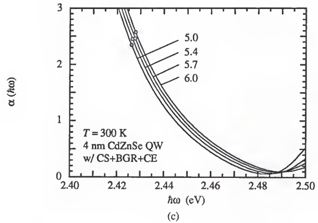

Figure 6.4 -- continued.

6.3.2 A Qualitative Description

In this section, a qualitative description will be given on how the antiguiding factor, which is associated with the carrier-induced refractive index change discussed earlier, has important implications for the laser beam quality. For mathematical models on this subject, we leave them to the literatures [Coo75, Kir77, Nas73].

Fig. 6.5(a) is a simplified cross-section sketch of a stripe-geometry gain-guided QW laser with a stripe width of w, where x-direction is the lateral direction, y-direction is along the axis of the stripe and z-direction is the growth direction (normal to the plane of QW). In the QW layer, the region beneath the stripe is defined here as the "pumped section" and the "unpumped section" is referred to as the region on the either side of the pumped section. Assuming that current spreading can be neglected, injection current is then confined to the pumped section and the lateral current profile is sketched in Fig. 6.5(b). Below threshold, the injection current creates a lateral carrier density profile, as shown in Fig. 6.5(c), where the injected carrier density $N < N_{th}$ only exists in the pumped section when lateral carrier diffusion is ignored. The injected carriers go into spontaneous emission since the stimulated emission is negligible below threshold. If the antiguiding factor is positive, the real refractive index will have an inverse profile of the carrier density profile. As a consequence, the real refractive index is lower beneath the stripe than the edges producing a so-called carrier-induced antiguiding effect, as shown in Fig. 6.5(d). This antiguiding effect has been observed leading to worse lateral beam confinements and higher threshold currents in narrow-stripe gain-guided InGaAs QW lasers [Bee91, Shi89] than in their ridge-guided counterparts [Off89]. Fig. 6.5(e) shows that if the antiguiding factor is negative, which is very unusual, the real refractive index in the pumped section is higher than those in the unpumped sections on both sides, resulting in a better lateral beam confinement for narrow-stripe lasers.

Above threshold, that is $I > I_{th}$, a narrow-stripe laser ($w < 10$ μm) typically lases in a fundamental lateral mode where the optical intensity distribution (lateral near-field pattern) of the stimulated emission fills the entire width of the pumped section, as illustrated in Fig. 6.6(a). For the purpose of this qualitative explanation, the cosine-form of intensity profile is replaced by a rectangular profile. Since all extra carriers above N_{th} go into stimulated emission, carrier density in the pumped section is clamped at N_{th}, as shown in Fig. 6.6(b). Again, if the antiguiding factor is positive, the real refractive index profile in Fig. 6.6(c) will have a lower value in the pumped section than in the either side and the optical field will experience a carrier-induced antiguiding effect, in addition to the gain-guiding mechanism provided by the gain generated along the axis of the stripe. Much of the light will be absorbed in the lossy unpumped sections. If the antiguiding factor is negative, the beam will have a better lateral confinement due to the convex real index profile in Fig. 6.6(d).

For wide-stripe gain-guided lasers ($w > 20\ \mu\text{m}$), as the current increases above threshold, they usually will lase in higher order lateral mode, which has more than one peak in the lateral optical intensity profile as illustrated in Fig. 6.7(a). Each peak corresponding a lasing filament and the total width of lasing filaments are less than the stipe width. The carrier density is clamped at N_{th} inside a lasing filament and continues to rise above N_{th} on the either side of the filament. This phenomenon is referred to as spatial hole burning and illustrated in Fig. 6.7(b) based on the assumptions of the rectangular intensity profile and no lateral carrier diffusion. In the case of the positive antiguiding factor, as shown in Fig. 6.7(c), the real refractive index variation is inverse to the carrier density variation. Therefore, the real index inside the filament is higher than that in the either side of the filament, which forms a self-focusing carrier-induced index waveguide. As a consequence, the size of the self-focused filament will be very small ($< 5\ \mu\text{m}$) [Kir77]. If the antiguiding factor is negative, the real refractive index variation follows the variation of the carrier density, as shown in Fig. 6.7(d), which produces an antiguiding effect for the filaments and suppresses filamentary lasing to achieve a better beam quality.

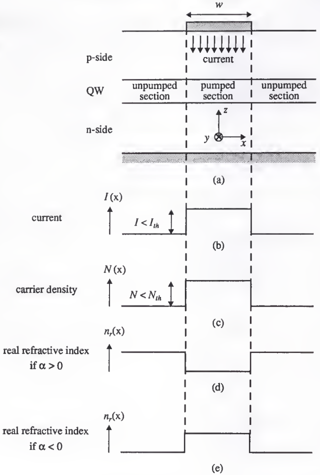

Figure 6.5 Below threshold, effect of carrier-induced real refractive index change illustrated by (a) cross-section sketch of a gain-guided stripe-geometry QW laser and sketched lateral profiles of (b) current; (c) carrier-density; (d) real refractive index when the antiguiding factor $\alpha > 0$; (e) real refractive index when $\alpha < 0$.

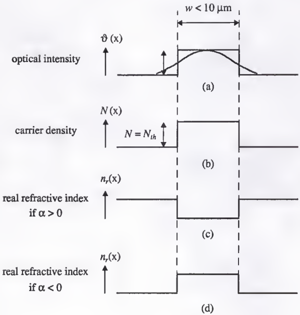

Figure 6.6 Above threshold, effect of carrier-induced real refractive index change in narrow-stripe gain-guided QW lasers illustrated by the sketched lateral profiles of (a) optical intensity; (b) carrier density; (c) real refractive index when the antiguiding factor $\alpha > 0$; (d) real refractive index when $\alpha < 0$.

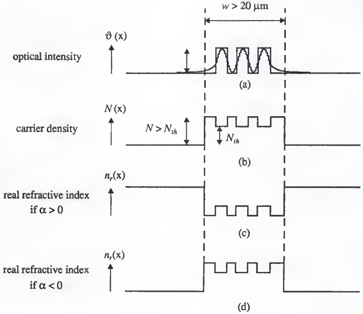

Figure 6.7 Above threshold, effect of carrier-induced real refractive index change in wide-stripe gain-guided QW lasers illustrated by the sketched lateral profiles of (a) optical intensity; (b) carrier density; (c) real refractive index when the antiguiding factor $\alpha > 0$; (d) real refractive index when $\alpha < 0$.

6.4 Near-Field Measurement

One important measurement indicating the quality of a laser beam is measuring its optical intensity distribution at the laser facet (sketched as an oval shape in Fig. 4.19), which is usually referred to as the near-field measurement. In this work, near-field patterns at various injection levels are measured using two configuration types of CdZnSe QW lasers fabricated from the same wafer with an epitaxial structure as sketched in Fig. 2. 2. One type is the narrow-stripe buried-ridge index-guided lasers with a stripe width $w = 5$ µm and a cavity length $L = 1219$ µm, as depicted in Fig. 4.2, and the other type is the wide-stripe gain-guided lasers with $w = 20$ µm and $L = 1300$ µm, as shown in Fig. 6.8 with a sketch of a near-field pattern. Both types of lasers were characterized in bar forms using current pulses at room temperature. Fig. 6.9 illustrates the experimental setup of the near-field measurement. The near-field pattern at the laser facet was imaged onto the paper screen using a 50X microscope objective. The image on the paper screen was captured by the Hamamatsu C2400 CCD camera and monitored on a TV screen. The image of the measured near-field pattern was also sent to a Pentium 120 MHz PC equipped with a viewgraber interface for image processing and data analysis using the software HLImage^{++}.

Fig. 6.10 shows plots of measured lateral near-field intensity profiles for the 20 µm wide-stripe gain-guided CdZnSe QW laser with $I_{th} = 150$ mA. At $I = 250$ mA, several bright spots are found along the lateral direction in the near-field pattern which clearly show up as several sharp peaks in the analyzed lateral near-field intensity profile. This filamentary lasing phenomenon in the wide-stripe gain-guided lasers indicates that, as discussed in Section 6.3.2 and illustrated in Fig. 6.7, CdZnSe QW lasers have positive antiguiding factors at lasing energies. This agrees with the calculation results shown in Fig. 6.4 and thus invalidates a previous prediction that CdZnSe QW lasers should have negative antiguiding factors at where optical gain exists due the strong Coulomb attraction effect [Cho94]. In a comparison with the wide-stripe gain-guided lasers, near-field patterns for the 5 µm nar-

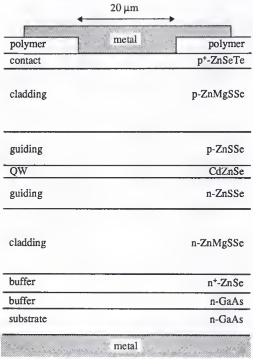

Figure 6.8 Cross-section sketch of the 20 μm wide gain-guided CdZnSe/ZnSSe SCH single QW laser devices provided by the 3M Company.

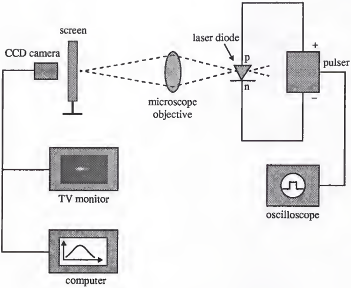

Figure 6.9 Illustration of experimental setup for measuring the near-field pattern of CdZnSe QW diode lasers. The near-field pattern at the laser facet was imaged to a paper screen using a microscope objective. The image was captured by a CCD camera and displayed on a TV monitor. The image was then analyzed using the software HLImage^{++} in a computer.

row-stripe buried-ridge index-guided CdZnSe QW laser with $I_{th} = 25$ mA were also measured at various injection currents. The analyzed lateral near-field intensity profiles, as shown in Fig. 6.11(b), show smooth single-lobe fundamental mode profiles with no sign of filamentary lasing due to the built-in lateral index waveguide of the buried-ridge structure.

6.5 Summary

Complex refractive index as a function of photon energy was derived from the complex optical susceptibility using the EHP theory with various many-body effects included. Spectra of real and imaginary refractive indices were calculated for the CdZnSe QW structure at various carrier densities. It was found that the real refractive indices around gain peaks decrease with increasing carrier density. As a consequence, the associated antiguiding factors were found having positive values at gain peaks for the CdZnSe QW structure, even when the significant Coulomb enhancement was taken into account in the calculation. This result was opposite to a previous work where negative antiguiding factors at gain peaks were predicted for the CdZnSe QW structure [Cho94]. The filamentary lasing phenomenon observed in the measured near-field pattern for the wide-stripe gain-guided CdZnSe QW laser indicated agreement with our prediction that CdZnSe QW lasers should have positive antiguiding factors at lasing energies.

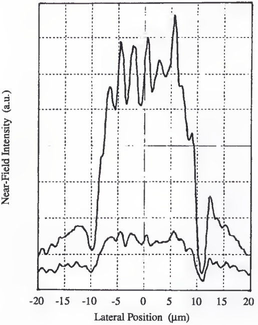

Figure 6.10 Analyzed lateral intensity profiles of the measured near-field patterns for the 20 μm wide gain-guided CdZnSe QW lasers with $I_{th} = 150$ mA at $I = 50$ and 250 mA.

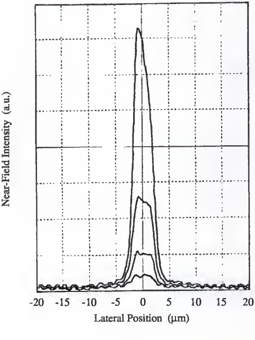

Figure 6.11 Analyzed lateral intensity profiles of the measured near-field patterns for the 5 μm wide buried-ridge index-guided CdZnSe QW lasers with I_{th} = 25 mA at I = 10, 20, 30 and 40 mA.

CHAPTER 7
CONCLUSIONS AND FUTURE WORKS

7.1 Conclusions

Effects of Coulomb attraction between injected electrons and holes in semiconductor quantum well lasers were studied. The investigation was based on a realistic model presented in Chapter 2 and 3, which was developed from the conventional electron-hole plasma theory [Col95, Cor93], modified by many-body effects [Asa93, Cho94, Hau90], generalized for the multi-subband system and incorporated with the effective-mass anisotropy due to the biaxial strain in the quantum well. Numerical calculations showed that Coulomb attraction enhances the optical gain and spontaneous emission in quantum well laser structures. This so-called Coulomb enhancement was found to be stronger in blue-green CdZnSe QW lasers than in infrared InGaAs QW lasers.

With inclusion of Coulomb enhancement, the spectral location of peak gain was found to shift to higher energy with increasing injected carrier density in either InGaAs or CdZnSe QW laser structures. The importance of Coulomb enhancement on predicting the carrier-induced energy shift in peak gain location was justified by good agreement found between the measured (see Figs. 4.5 and 4.8) and predicted (see Figs. 4.12 and 4.15) increases in lasing energy with decreasing cavity length (increasing carrier density). For InGaAs QW lasers, the inclusion of Coulomb enhancement in the prediction [Hsu97a] has solved a problem raised in previous studies on GaAs-based QW lasers [Che93, Chi88] that the ignorance of Coulomb enhancement had yielded essentially a constant spectral location of peak gain with increasing carrier density. This is due to the fact that the bandgap renormalization red shift and band filling blue shift offset each other in GaAs-based QW lasers (see Fig. 4.6). For CdZnSe QW lasers, our study [Hsu97b] has proved a previous prediction to be incorrect [Cho95b] which showed a red shift in the peak gain energy with increasing carrier density.

In studying the temperature dependence of lasing energy using CdZnSe QW lasers, good agreement was found between the prediction with Coulomb enhancement and experimental data at temperature ranging from 160 K to 300 K (see Fig. 4.30). This has demonstrated that electron-hole plasma is responsible for lasing action in CdZnSe QW lasers at room temperature down to 160 K. Below 160 K, excitons may play a more important role in lasing mechanism for CdZnSe QW lasers.

Gain versus radiative current density (g-J_{rad}) relationship was calculated for both InGaAs and CdZnSe QW lasers (see Fig. 4.21 and 4.22). With inclusion of Coulomb enhancement, the calculated g-J_{rad} curves were found to have higher transparencies and higher slopes than the ones predicted without Coulomb enhancement included. Using these g-J_{rad} curves, the predicted threshold currents for both InGaAs and CdZnSe QW lasers with Coulomb enhancement included (see Figs. 4.25 and 4.26) were found to give good agreement with the measured threshold currents at various cavity lengths (see Figs. 4.17 and 4.18). The predictions without Coulomb enhancement were found to overestimate the threshold currents. This study has corrected a previous work on the calculation of gain-current characteristics in CdZnSe QW structures including many body effects [Ree95a] where the predicted threshold currents were much too high comparing to our measured data.

For CdZnSe QW laser structure, Coulomb attraction effects were shown to not only increase the peak gain but also enhance the absorption steps to resonance-like absorption peaks (see Fig. 5.5). The experimentally observed absorption peaks in CdZnSe QW lasers at room temperature (see Fig. 5.4), which were mistakenly attributed to exciton absorption resonances [Din94], were thus successfully predicted for the first time by using the electron-hole plasma theory with Coulomb attraction and other many-body effects taken into account.

Spectra of complex refractive index were calculated including many-body effects for the CdZnSe QW laser structure at various carrier densities (see Figs. 6.1, 6.2 and 6.3). The real refractive indices around gain peaks were found to reduce with increasing carrier density in the QW, even when Coulomb enhancement was included. The resulting positive antiguiding factors (see Fig. 6.4) disagreed with the negative antiguiding factors predicted for CdZnSe QW lasers in a previous work [Cho95b]. However, the filamentary lasing phenomenon observed in the 20 µm wide gain-guided CdZnSe QW laser (see Fig. 6.10) implied that CdZnSe QW lasers should have positive antiguiding factors at gain peaks.

In conclusion, Coulomb attraction effects are very important in semiconductor quantum well lasers, especially in wide-band gap laser materials with small dielectric constants such as CdZnSe QW lasers. At room temperature, recombinations of electron-hole plasma are responsible for lasing action in CdZnSe QW lasers, not excitons. The theory with Coulomb enhancement works well in CdZnSe QW lasers down to 160 K. As reducing the temperature below 160 K, excitons may become more important.

7.2 Future Works

Several related future works are suggested as follows:

1. Theoretical models developed in this work can be applied to other material systems and utilized for optimization of laser devices. Recently there has been a considerable expansion of research activities on III-V GaN-based laser materials. This expansion is attributed to the commercialization of high-brightness III-V GaN-based blue-green LEDs by Nichia Chemical Industries and the first demonstration of blue lasing emission from laser diodes fabricated from this material system [Nak96]. Several theoretical studies based on the theory including many-body effects have shown that Coulomb attraction effects are strong in these GaN-based laser structures [Cho95c, Ree95b]. However, many unrealistic

assumptions were made in these works due to lack of many parameters for the hexagonal GaN-based materials. In addition, similar works done for the zinc-blend CdZnSe material system by the same research groups [Cho95b, Ree95a] were shown in this dissertation to conflict with experimental measurements. It will be interesting to simulate GaN-based QW lasers using our Coulomb enhancement model developed in this work, once the parameters for GaN-based materials become available in the future.

2. The Coulomb enhancement model developed in this dissertation reaches its limit for carrier density much lower than the Mott density. This short coming is mainly due to the fact that the Padé approximation, made in deriving the Coulomb enhancement factor, is an approximation for carrier densities higher than the Mott density. If this limitation can be removed, then the absorption and refractive index spectra in the unpumped section of a laser device can be calculated. This may be beneficial to the understanding and designing of laser devices which utilize index modulation between the pumped and unpumped sections such as antiguiding array laser devices.

3. In the recent years, a new type of semiconductor lasers, which utilizes transitions between subbands in the conduction band quantum wells, is under fast development [Fai94, Fai95, Hsu97c]. In such so-called intersubband laser devices, photons are generated from electrons making transitions from a higher subband to a lower subband in the conduction band, as shown in Fig. 7.1, which is unlike the conventional interband QW lasers discussed in this work that photons are generated from recombinations of conduction band electrons and valence band holes. Since electrons are the only type of carriers participating in the photon emission process in intersubband lasers, Coulomb attraction effects are not expected to be important. But other many-body effects, such as carrier scattering with phonons and carrier screening, still need to be investigated to improve the design of intersubband lasers.

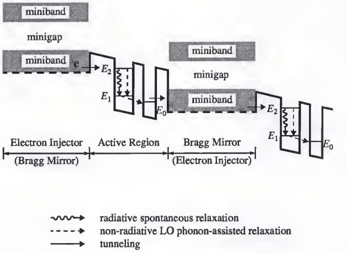

Figure 7.1 Conduction band energy diagram of a portion of the waveguide core region of a vertical transition quantum cascade laser [Fai95] under a threshold forward bias electric field.

APPENDIX A
MATERIAL PARAMETERS II-VI TERNARIES

A.1 Interpolation Method

The interpolation scheme is known to be a useful tool for estimating some physical parameters of semiconductor compounds. If one uses the linear interpolation scheme, the material parameter P of the ternary alloy $A_xB_{1-x}C$ can be derived from those of its relevant binaries AC and BC using

$$P_{A_xB_{1-x}C} = xP_{AC} + (1-x)P_{BC}, \tag{A.1}$$

where x is the mole fraction of the composition A and the subscripts indicate the materials of interest. Some material parameters, however, are shown in the experiments to deviate from the linear relation of Eq. (A.1) and have an approximately quadratic dependence on the mole fraction x as

$$P_{A_xB_{1-x}C} = xP_{AC} + (1-x)P_{BC} - b_o x(1-x), \tag{A.2}$$

where b_o is referred to as the bowing parameter. For the $Cd_xZn_{1-x}Se$ and ZnS_xSe_{1-x} ternaries, the material parameters such as the lattice constant a_c, electron effective mass m_c, elastic moduli C_{11} and C_{12}, spin-orbit splitting energy Δ, static dielectric constant ε_s, background refractive index $\bar{n}$ are assumed to vary linearly with the mole fraction x and, therefore, Eq. (A.1) is used to estimate these parameters. On the other hand, the parameters such the bulk bandgap E_g are obtained using Eq. (A.2). Some other ternary parameters are available in the literatures such as the Luttinger parameters γ_1 and γ_2 in [Wu94b], hydrostatic deformation potential a and shear deformation potential b in [Cai 95].

A.2 Binary Parameters

The material parameters for the relevant II-VI binary alloys used to estimate the II-VI ternary CdZnSe and ZnSSe alloys are listed in Table A.1 [Mad87, Mad92]. The temperature dependence of some parameters which are available in the literatures such as E_g are also listed.

A.3 Ternary Parameters

In this section, the material parameters of CdZnSe and ZnSSe ternary alloys, either estimated using the interpolation scheme of the binary parameters listed in Table A.1 or quoted from the literatures, are summarized.

1. Lattice constant. Using the lattice constants a_o of CdSe and ZnSe listed in Table A.1 in Eq. (A.1), a_o of $Cd_xZn_{1-x}Se$ is obtained

$$a_o(\mathrm{Cd}_x\mathrm{Zn}_{1-x}\mathrm{Se}) = 5.6676 + 0.3844x \ \ (\text{Å}). \tag{A.3}$$

2. Bulk bandgap. The bowing parameters b_o for bulk bandgaps E_g of CdZnSe and ZnSSe ternaries are 0.22 and 0.49 eV, respectively [Cai95]. Plugging these values for b_o and the values for E_g and dE_g/dT of CdSe, ZnSe and ZnSe binaries into Eq. (A.2), we obtain the temperature dependence of E_g for $Cd_xZn_{1-x}Se$ and ZnS_xSe_{1-x} ternaries as

$$E_g(\mathrm{Cd}_x\mathrm{Zn}_{1-x}\mathrm{Se}) = \begin{array}{l} 2.698 - 1.149x + 0.22x^2 \\ -(4.5 - 0.97x) \times 10^{-4}(T - 300) \end{array} \ (\mathrm{eV}), \tag{A.4}$$

$$E_g(\mathrm{ZnS}_x\mathrm{Se}_{1-x}) = \begin{array}{l} 2.698 + 0.49x + 0.49x^2 \\ -(4.5 + 0.2x) \times 10^{-4}(T - 300) \end{array} \ (\mathrm{eV}). \tag{A.5}$$

where T is temperature in K.

3. Spin-orbit splitting energy. The spin-orbit splitting energy Δ for $Cd_xZn_{1-x}Se$ is derived using Eq. (A.1) with values of Δ for CdSe and ZnSe in Table A.1 and given by

Parameters	CdSe	ZnSe	ZnS
lattice constant a_o (Å)	6.052	5.6676	
bulk bandgap E_g (eV)	1.771 at 293 K	2.7 at 295 K	3.68 at 295 K
temperature dependence of bulk bandgap dE_g/dT ($\times 10^{-4}$ eV/K)	-3.53	-4.5	-4.7
spin-orbit splitting energy Δ (eV)	0.416	0.4	
electron effective mass m_c ($\times m_o$)	0.112	0.150	0.184
elastic moduli C_{11} ($\times 10^{10}$ N/m^2)	6.13	9.00	
elastic moduli C_{12} ($\times 10^{10}$ N/m^2)	4.96	5.43	
static dielectric constant ε_s	10.16	$8.8+1.5\times 10^{-4}T$	
background refractive index $\bar{n}$	3.416	2.746	

Table A.1 List of material parameters for II-VI binary alloys CdSe, ZnSe and ZnS.

$$\Delta(\mathrm{Cd}_x\mathrm{Zn}_{1-x}\mathrm{Se}) = 0.4 + 0.016x \quad (\mathrm{eV}). \tag{A.6}$$

4. Electron effective mass. The electron effective mass m_c for ternaries $Cd_xZn_{1-x}Se$ and ZnS_xSe_{1-x} are estimated using Eq. (A.1) with values of m_c for CdSe, ZnSe and ZnS

$$\begin{aligned} m_c(\mathrm{Cd}_x\mathrm{Zn}_{1-x}\mathrm{Se}) &= 0.15 - 0.038x \\ m_c(\mathrm{ZnS}_x\mathrm{Se}_{1-x}) &= 0.15 + 0.034x \end{aligned} , \tag{A.7}$$

where m_c is in the unit of electron rest mass m_o.

5. Luttinger parameters. The Luttinger parameters γ_1 and γ_2 for $Cd_xZn_{1-x}Se$ and ZnS_xSe_{1-x} are given by [Wu94b]

$$\begin{aligned} \gamma_1(\mathrm{Cd}_x\mathrm{Zn}_{1-x}\mathrm{Se}) &= 4.3 + 0.65x \\ \gamma_2(\mathrm{Cd}_x\mathrm{Zn}_{1-x}\mathrm{Se}) &= 1.14. + 0.22x \\ \gamma_1(\mathrm{ZnS}_x\mathrm{Se}_{1-x}) &= 4.3 \\ \gamma_2(\mathrm{ZnS}_x\mathrm{Se}_{1-x}) &= 1.14 \end{aligned} , \tag{A.8}$$

where γ_1 and γ_2 are in the units of $\hbar^2/(2m_o)$. Since values of γ_1 and γ_2 for ZnS are not available in the literatures, values of γ_1 and γ_2 for ZnSe are used for ZnS_xSe_{1-x} which is reasonable in the case of $ZnS_{0.06}Se_{0.94}$ where $x = 0.06$.

6. Elastic moduli. The elastic moduli C_{11} and C_{12} for $Cd_xZn_{1-x}Se$ are derived using Eq. (A.1) with values of C_{11} and C_{12} for CdSe and ZnSe in Table A.1 and given by

$$\begin{aligned} C_{11}(\mathrm{Cd}_x\mathrm{Zn}_{1-x}\mathrm{Se}) &= (9 - 2.87x) \times 10^{10} \\ C_{12}(\mathrm{Cd}_x\mathrm{Zn}_{1-x}\mathrm{Se}) &= (5.34 - 0.38x) \times 10^{10} \end{aligned} \quad (\mathrm{N/m^2}). \tag{A.9}$$

7. Static dielectric constant. The temperature dependence of static dielectric constant ε_s for $Cd_xZn_{1-x}Se$ is derived using Eq. (A.1) with values of ε_s for CdSe and ZnSe in Table A.1 and given by

$$\varepsilon_s(\mathrm{Cd}_x\mathrm{Zn}_{1-x}\mathrm{Se}) = 8.8 + 1.36x + 1.5 \times 10^{-3}(1-x)T. \tag{A.10}$$

8. Background refractive index. Plugging the background refractive indices $\bar{n}$ of CdSe and ZnSe listed in Table A.1 into Eq. (A.1), $\bar{n}$ of $Cd_xZn_{1-x}Se$ is obtained

$$\bar{n}\,(\mathrm{Cd}_x\mathrm{Zn}_{1-x}\mathrm{Se}) = 2.746 + 0.67x. \qquad \text{(A.11)}$$

9. Deformation potential. The hydrostatic and shear components of the deformation potential for $Cd_xZn_{1-x}Se$ are given by $a = -5.04$ eV and $b = -1.12$ eV, respectively [Cai95].

APPENDIX B
TRANSITION MATRIX ELEMENT

B.1 Polarization-Dependent Effects

From Eqs. (57a-c) in [Cor93], the polarization-dependent of the transition matrix elements for C-HH and C-LH transitions are given by

$$\frac{|M_T|^2}{|M|^2} = \begin{cases} 1-|\hat{\mathbf{k}}\cdot\hat{\mathbf{e}}|^2 & \text{for C-HH transition} \\ \frac{1}{3}+|\hat{\mathbf{k}}\cdot\hat{\mathbf{e}}|^2 & \text{for C-LH transition} \end{cases}, \tag{B.1}$$

where $\hat{\mathbf{k}}$ is a unit vector directed along the electron wavevector $\mathbf{k}$ and $\hat{\mathbf{e}}$ is the unit polarization vector. Fig. B.1(a) and (b) show plots of $\hat{\mathbf{k}}$ and $\hat{\mathbf{e}}$ in the three-dimensional (3D) rectangular coordinates and, therefore, $\hat{\mathbf{k}}$ and $\hat{\mathbf{e}}$ can be expressed as

$$\hat{\mathbf{k}} = \sin\theta\cos\varphi\hat{\mathbf{x}} + \sin\theta\sin\varphi\hat{\mathbf{y}} + \cos\theta\hat{\mathbf{z}}, \tag{B.2}$$

$$\hat{\mathbf{e}} = \sin\theta'\cos\varphi'\hat{\mathbf{x}} + \sin\theta'\sin\varphi'\hat{\mathbf{y}} + \cos\theta'\hat{\mathbf{z}}. \tag{B.3}$$

where $\hat{\mathbf{x}}$ and $\hat{\mathbf{y}}$ are chosen as the unit vectors in the in-plane directions (in the plane of the QW), $\hat{\mathbf{z}}$ is chosen as the unit vector in the growth direction (normal to the plane of the QW), θ and θ' are angles measured from the z-axis while φ and φ' are angles measured from the x-axis. Using Eqs. (B.2) and (B.3), we obtain

$$\begin{aligned} |\hat{\mathbf{k}}\cdot\hat{\mathbf{e}}|^2 &= (\sin\theta\cos\varphi\sin\theta'\cos\varphi' + \sin\theta\sin\varphi\sin\theta'\sin\varphi' + \cos\theta\cos\theta')^2 \\ &= \sin^2\theta\cos^2\varphi\sin^2\theta'\cos^2\varphi' \\ &\quad + \sin^2\theta\sin^2\varphi\sin^2\theta'\sin^2\varphi' \\ &\quad + \cos^2\theta\cos^2\theta' \\ &\quad + 2\sin^2\theta\sin\varphi\cos\varphi\sin^2\theta'\sin\varphi'\cos\varphi' \\ &\quad + 2\sin\theta\cos\theta\sin\varphi\sin\theta'\cos\theta'\sin\varphi' \\ &\quad + 2\sin\theta\cos\theta\cos\varphi\sin\theta'\cos\theta'\cos\varphi' \end{aligned} \quad . \tag{B.4}$$

Since photons of a given polarization interact with electrons of **k** vectors pointing in different directions, $|\hat{\mathbf{k}} \cdot \hat{\mathbf{e}}|^2$ in Eq. (B.4) needs be averaged over these interactions by a proper average over **k** vector. Fig. B.1(c) shows a plot of **k** in the 3D rectangular coordinates where $k_{j\perp}$ and $k_{\parallel}$ are the components of **k** vector in the growth and in-plane directions. The j subscript indicates the jth quantized subband since electrons are quantized in the growth direction ($\hat{\mathbf{z}}$ direction). For electrons in a given subband, $k_{j\perp}$ is calculated from the associated quantized energy level using Eq. (3.9). At the subband edge, $k_{\parallel} = 0$ and $\theta_j = 0$. As moving away from the subband edge, **k** vector with a given $k_{\parallel}$ sweeps over a cone angle of $2\theta_j$ with respect to the z-axis. As a consequence, we average Eq. (B.4) over φ from 0 to 2π to obtain

$$\begin{aligned} |\hat{\mathbf{k}} \cdot \hat{\mathbf{e}}|^2 = {} & \frac{1}{2}\sin^2\theta_j \sin^2\theta' \cos^2\varphi' \\ & + \frac{1}{2}\sin^2\theta_j \sin^2\theta' \sin^2\varphi' \\ & + \cos^2\theta_j \cos^2\theta' \\ & + 0 \\ & + 0 \\ & + 0 \end{aligned} \quad , \tag{B.5}$$

where θ is replaced with θ_j indicating the jth subband transition pair. For a TE polarization, $\hat{\mathbf{e}} = \hat{\mathbf{x}}$ or $\hat{\mathbf{y}}$ and therefore plugging $\theta' = \frac{\pi}{2}$ and $\varphi' = 0$ or $\frac{\pi}{2}$ in Eq. (B.5), we have

$$|\hat{\mathbf{k}} \cdot \hat{\mathbf{e}}|^2 = \frac{1}{2}\sin^2\theta_j = \frac{1}{2} - \frac{1}{2}\cos^2\theta_j \qquad \text{for TE polarization.} \tag{B.6}$$

For a TM polarization, $\hat{\mathbf{e}} = \hat{\mathbf{z}}$ and therefore plugging $\theta' = 0$ in Eq. (B.5), we have

$$|\hat{\mathbf{k}} \cdot \hat{\mathbf{e}}|^2 = \cos^2\theta_j \qquad \text{for TM polarization.} \tag{B.7}$$

For spontaneous emission, $\hat{\mathbf{e}}$ is arbitrarily polarized. In that case, we need to average Eq. (B.5) over θ' from 0 to $\pi/2$ and φ' from 0 to 2π in spherical coordinates and the result is given by

$$|\hat{\mathbf{k}} \cdot \hat{\mathbf{e}}|^2 = \frac{1}{3} \qquad \text{for averaged polarization} \tag{B.8}$$

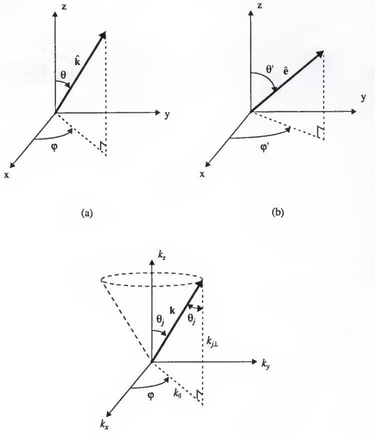

(a)

(b)

(c)

Figure B.1 The three dimensional plots of various vectors in the rectangular coordinates. (a) the unit vector $\hat{\mathbf{k}}$ directed along the electron wavevector **k**; (b) the unit polarization vector $\hat{\mathbf{e}}$; and (c) the electron wavevector **k**.

Using Eqs. (B.6) and (B.7) in Eq. (B.1), the transition matrix elements $|M_T|^2$ for the optical gain with TE and/or TM polarizations can be expressed as a function of θ_j

$$\frac{|M_T|^2}{|M|^2} = \begin{cases} \frac{1}{2}+\frac{1}{2}\cos^2\theta_j & \text{for C-HH TE gain} \\ 1-\cos^2\theta_j & \text{for C-HH TM gain} \\ \frac{5}{6}-\frac{1}{2}\cos^2\theta_j & \text{for C-LH TE gain} \\ \frac{1}{3}+\cos^2\theta_j & \text{for C-LH TM gain} \end{cases} . \tag{B.9}$$

Using Eq. (B.8) in Eq. (B.1), the average transition matrix $|\overline{M}_T|^2$ for the spontaneous emission can be also be expressed as a function of θ_j

$$\frac{|\overline{M}_T|^2}{|M|^2} = \frac{2}{3} \quad \text{for both C-HH and C-LH spontaneous emission}. \tag{B.10}$$

Eqs. (2.27) and (2.32) are therefore given as Eqs. (B.9) and (B.10), respectively.

B.2 Angle-Dependent Effects

In the former section, we have derived the expression for $|M_T|^2$ as a function of θ_j without knowing how to calculate θ_j. From Fig. B.1(c), we use the definition of the cosine function of angle θ_j for a right triangle to obtain

$$\cos^2\theta_j = \frac{k_{j\perp}^2}{k_\parallel^2 + k_{j\perp}^2}. \tag{B.11}$$

Multiplying both the denominator and numeration at the right-hand side (RHS) of Eq. (B.11) by $\hbar^2/(2m_{rj\parallel})$, it becomes

$$\cos^2\theta_j = \frac{\dfrac{\hbar^2 k_{j\perp}^2}{2m_{rj\parallel}}}{\dfrac{\hbar^2 k_\parallel^2}{2m_{rj\parallel}} + \dfrac{\hbar^2 k_{j\perp}^2}{2m_{rj\parallel}}}, \tag{B.12}$$

where $m_{rj\parallel}$ is the in-plane reduced effective mass for the jth subband transition pair defined in Eq. (2.31). Recalling Eqs. (2.21) and (2.22), the transition energy E_{cv} can be rewritten as

$$\begin{aligned} E_{cv} &= E_g + E_{cj} + \frac{\hbar^2 k_{\parallel}^2}{2m_{cj\parallel}} + E_{vj} + \frac{\hbar^2 k_{\parallel}^2}{2m_{vj\parallel}}, \\ &= E_g + E_{cj} + E_{vj} + \frac{\hbar^2 k_{\parallel}^2}{2m_{rj\parallel}} \end{aligned} \tag{B.13}$$

where definition for $m_{rj\parallel}$ in Eq. (2.31) is used in the last expression for Eq. (B.13). Rearranging Eq. (B.13), we obtain

$$\frac{\hbar^2 k_{\parallel}^2}{2m_{rj\parallel}} = E_{cv} - E_g - E_{cj} - E_{vj}. \tag{B.14}$$

Recalling the relationship between the jth quantized energy level E_{nj} and the associated equivalent growth-direction wavevector $k_{nj\perp}$ from Eq. (3.11), the summation of the jth quantized energies in the CB and VB are given by

$$E_{cj} + E_{vj} = \frac{\hbar^2 k_{cj\perp}^2}{2m_{cj\perp}} + \frac{\hbar^2 k_{vj\perp}^2}{2m_{vj\perp}} \cong \frac{\hbar^2 k_{j\perp}^2}{2m_{rj\perp}}, \tag{B.15}$$

where the last expression is approximated under a typical case that $k_{cj\perp}$ and $k_{vj\perp}$ for the jth CB and VB subbands are approximately equal. Plugging Eq. (B.15) into the following equation, we obtain

$$\frac{\hbar^2 k_{j\perp}^2}{2m_{rj\parallel}} = \frac{\hbar^2 k_{j\perp}^2}{2m_{rj\perp}} \cdot \frac{m_{rj\perp}}{m_{rj\parallel}} = (E_{cj} + E_{vj}) \frac{m_{rj\perp}}{m_{rj\parallel}}. \tag{B.16}$$

We then use Eqs. (B.14) and (B.16) in Eq. (B.12) to obtain

$$\cos^2\theta_j = \frac{(E_{cj} + E_{vj}) \dfrac{m_{rj\perp}}{m_{rj\parallel}}}{(E_{cv} - E_g - E_{cj} - E_{vj}) + (E_{cj} + E_{vj}) \dfrac{m_{rj\perp}}{m_{rj\parallel}}}. \tag{B.17}$$

Eqs. (2.9) or (B.17) is therefore derived for the anisotropic effective-mass model described in Chapter 2. For an isotropic effective-mass model where the in-plane effective masses are equal to their growth-direction counterparts and $m_{rj\parallel} = m_{rj\perp}$, Eq. (B.17) reduces to

$$\cos^2\theta_j = \frac{E_{cj} + E_{vj}}{E_{cv} - E_g}. \tag{B.18}$$

Eq. (B.18) is usually used in the literatures [Chi88] where the anisotropy in effective masses is ignored.

REFERENCES

[Asa93] M. Asada, *Quantum Well Lasers*, P. S. Zory, Ed. New York: Academic Press, 1993, ch. 2.

[Bee91] K. J. Beernink, J. J. Alwan, and J. J. Coleman, "Antiguiding in narrow stripe gain-guided InGaAs-GaAs strained-layer lasers," *J. Appl. Phys.*, vol. 69, pp. 56-60, 1991.

[Blo96] P. Blood, P. Rees, C. Cooper and P. M. Smowton, "Critical issues in laser diode calculations," *Proceedings of SPIE*, vol. 2693, pp. 444-454, 1996.

[Cai95] Yijun Cai, "Wide-band-gap II-VI Semiconductor heterostructure modeling and device design," *Ph.D dissertation*, Oregon Graduate Institute of Science & Technology, 1995.

[Cam94] D. Campi, P. J. Bradley, R. Calvani, and R. Caponi, "Modeling of nonlinear absorption and refraction in quantum-well structures for all-optical switching," *IEEE J. Quantum Electron.*, vol. QE-29, pp. 1144-1157, 1994.

[Cas78] H. C. Casey, and M. B. Panish, *Heterostructure Lasers; Part A: Fundamental Principles*, Orlando: Academic Press, 1978.

[Che93] P. A. Chen, C. Juang, and C. Y. Chang, "Carrier-induced energy shift in GaAs/AlGaAs multiple quantum well laser diodes," *IEEE J. Quantum Electron.*, vol. QE-29, pp. 2607-2618, 1993.

[Chi88] S. R. Chinn, P. S. Zory, and A. R. Reisinger, "A model for GRIN-SCH-SQW diode lasers," *IEEE J. Quantum Electron.*, vol. QE-24, pp. 2191-2214, 1988.

[Cho94] W. W. Chow, S. W. Koch, and M. Sargent III, *Semiconductor-Laser Physics*, Berlin: Springer, 1994.

[Cho95a] W. W. Chow, S. W. Corzine, D. B. Young, and L. A. Coldren, "Many body effects in the temperature dependence of threshold in a vertical-cavity surface-emitting laser," *Appl. Phys. Lett.*, vol. 66, pp. 2460-2462, 1995.

[Cho95b] W. W. Chow, and S. W. Koch, "Many-body Coulomb effects in room-temperature II-VI quantum well semiconductor lasers," *Appl. Phys. Lett.*, vol. 66, pp. 3004-3006, 1995.

[Cho95c] W. W. Chow, A. Knorr, and S. W. Koch, "Theory of laser gain in group-III nitrides," *Appl. Phys. Lett.*, vol. 67, pp. 754-756, 1995.

[Cin96] R. Cingolani, L. Calcagnile, G. Coli, R. Rinaldi, M. Lomoscolo, M. DiDio, A. Franciosi, L. Vanzetti, G. C. LaRocca, and D. Campi, "Radiative recombination processes in wide-band-gap II-VI quantum wells: the interplay between excitons and free carriers," *J. Opt. Soc. Am. B*, vol. 13, pp. 1268-1277, 1996.

[Col95] L. A. Coldren, and S. W. Corzine, *Diode Lasers and Photonic Integrated Circuits*, New York: John Wiley & Sons, 1995.

[Coo75] D. D. Cook, and F. R. Nash, "Gain-induced guiding and astigmatic output beam of GaAs lasers," *J. Appl. Phys.*, vol. 46, pp. 1660-1672, 1975.

[Cor93] S. W. Corzine, R. H. Yan, and L. A. Coldren, *Quantum Well Lasers*, P. S. Zory, Ed. New York: Academic Press, 1993, ch. 1.

[Din92] J. Ding, H. Jeon, T. Ishihara, M. Hagerott, and A. V. Nurmikko, H. Luo, N. Samarth, and J. K. Furdyna, "Excitonic gain and laser emission in ZnSe-based quantum wells," *Phys. Rev. Lett.*, vol. 69, pp. 1707-1710, 1992.

[Din93] J. Ding, M. Hagerott, T. Ishihara, H. Jeon, and A. V. Nurmikko, "(Zn,Cd)Se/ZnSe quantum-well lasers: excitonic gain in an inhomogeneously broadened quasi-two-dimensional system," *Phys. Rev. B*, vol. 47, pp. 10528-10542, 1993.

[Din94] J. Ding, M. Hagerott, P. Kelkar, A. V. Nurmikko, D. C. Grillo, L. He, J. Han, and R. L. Gunshor, "Role of Coulomb-correlated electron-hole pairs in ZnSe-based quantum-well diode lasers," *Phys. Rev. B*, vol. 50, pp. 5787-5790, 1994.

[Fai94] J. Faist, F. Capasso, D. L. Sivco, C. Sirtori, A. L. Hutchinson, and A. Y. Cho, "Quantum cascade laser," *Science*, vol. 264, pp.553-556, 1994.

[Fai95] J. Faist, F. Capasso, C. Sirtori, D. L. Sivco, A. L. Hutchinson, and A. Y. Cho, "Vertical transition quantum cascade laser with Bragg confined excited state," *Appl. Phys. Lett.*, vol. 66, pp. 538-540, 1995.

[Fan92] Y. Fan, J. Han, L. He, J. Saraie, R. L. Gunshor, M. Hagerott, H. Jeon, A. V. Nurmikko, G. C. Hua, and N. Otsuka, "Graded band gap ohmic contact to p-ZnSe," *Appl. Phys. Lett.*, vol. 61, pp. 3160-3162, 1992.

[Gai93] J. M. Gaines, R. R. Drenten, K. W. Haberern, T. Marshall, P. Mensz, and J. Petruzzello, "Blue-green injection lasers containing pseudomorphic ZnMgSSe cladding layers and operating up to 394 K," *Appl. Phys. Lett.*, vol. 62, pp. 2462-2464, 1993.

[Gro94] M. J. Grove, D. A. Hudson, P. S. Zory, R. J. Dalby, C. M. Harding, and A. Rosenberg, "Pulsed anodic oxides for III-V semiconductor device fabrication," *J. Appl. Phys.*, vol. 76, pp. 587-589, 1994.

[Haa91] M. A. Haase, J. Qiu, J. M. DePuydt, and H. Cheng, "Blue-green laser diodes," *Appl. Phys. Lett.*, vol. 59, pp. 1272-1274, 1991.

[Haa93] M. A. Haase, P. F. Baude, M. S. Hagedorn, J. Qiu, J. M. DePuydt, H. Cheng, S. Guha, G. E. Höfler, and B. J. Wu, "Low-threshold buried-ridge II-VI laser diodes," *Appl. Phys. Lett.*, vol. 63, pp. 2315-2317, 1993.

[Hab97] K. W. Haberern, P. F. Baude, S. J. Flamholtz, M. N. Buijs, J. Horikx, K. K. Law, M. A. Haase, T. J. Miller, and G. M. Haugen, "II-VI index-guided lasers for optical recording," *Proceedings of SPIE*, vol. 3001, pp. 101-105, 1997.

[Hag92] M. Hagerott, H. Jeon, A. V. Nurmikko, W. Xie, D. C. Grillo, M. Kobayashi, and R. L. Gunshor, "Indium tin oxide as transparent electrode material for ZnSe-based blue quantum well light emitters," *Appl. Phys. Lett.*, vol. 60, pp. 2825-2827, 1992.

[Hau89] H. Haug, and S. W. Koch, "Semiconductor laser theory with many-body effects," *Phys. Rev. A*, vol. 4, pp. 1887-1898, 1989.

[Hau90] H. Haug, and S. W. Koch, *Quantum Theory of the Optical and Electronic Properties of Semiconductors*, Singapore: World Scientific, 1990.

[Hen80] C. H. Henry, R. A. Logan, and R. F. Merritt, "Measurement of gain and absorption spectra in AlGaAs buried heterostructure lasers," *J. Appl. Phys.*, vol. 51, pp. 3042-3050, 1980.

[Hen81] C. H. Henry, R. A. Logan, and K. A. Bertness, "Spectral dependence of the change in refractive index due to carrier injection in GaAs lasers," *J. Appl. Phys.*, vol. 52, pp. 4457-4461, 1981.

[Hen82] C. H. Henry, "Theory of the linewidth of semiconductor lasers," *IEEE Quantum Electron.*, vol. QE-18, pp. 259-264, 1982.

[Hsu97a] C.-F. Hsu, P. S. Zory, P. Rees, and M. A. Haase, "Coulomb enhancement in CdZnSe single quantum well lasers," *Proceedings of SPIE*, vol. 3001, pp. 106-116, 1997.

[Hsu97b] C.-F. Hsu, P. S. Zory, C. H. Wu and M. A. Emanuel, "Coulomb Enhancement in InGaAs/GaAs Quantum Well Lasers," *IEEE J. Selected Topics in Quantum Electronics on Semiconductor Lasers*, vol. 3, pp. 158-165, 1997.

[Hsu97c] C.-F. Hsu, J. S. O, P. S. Zory, and D. Botez, "Intersuband laser design using a quantum box array," *Proceedings of SPIE*, vol. 3001, pp. 271-281, 1997.

[Hu94] S. Y. Hu, D. B. Young, A. C. Gossard, and L. A. Coldren, "The effect of lateral leakage current on the experimental gain/current-density curve in quantum-well ridge-waveguide lasers," *IEEE J. Quantum Electron.*, vol. QE-30, pp. 2245-2250, 1994.

[Kes90] M. P. Kesler, and C. Harder, "Excitonic effects in gain and index in GaAlAs quantum well lasers," *Appl. Phys. Lett.*, vol. 57, pp. 123-125, 1990.

[Kes91] M. P. Kesler, and C. Harder, "Spontaneous emission and gain in GaAlAs quantum well lasers," *IEEE J. Quantum Electron.*, vol. QE-27, pp. 1812-1816, 1991.

[Kir77] P. A. Kirkby, A. R. Goodwin, G. H. B. Thomson, and P. R. Selway, "Observations of self-focusing in stripe geometry semiconductor lasers and the development of a comprehensive model of their operation," *IEEE J. Quantum Electron.*, vol. QE-13, pp. 705-719, 1977.

[Kit86] C. Kittel, *Introduction to Solid State Physics*, Singapore: John Wiley & Sons, 1986.

[Kli97] C. F. Klingshirn, *Semiconductor Optics*, Berlin: Springer, 1997.

[Lim91] G. Lim, Y. Park, C. A. Zmudzinski, P. S. Zory, L. M. Miller, T. L. Cockerill, J. J. Coleman, C. S. Hong, and L. Figueroa, "Predicting diode laser performance," *Proceedings of SPIE*, vol. 1418, pp. 123-131, 1991.

[Lut56] J. M. Luttinger, "Quantum theory of cyclotron resonance in semiconductor: general theory," *Phys. Rev.*, vol. 102, pp. 1030-1041, 1956.

[Mad87] O. Madelung, W. von der Osten, and U. Rössler, *Landolt-Börnstein: Numerical Data and Fundamental Relationship in Science and Technology*, vol. 17b, O. Madelung, Ed. Berlin: Springer-Verlag, 1987.

[Mad92] O. Madelung, W. von der Osten, and U. Rössler, *Landolt-Börnstein: Numerical Data and Fundamental Relationship in Science and Technology*, vol. 22a, O. Madelung, Ed. Berlin: Springer-Verlag, 1992.

[Nak96] S. Nakamura, M. Senoh, S Nagahama, N. Iwasa, T. Yamada, T. Matsushita, H. Kiyoku, and Y. Sugimoto, "InGaN-based multi-quantum-well-structure laser diodes," *Jpn. J. Appl. Phys.*, vol. 35, 1996.

[Nas73] F. R. Nash, "Mode guidance parallel to the junction plane of double-heterostructure GaAs lasers," *J. Appl. Phys.*, vol. 44, pp. 4696-4704, 1973.

[Off89] S. D. Offsey, W. J. Schaff, P. J. Tasker, H. Ennen, and L. F. Eastman, "Strained-layer InGaAs-GaAs-AlGaAs graded-index separate confinement heterostructure single quantum well lasers grown by molecular beam epitaxy," *Appl. Phys. Lett.*, vol. 54, pp. 2527-2529, 1989.

[Osi87] M. Osinski, and J. Buus, "Linewidth broadening factor in semiconductor lasers – an overview," *IEEE Quantum Electron.*, vol. QE-23, pp. 9-29, 1987.

[Ree95a] P. Rees, F. P. Logue, J. F. Donegan, J. F. Heffernan, C. Jordan, and J. Hegarty, "Calculation of gain-current characteristics in ZnCdSe-ZnSe quantum well structures including many body effects," *Appl. Phys. Lett.*, vol. 67, pp. 3780-3782, 1995.

[Ree95b] P. Rees, C. Cooper, P. Blood, P. M. Smowton, and J. Hegarty, "Gain characteristics of GaN quantum wells including many body effects," *Electron. Lett.*, vol. 31, pp. 149-159, 1995.

[Ree96] P. Rees, J. F. Heffernan, F. P. Logue, J. F. Donegan, C. Jordan, J. Hegarty, F. Hiei, and A. Ishibashi, "Optical gain in ZnCdSe-ZnSe quantum well structures," *Proceedings of SPIE*, vol. 2693, pp. 121-127, 1996.

[Shi89] C. Shieh, J. Mantz, H. Lee, D. Ackley, and R. Engelmann, "Anomalous dependence of threshold current on stripe width in gain-guided strained-layer InGaAs/GaAs quantum well lasers," *Appl. Phys. Lett.*, vol. 54, pp. 2521-2523, 1989.

[Tar84] S. Tarucha, H. Kobayashi, Y. Horikoshi, and H. Okamoto, "Carrier-induced energy-gap shrinkage in current-injection GaAs/AlGaAs MQW heterostructures," *Jpn. J. Appl. Phys.* vol. 23, pp. 874-878, 1984.

[Tie92] L. F. Tiemeijer, P. J. A. Thijs, J. J. M. Binsma, and T. V. Dongen, "Effect of free carriers on the linewidth enhancement factor of InGaAs/InP (strained-layer) multiple quantum well lasers," *Appl. Phys. Lett.*, vol. 60, pp. 2466-2468, 1992.

[Ver89] J. T. Verdeyen, *Laser Electronics*, Englewood Cliffs: Prentice-Hall, 1989.

[Wu94a] C. H. Wu, P. S. Zory, and M. A. Emanuel, "Contact reflectivity effects on thin p-clad InGaAs single quantum well lasers," *IEEE Photon. Technol. Lett.*, vol. 6, pp. 1427-1429, 1994.

[Wu94b] Y.-H Wu, "Structure-dependent threshold current density for CdZnSe-based II-VI semiconductor lasers," *IEEE. J. Quantum Electron.*, vol. QE-30, pp. 1562-1573, 1994.

[Yam87] M. Yamanishi, and Y. Lee, "Phase dampings of optical dipole moments and gain spectra in semiconductor lasers," *IEEE J. Quantum Electron.*, vol. QE-23, pp. 367-370, 1987.

[Zim88] R. Zimmermann, "Nonlinear optics and the Mott transition in semiconductor," *Phy. Stat. Sol. (b)*, vol. 146, pp. 371-384, 1988.

BIOGRAPHICAL SKETCH

Chia-Fu Hsu was born in Taipei, Taiwan, on May 23, 1970. He received his B.S. degree in electrophysics from the National Chiao-Tung University, Hsinchu, Taiwan, in 1992, and his M.S. degree in electrical engineering from the University of Florida, Gainesville, in 1993.

In January of 1994, he joined the Photonics Research Group at the University of Florida and he has been pursuing his Ph. D. degree in electrical and computer engineering under the direction of Dr. Peter Zory. He has worked on process and characterization of various semiconductor diode laser materials, development and characterization of liquid contact luminescence technique, theory of quantum cascade lasers and design of intersubband quantum box lasers. His research has focused on modeling of semiconductor quantum well lasers with many-body effects taken into account, especially the Coulomb attraction effects in the II-VI blue-green CdZnSe QW lasers.

In his spare time, he enjoys playing basketball and tennis, attending Gator football games and watching professional football.

I certify that I have read this study and that in my opinion it conforms to acceptable standards of scholarly presentation and is fully adequate, in scope and quality, as a dissertation for the degree of Doctor of Philosophy.

Peter S Zory

Peter S. Zory, Chairman
Professor of Electrical and Computer Engineering

I certify that I have read this study and that in my opinion it conforms to acceptable standards of scholarly presentation and is fully adequate, in scope and quality, as a dissertation for the degree of Doctor of Philosophy.

Gijs Bosman
Professor of Electrical and Computer Engineering

I certify that I have read this study and that in my opinion it conforms to acceptable standards of scholarly presentation and is fully adequate, in scope and quality, as a dissertation for the degree of Doctor of Philosophy.

FA Lindholm

Fredrik A. Lindholm
Professor of Electrical and Computer Engineering

I certify that I have read this study and that in my opinion it conforms to acceptable standards of scholarly presentation and is fully adequate, in scope and quality, as a dissertation for the degree of Doctor of Philosophy.

R. Srivastava

Ramakant Srivastava
Professor of Electrical and Computer Engineering

I certify that I have read this study and that in my opinion it conforms to acceptable standards of scholarly presentation and is fully adequate, in scope and quality, as a dissertation for the degree of Doctor of Philosophy.

Kevin S. Jones
Professor of Materials Science and Engineering

This dissertation was submitted to the Graduate Faculty of the College of Engineering and to the Graduate School and was accepted as partial fulfillment of the requirements for the degree of Doctor of Philosophy.

December 1997

Winfred M. Phillips
Dean, College of Engineering

Karen A. Holbrook
Dean, Graduate School

LD
1780
199_7
.H 8736

UNIVERSITY OF FLORIDA
3 1262 08556 6023